# Manufacturing of functionally graded ceramics with in-space resources

**Mathilde Anne Louise Laot**

Student number: 4849639
Faculty of Mechanical, Maritime and Materials Engineering (3mE)
Delft University of Technology

| | | |
|---|---|---|
| Supervisors: | Dr. V.A. Popovich | TU Delft |
| | Belinda Rich | ESTEC-ESA |
| | Ina Cheibas | ESTEC-ESA |
| Committee: | Dr. Ir. M.J.M Hermans | TU Delft |
| | Jia Fu | TU Delft |

18 December 2020

# Acknowledgment

Firstly, I would like to thank my supervisors Dr. Vera Popovich, Ina Cheibas and Belinda Rich who gave me the opportunity to work on this project and develop my knowledge about doing a research. This thesis has required a sense of innovation and discussions along the process with my supervisors have supported me a lot. Their help was valuable throughout the process to go through this project. This year has been complicated for everyone in the World but their support has been constant whenever some issues arose.

Furthermore, I would like to give a huge thank you to Jia Fu who gave a lot of his time to help me with my Spark Plasma Sintering. He has been very available to perform experiments with and even taught me how to use the device on my one while always keeping there for me. The experiments would not have been possible without him.
I would like to thank Jia-Ning Zhu for his help at the end of my master thesis. I am thankful for his support through Thermocalc® calculations.

I would also like to thank Jaap Hooijmans for the Digital Light Processing experiments. I would like to particularly thank Joost van Berge Henegouwen who has been very reactive and flexible to perform water-jet cutting of my samples.
I would also like to thank Richard Huizenga for the XRD experiments which weren't easy regarding the samples I had, Hans Brouwer for his help during the SPS experiments, Ton Rieslag and Elise Reinton for their support in the mechanical side of the thesis, Sander van Asperen and Luis de Almeida for their help with the samples preparation and the microscopy.

I would also like to thank my friends Mirthe, AiYu, Ya-Shan and Yuan who were there to discuss and have some breaks during these months of thesis (and months of coronavirus). It has always been enjoyable to take some breaks and forget about the stress of this period. I would also want to address a big "merci" to my French friends who have always been supportive even without seeing them: thank you to my friends 'centraliens' and especially to Léa, Ambre, Amelia and Maxime. I feel very privileged to have them on my side whatever the barriers are!

To finish, I can't forget my family who is my most important support. Studying in delft and doing this thesis wouldn't have been possible without their support. I am so grateful to have them to help me face the problems and always remains proud of what I can achieve. I would then finish my acknowledgments in French for them. « Merci beaucoup d'être là et de l'avoir toujours été pour moi ! Cette thèse est un accomplissement pour moi mais elle a été possible grâce à votre soutien inconditionnel. »

# Abstract

Building habitats on the Moon is required for long-duration missions foreseen in the very near future. The availability of lunar regolith will allow to manufacture such in space habitats and reduce the cost of space missions. However, the Moon has specific environmental characteristics that are different compared to terrestrial habitats: meteoroids impacts, high cosmic radiation level and high temperature gradient, etc.

Functionally graded materials (FGM) are high-performance composite materials, featuring such advantages as localized tailoring of material properties, improved interfacial boundary compatibility, and enhanced thermomechanical behaviour. Much of the current in-situ resource utilization (ISRU) manufacturing research explores additive manufacturing (AM) of as-received regolith, with some consideration given to metal alloys extracted in-situ. This study combines these two aspects by investigating the feasibility of in-situ manufactured metallic-regolith FGMs.

In this study three regolith simulant powders were first characterized based on their similarity with the actual lunar regolith and then assessed further for their AM processability. Digital Light Processing (DLP), Spark Plasma Sintering (SPS) and laser scanning, were selected due to their compatibility with metallic-ceramic processing in a space environment. The chosen AM techniques were first assessed on their capability to effectively consolidate regolith alone, before progressing to AM of regolith directly onto metallic substrates.

The powder characterisation proved that all three simulants have composition and particle size distribution close to the ones of the actual lunar regolith. Powders are composed of plagioclase, pyroxene and iron titanium oxide. Dense regolith samples were successfully shaped with DLP and subsequently consolidated with Spark Plasma Sintering at 1050 °C under 80 MPa with crushed lunar regolith simulant. Optimized processing conditions based on the sintering temperature, initial powder particle size and different compositions in the lunar regolith powders were identified. The reduction of the particle size proved to be the most significant factor to obtain a good densification.

Additive manufacturing was then studied as a potential technique to manufacture functionally graded materials combining the properties of the lunar regolith and metals (Ti6Al4V and 316L). The combination of lunar regolith and Ti6Al4V was found as the most promising. The hardness profile showed a gradual transition between the two layers and the interface was found to be strong and without any cracking or delamination. Furthermore, interesting segregation effects at the interface regions were observed and investigated in this work.

Additionally, results from this study indicate that laser-based additive manufacturing techniques could be a feasible method for application of FGM coatings, which presents a topic for further study focused on wear, corrosion and thermal resistant in-situ resource coatings.

While the current study showed that it is feasible to AM FGMs from lunar regolith, further developments of a fully optimized method have the potential to produce tailored, high-performance materials in an off-earth manufacturing setting, for the production of aerospace, robotic, or architectural components.

# Table of content

# List of figures

# List of tables

## Nomenclature

AM – Additive Manufacturing

CAD – Computer-aided Design

CSL – Ceramic Stereolithography

DLP – Digital Light Processing

DMD – Digital Micromirror Device

DSC – Differential Scanning Calorimetry

EDS – Energy Dispersive X-ray Spectroscopy

ESA – European Space Agency

FGM – Functionally Graded Materials

PLS – Pressureless Sintering

SEM – Scanning Electron Microscope

SLA - Stereolithography

SLM – Selective Laser Melting

SPS – Spark Plasma Sintering

TGA – Thermogravimetric Analysis

XRD – X-ray Diffraction

# 1 Introduction

In recent years the idea of human settlement on the Moon or on Mars has become very attractive. Researches are thus undergone to determine how humans can settle on these extra-terrestrial bodies regarding different issues such as harsh environment, financial issues and available materials to build space habitats. The Moon is viewed as the first step thanks to its proximity to Earth. Space habitats will be built on the Moon to allow humans to survive in the lunar environment and to protect them from threats like meteoroids or solar flares.

Finding a way to build lunar habitats is then key for human settlement. Bringing materials and equipment would be done at a very high cost and spatial agencies would thus prefer to use in-situ resources for space habitats. Indeed, according to NASA, “In-situ resource utilization will enable the affordable establishment of extraterrestrial exploration and operations by minimizing the materials carried from Earth” [1]. Lunar regolith is seen as a promising in-situ resources since it can provide a good protection from cosmic radiation and meteoroids impacts, and it is widely available on the Moon. The composition and the microstructure of the lunar regolith have been determined thanks to the samples brought back to Earth. The lunar regolith has specificities such as particles shape or presence of different phases that have to be taken into account while manufacturing habitats. Several techniques are under research to determine whether they are feasible for space applications. Lunar regolith can be consolidated through many techniques: special types of concrete using small amount of water, Spark Plasma Sintering, Additive Manufacturing techniques or others discussed in current review.

Additive manufacturing, also well known as 3D-printing, offers many advantages for space application. Additive manufacturing is versatile, produces low amount of waste, can be fast and used to produce complex shapes. However, additive manufacturing refers to many different techniques and a discussion over their advantages and disadvantages is necessary to assess whether they are promising for space habitat manufacturing. Many techniques like solar sintering, selective laser melting or stereolithography have been tested with lunar regolith. Additive manufacturing is also promising since it can be used to build components made out of dissimilar materials like metals combined with ceramics. Functionally graded materials (FGM) are a newly type of materials that are used to obtain materials with the best combination of properties. FGM are an alternative for space habitats: the inner and outer properties are different and combining the lunar regolith with metal would give good properties for both sides.

This literature review is divided into 6 main chapters.

- Chapter 2 is dedicated to the description of lunar regolith and the simulants currently available on the market for the purpose of scientific research.
- Chapter 3 outlines specific requirements for lunar habitat.
- Chapter 4 provides an overview of different consolidation techniques that showed promising results.
- Chapter 5 introduces the concept of functionally graded materials and its application for lunar habitats.
- Chapter 6 and 7 are dedicated to the main literature review conclusions and research objectives set for this master study.

# 2 Literature review

## 2.1 Lunar regolith

### 2.1.1 Definition of lunar regolith

The Moon surface is covered by a thick layer of regolith (Figure 1). Its composition and structure differ on location. The regolith is 4 – 5 m thick in the mare regions and 10 – 15m thick in the Highlands regions. Lunar soil and lunar dust are terms used to describe specific fraction of the lunar regolith. Another characteristic of the lunar regolith is indeed its wide particle size distribution. Lunar soil is the subcentimeter (< 1cm) fraction of the lunar regolith [2] while lunar dust describes the < 50 μm or < 20 μm fraction of the regolith [3].

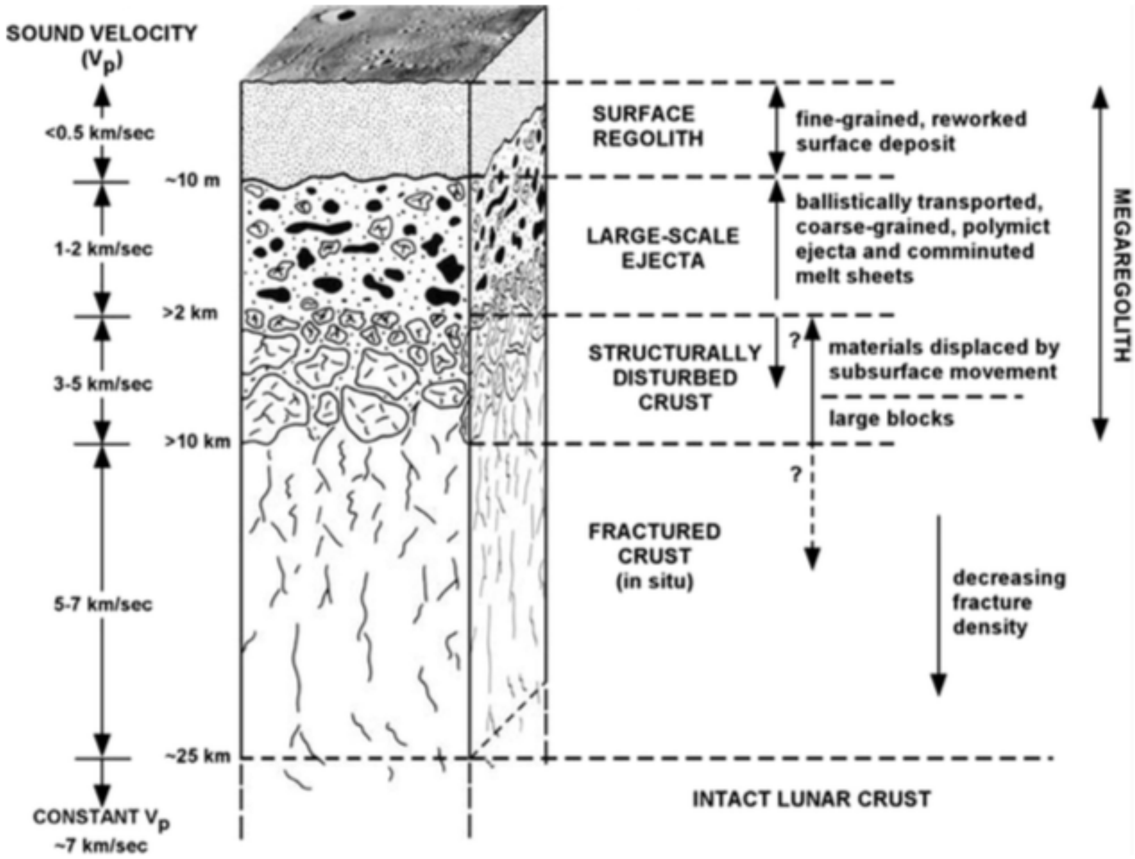

*Figure 1. Idealized profile of the lunar megaregolith [4]*

The formation of this lunar top-layer results from a combination of physical and chemical processes due to constant bombardment by meteorites as well as solar wind and galactic/cosmic ray particles. The rocks are bombarded by micrometeorites at very high velocity due to the absence of an atmosphere and the rocks are thus crushed into small particles. Furthermore, these micrometeorites can melt some fraction of the particles and the melt penetrates into the soil to form aggregates called *agglutinates*. A portion of the melt can also be vaporized thanks to the energy provided by the impacts and it is deposited on the surface particles as silica-rich glass coatings containing abundant nanophase metallic iron [3]. The composition of the lunar regolith reflects the history of its formation.

The characteristics of the lunar regolith have been examined thanks to the samples brought back to Earth with the Moon exploration missions such as Apollo missions. The samples are from different regions of the Moon surface and represents a range of compositions available on the Moon. Many researches have been done to compare compositions of lunar regolith. Five basic particle types composed the lunar soil: mineral fragments, pristine crystalline rock fragments, breccia fragments, glasses of various kinds, and the unique lunar constructional particles called agglutinates [5].

Lunar regolith has a quite simple mineralogical composition as shown in Table 1. Lunar dust consists of impact glass (mostly agglutinitic glass), plagioclase and pyroxene: these phases make up to 70 – 98% of the lunar dust. Agglutinitic glasses show a wide range of chemical compositions from virtually pure plagioclase to mixture of olivine and pyroxene [3].

*Table 1. Minerals forming lunar rocks according to NASA [2]*

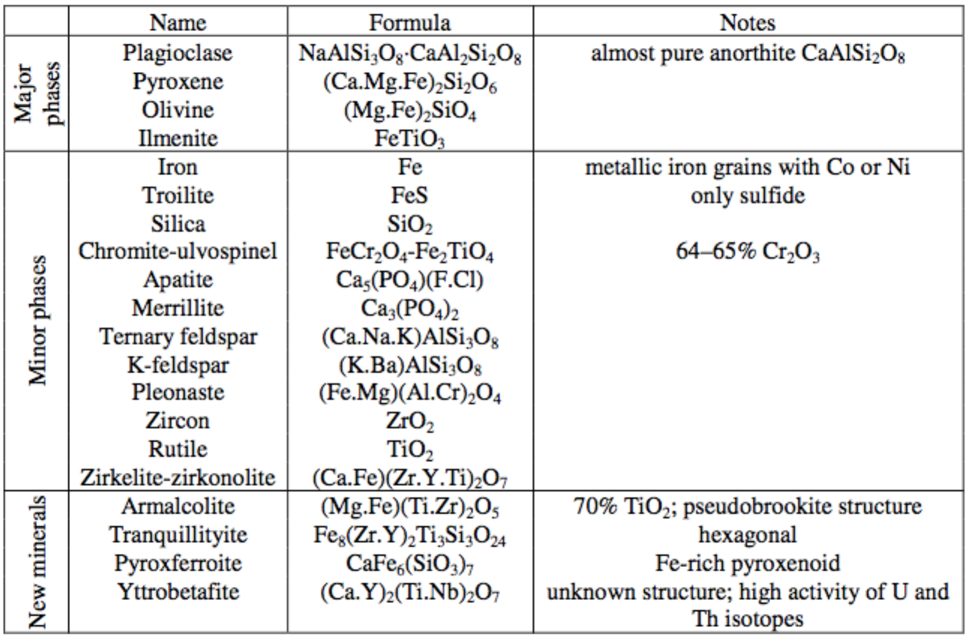

| | Name | Formula | Notes |
|---|---|---|---|
| Major phases | Plagioclase | $NaAlSi_3O_8 \cdot CaAl_2Si_2O_8$ | almost pure anorthite $CaAlSi_2O_8$ |
| | Pyroxene | $(Ca.Mg.Fe)_2Si_2O_6$ | |
| | Olivine | $(Mg.Fe)_2SiO_4$ | |
| | Ilmenite | $FeTiO_3$ | |
| Minor phases | Iron | $Fe$ | metallic iron grains with Co or Ni |
| | Troilite | $FeS$ | only sulfide |
| | Silica | $SiO_2$ | |
| | Chromite-ulvospinel | $FeCr_2O_4$-$Fe_2TiO_4$ | 64–65% $Cr_2O_3$ |
| | Apatite | $Ca_5(PO_4)(F.Cl)$ | |
| | Merrillite | $Ca_3(PO_4)_2$ | |
| | Ternary feldspar | $(Ca.Na.K)AlSi_3O_8$ | |
| | K-feldspar | $(K.Ba)AlSi_3O_8$ | |
| | Pleonaste | $(Fe.Mg)(Al.Cr)_2O_4$ | |
| | Zircon | $ZrO_2$ | |
| | Rutile | $TiO_2$ | |
| | Zirkelite-zirkonolite | $(Ca.Fe)(Zr.Y.Ti)_2O_7$ | |
| New minerals | Armalcolite | $(Mg.Fe)(Ti.Zr)_2O_5$ | 70% $TiO_2$; pseudobrookite structure |
| | Tranquillityite | $Fe_8(Zr.Y)_2Ti_3Si_3O_{24}$ | hexagonal |
| | Pyroxferroite | $CaFe_6(SiO_3)_7$ | Fe-rich pyroxenoid |
| | Yttrobetafite | $(Ca.Y)_2(Ti.Nb)_2O_7$ | unknown structure; high activity of U and Th isotopes |

### 2.1.2 Simulants available on the market

A simulant is a granular or powder material that mimics one or more properties of the material found on the Moon [6]. Many simulants exist on the market. Their chemical and physical properties must match as much as possible the ones of the lunar regolith to be able to draw accurate conclusions from the experiments. In term of chemical composition, the simulant should reflect the mineral composition of lunar regolith and have similar compounds, at least the mineral compounds that will play the major role in the process studied. Moreover, in term of physical properties, the granulometry of the simulant is of particular importance to mimic the behaviour of the lunar regolith.

The development of lunar simulants has known different main stages. After Apollo missions, lunar simulants were developed by individual research groups for their own research. In 1991, a workshop was held to regulate the manufacturing of simulants and the simulant JSC-1 (from Johnson Space Center) was produced and sold widely. Thereafter, in 2005, a new workshop was held, and it was decided that a new batch of simulants was needed. New simulants will have specific properties useful for different applications [3]. The main common simulants found in literature will be discussed below in Table 2. It must be noted that all simulants are different and so, extending results from a research must be done carefully if another simulant is used (especially if the simulants differ significantly on the factors influencing the results) [7].

*Table 2. Bulk chemistry of common lunar soil simulants: JSC-1 [8] , JSC-1A/JSC-2A [9] , DNA-1 [10], DNA-1A [10], CLRS-2 [11] , CAS-1 [12], FJS-1 [13](*indicates that content of FeO and Fe2O3 are not distinguished)*

| | JSC-1 (wt. %) | JSC-1A /JSC-2A (wt. %) | DNA-1 (wt. %) | DNA-1A (wt. %) | CLRS-2 (wt. %) | CAS-1 (wt. %) | FJS-1 (wt. %) |
|---|---|---|---|---|---|---|---|
| **$SiO_2$** | 47.71 | 46.67 | 41.90 | 51.97 | 41.89 | 49.24 | 45-55 |
| **$TiO_2$** | 1.59 | 1.71 | 1.31 | 0.85 | 7.62 | 1.91 | 1-2 |
| **$Al_2O_3$** | 15.02 | 15.79 | 16.02 | 18.02 | 13.41 | 15.80 | 12-18 |
| **$Fe_2O_3$** | 3.44 | 3.41 | 14.60 | 7.07 | 15.90* | 11.47* | 2-4 |
| **FeO** | 7.35 | 7.57 | - | - | | | 4-8 |
| **MgO** | 9.01 | 9.39 | 6.34 | 2.70 | 7.06 | 8.72 | 3-7 |
| **CaO** | 10.42 | 9.90 | 12.90 | 7.40 | 9.70 | 7.25 | 7-10 |
| **$Na_2O$** | 2.70 | 2.83 | 2.66 | 4.81 | 2.34 | 3.08 | 2-3 |
| **$K_2O$** | 0.82 | 0.78 | 2.53 | 4.63 | 0.78 | 1.03 | 0.5-0.7 |
| **MnO** | 0.18 | 0.19 | 0.21 | 0.14 | 0.20 | 0.14 | - |
| **$Cr_2O_3$** | 0.04 | - | - | - | - | - | - |
| **$P_2O_5$** | 0.66 | 0.66 | 0.34 | 0.41 | 0.25 | 0.3 | - |
| **$SO_3$** | - | - | - | - | 0.71 | - | - |
| **LOI** | 0.71 | - | - | 2.00 | - | 0.52 | - |

## 2.2 Specific requirements for lunar habitats

### 2.2.1 Lunar environment

The lunar environment has its specificities that must be carefully considered and understood to determine the required properties that a structure must meet. The lunar environment is very different from the earth environment. Table 3 shows the difference between these two environments.

The most important factors that will have different impacts on the moon compared to earth are: temperature, radiation, atmosphere and pressure, meteoroids, gravity, the length of the lunar day, dust and seismicity [14].

*Table 3. Comparison between Earth and Moon on physical parameters [15]*

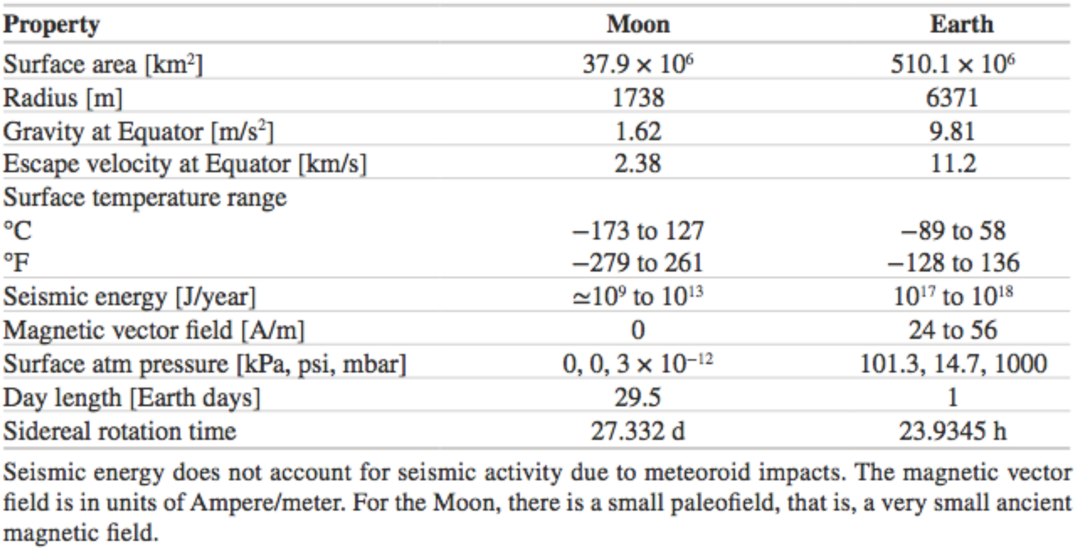

| Property | Moon | Earth |
|---|---|---|
| Surface area [km$^2$] | $37.9 \times 10^6$ | $510.1 \times 10^6$ |
| Radius [m] | 1738 | 6371 |
| Gravity at Equator [m/s$^2$] | 1.62 | 9.81 |
| Escape velocity at Equator [km/s] | 2.38 | 11.2 |
| Surface temperature range | | |
| °C | −173 to 127 | −89 to 58 |
| °F | −279 to 261 | −128 to 136 |
| Seismic energy [J/year] | $\simeq 10^9$ to $10^{13}$ | $10^{17}$ to $10^{18}$ |
| Magnetic vector field [A/m] | 0 | 24 to 56 |
| Surface atm pressure [kPa, psi, mbar] | 0, 0, $3 \times 10^{-12}$ | 101.3, 14.7, 1000 |
| Day length [Earth days] | 29.5 | 1 |
| Sidereal rotation time | 27.332 d | 23.9345 h |

Seismic energy does not account for seismic activity due to meteoroid impacts. The magnetic vector field is in units of Ampere/meter. For the Moon, there is a small paleofield, that is, a very small ancient magnetic field.

The temperature on the Moon varies significantly during the lunar day: the gradient of temperature is higher than 200 K. It is indeed due to the length of the lunar day: The Moon has more time to heat up and to cool down during the long lunar day. Moreover, the average temperature at the equator is only – 18 °C and the temperature can be even lower at other locations. The materials must have good thermal properties at low temperatures but also, a good thermal fatigue behaviour to sustain the temperature fluctuation. The coefficient of thermal expansion of different phases or dissimilar materials must match to avoid early cracking in the whole structure.

The quasi absence of atmosphere and low pressure impede good thermal insulation, radiation shielding and does not stop meteoroids. Moreover, the lunar habitats have to be thought as a pressure vessel to let humans live in. Inflatables can be used for this purpose.

Meteoroids impact the lunar surface with high velocity (from 10 to 72 km/s) and a lunar structure have to remain viable under these threats. Calculus were made by different authors and they found that a regolith cover that offers a good thermal and radiation protection will be sufficient to protect from meteoroids impacts.

The gravity on the Moon is one sixth the gravity on earth. The weight-bearing capacity of a structure will thus be six times higher on the Moon than on the Earth. Furthermore, the low gravity is important when considering structure anchoring.

The dust can levitate up to some meters above the surface due to a photoelectric change in the conductivity of the regolith particles during the day. The particles are angular and thus are abrasive.

The seismic activity on the Moon is really low compared to Earth and has a low impact on structural design. Furthermore, the moonquakes are often due to meteoroids impacts and so meteoroids are more important in structural design.

Other concerns with the lunar environment are the biological issues. Indeed, toxicity of the regolith or radiation are factors that might prevent humans from living on the Moon. Thus, the structure must be an efficient barrier against these external factors. The dose equivalent due to galactic cosmic radiation is about 0.3 Sv/year whereas the dose equivalent due to cosmic rays is 2 – 4 mSv/year on Earth: the structures have to be able to reduce the dose equivalent to an acceptable level close to the dose equivalent on Earth. Recommendations of maximum dose acceptable have been set up but they depend on the length of the stay among other things. For instance, the Space Studies Board in 1996 recommended a maximum dose equivalent of 0.5 Sv/year but it can be only be acceptable if humans stay for 2 to 8 years and not more. In the case of workers in nuclear power plants, the limit is set up to 0.05 Sv/year since it is considered that they will be exposed to radiation for many years. A regolith cover of 2 to 5 m would be able to reduce the radiation exposure to an acceptable dose.

### 2.2.2 Materials properties required

In this section, we only consider the properties that the outer structure of the lunar habitat must have. Indeed, the project led by ESA considers a lunar habitat made of an inflatable structure and an outer shell of sintered regolith (or of a functionally graded material). The inflatable inner structure will act as a pressure containment.

The particular environment leads to a list of properties that a material has to fulfil to be consider as a promising one for lunar applications. The properties are given in the following table.

*Table 4. Requirement for lunar space habitats*

| | |
|---|---|
| Thermal cyclic fatigue | High gradient of temperature (- 173 °C to 127 °C) due to long lunar day |
| Impact toughness | Meteoroids impact with high velocities and can form craters up to 500 μm [16] |
| Cosmic radiation resistance | Reducing the dose equivalent from 0.3 Sv/year to 0.003 Sv/year and to withstand individual events with a dose of 1000 Sv. |
| Wear resistance | Abrasiveness of regolith (small angular particles) that can be suspended 1 – 2 m above the surface |
| Compressive strength | Considering a gravitational acceleration of 1/6 g ($g=9.8$ m/s$^2$ on earth) |
| Solar radiation resistance | On the moon, solar radiation is 1316 to 1421 W/m$^2$<br>On Earth, it is 0.095 W/m$^2$ |

Many mechanical and thermal properties are required for a suitable lunar space habitat. Structures made out of in-situ resources might not meet these requirements. Thus, it will be beneficial to manufacture a functionally graded materials with lunar regolith and metal to have a good combination of both properties.

## 2.3 Consolidation Techniques

### 2.3.1 Conventional techniques

#### *2.3.1.1 Spark Plasma Sintering (SPS)*

##### Principles

Spark Plasma Sintering is a sintering process that uses a combination of electric pulse and external pressure to compact the powder. This process is suitable for high-temperature materials with poor deformability. A pulsed direct current passes through the sample and produces an electric field. The powder is thus heated from inside and outside. The sintering temperature range used for SPS can be a few hundred degrees lower than the sintering temperature used for other conventional techniques like Hot Pressing. During the process, spark discharge can occur in the air gap between the particles leading to the formation of a high-temperature zone. The surface of particles melts and impurities can evaporate due to this increase of temperature to about 1000 °C. The melted particle's surfaces can coalesce and form neck between particles [17].

The main 4 stages of SPS are shown on Figure 2.

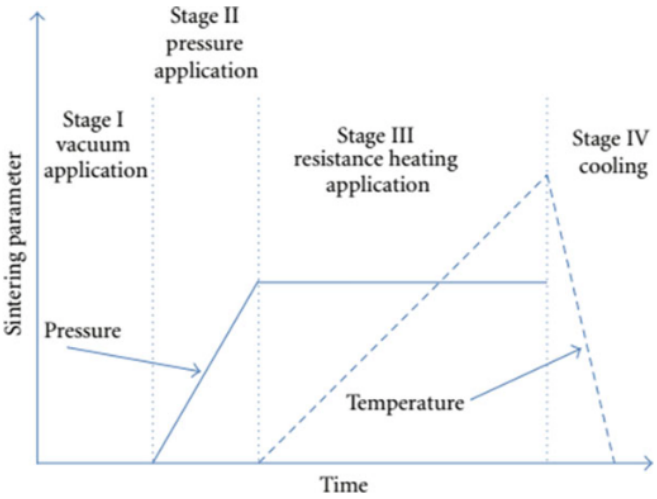

*Figure 2. SPS stages [17]*

High density can be achieved with SPS thanks to the melting of the particle's surface. It is also achieved by applying external pressure that enhances the previous densification mechanism and also promotes other densification mechanisms such as plastic deformation. The lower temperature used in SPS helps to control the grain growth during the process [17]. Table 5 summarises the advantages and disadvantages of this technique.

*Table 5. Advantages and disadvantages of SPS*

| Advantages | Disadvantages |
|---|---|
| • Microstructure control due to low temperature and short time<br>• High density due to higher heating rate and pressure than other techniques<br>• Dissimilar materials can be sintered<br>• Fast and FGMs can be produced<br>• Cost of SPS is 50 – 80% lower than other conventional sintering techniques<br>• Temperature of 900°C enough for sintering lunar regolith<br>• Good mechanical properties | • Only simple symmetrical shape can be prepared<br>• Expensive DC generator required<br>• For very small powder (less than 100 nm), significant temperature gradient can lead to non-uniform densification<br>• Sieving or crushing needed for lunar soil regolith<br>• Limited to simple shapes |

### Applications – Ceramics/Lunar soil simulant

SPS has been used to sinter lunar soil simulants. Zhang and al. [13] studied the feasibility of this technique to sinter properly the lunar soil and to achieve good densification of the lunar soil. They studied the effect of SPS parameters such as temperature, pressure and time on the mechanical properties of the sintered parts and on the microstructural evolution. They used the simulant FJS-1, whose composition is given in Table 2. This simulant has a density of 1.85 g/cm$^3$ and a particle size distribution ranging from 5 to 5000 μm comparable to the particle size distribution of the lunar regolith. Their samples were sintered in a 20 mm diameter graphite die at different temperatures and at a uniaxial pressure of 50 or 100 MPa under vacuum (2 x 10$^{-2}$ Torr). The profiles of temperature for the different samples are given in
Figure 3. After being cooled to 500 °C, the samples are let cool down naturally to room temperature.

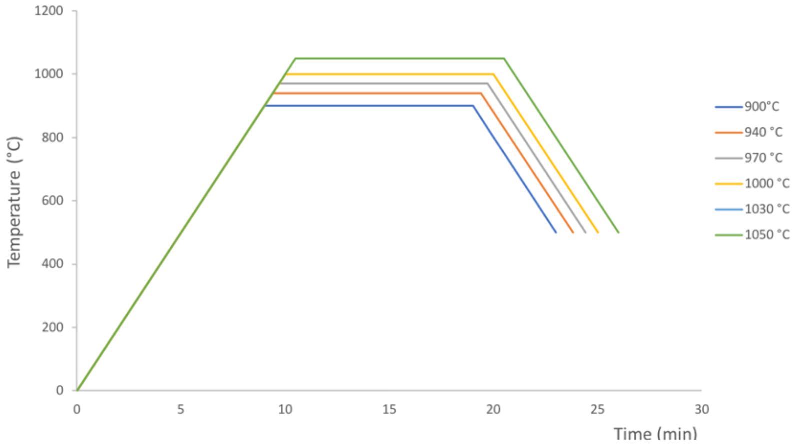

*Figure 3. Temperature profiles of the samples during SPS experiments*

SPSed samples showed higher densities than Pressureless Sintered (PLS) samples. Increase in densities was observed for temperatures as low as 900 °C and the maximum densities was 2.90 g/cm$^3$ for the samples sintered at 1050 °C and under 100 MPa pressure (figure 4). Moreover, increasing the dwelling time to 20, 30 or 40 minutes at 1050 °C improved only slightly the density. This slightly change in density might be due to microstructural evolution. The increase of density with temperature was not viable above 1050 °C because liquid formed and squeezed out of the mold.

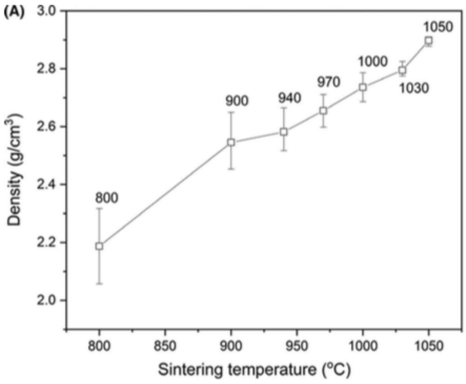

*Figure 4. Density of SPSed FJS-1 samples as a function of sintering temperature [13]*

SPSed samples have a more homogeneous and dense structure while sintering temperature is increased as shown on Figure 5. Moreover, the SPS process was proved to be more efficient than PLS in densification of the lunar simulant. SPSed samples have denser and more homogeneous microstructures than PLSed samples.

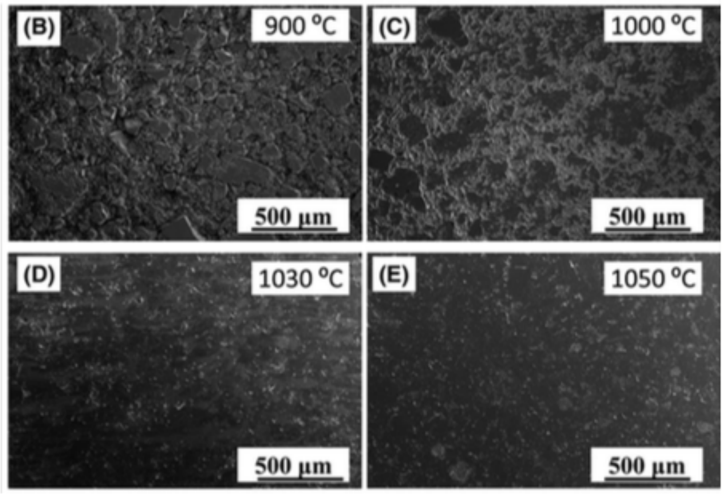

*Figure 5. Secondary electron images of the polished (B) SPS900-100, (C) SPS1000-100, (D) SPS1030-100, (E) SPS1050-100 samples [13]*

XRD measurements have been performed to determine the evolution of microstructure during sintering. The main phase in SPSed samples is sodian anorthite (Figure 6). During SPS, augite particles are crushed by the applied pressure and the partially dissolved sodian anorthite and glass mixture is pushed into the gaps formed between the crushed augite. This repartition of liquid between phases accelerates the densification process.

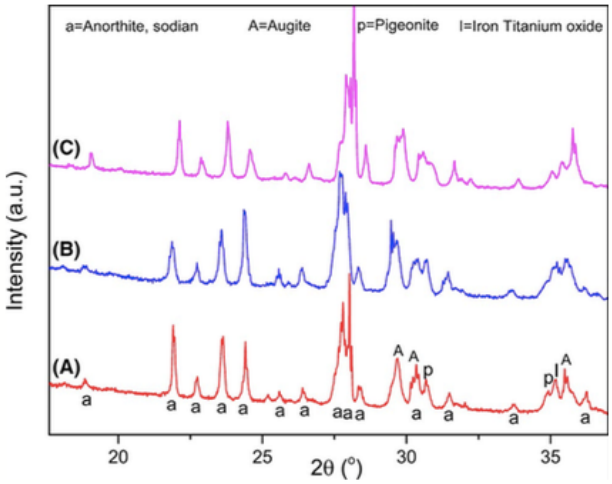

*Figure 6. XRD from the surface of (A) SPS900-100, (B) SPS1000-100, and (C) SPS1050-100, showing limited phase transformation from sodian anorthite to augite [13]*

Furthermore, microhardness tests have been done. It was shown that the standard deviation for SPSed samples is lower than PLSed samples proving that the microstructure is more homogeneous in the SPSed samples. They concluded that applied pressure and pulse electric current help to accelerate the densification of the powder. Finally, they also performed nanoindentation tests to determine mechanical properties at the phase level compared to the properties of the FJS-1 powder. They observed that SPSed samples have larger region of high elastic modulus and nanohardness than the raw powder.

Phuah and al. [18] have just published a paper last August about spark plasma sintering with lunar regolith simulant. They used the simulant JSC-1A (Table 2) and ball-milled the powder: the average particle size was reduced to 1,67 µm from 23,9 µm. These authors used low pressure and temperature compared to Zhang and al. [13]. They sintered their samples at 550 °C under 30 MPa and at 700 °C under 50 MPa and were both heated at 100 °C/min.

The increase of temperature and pressure increases the crystallinity. XRD patterns revealed the presence of an amorphous phase for the samples 550 °C/30 MPa while this amorphous phase is not detected for the other sample 700 °C/50 MPa. The overall composition is however similar to the one of the as-received powder with mainly plagioclase, pyroxene, olivine and ilmenite.

The sample at higher temperature and higher pressure was more densified and had smaller pores compared to the samples 550 °C/30 MPa as shown Figure 7. The higher pressure and temperature increase the driving force for densification and close the porosities. They achieved a relative density of 97 % at 700 °C and 50 MPa. The hardness was measured and was comparable to the hardness of glass materials. Moreover, they studied the ferroelectric and magnetic behavior of the samples since the lunar simulant are composed of iron and dielectric oxides. Higher temperature and pressure lead to stronger ferromagnetic and ferroelectric properties: higher saturation and larger coercivity, and higher saturated polarization.

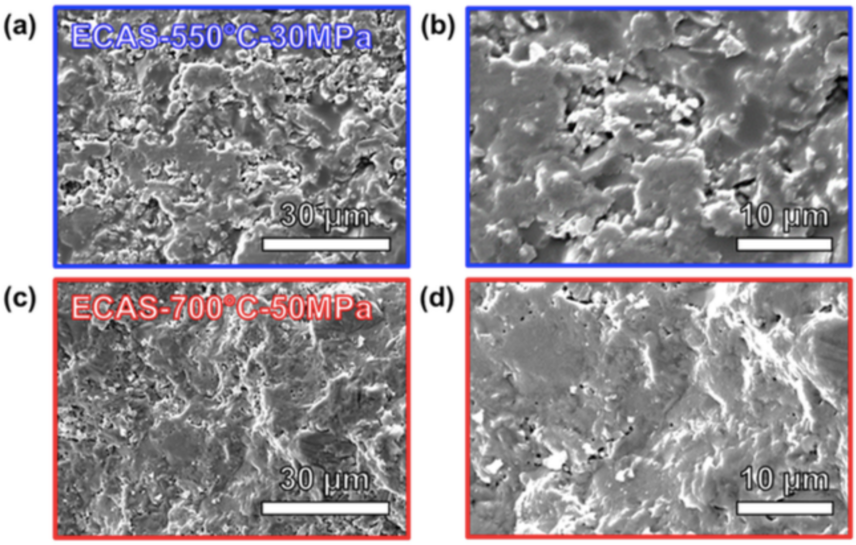

*Figure 7. Fracture surface of (a,b) ECAS-550 °C-30 MPa and (c,d) ECAS-700 °C-50 MPa* [18]

SPS is a promising process to sinter lunar simulant since it allows the manufacturing of parts with mechanical properties better than with PLS technique. Depending on the sintering temperature, the dominant densification mechanism differs. At 900 – 1000 °C, densification occurs via plastic deformation of phases with low modulus and melting point that can fill the gaps between powder particles. At temperature higher than 1000 °C, the dominant densification process is a diffusion-controlled process involving movement of interfaces and grain boundaries [13].

Other specific techniques have been studied such as vacuum sintering or thermite reactions methods because they take into account some specificities of the lunar environment (low gravity, lack of energy source, etc).

#### *2.3.1.2 Vacuum sintering*

Researches on vacuum sintering have been pursued to study the effect of vacuum because the gravity is very low on the Moon. Song and al. [19] studied the sintering process of the lunar simulant CLRS-1

(Table 2), the physiochemical properties and the pore-forming mechanism. They sintered at different temperatures from 700 to 1150 °C.
They observed the formation of macro-pores of irregular shape at temperature up to 1100 °C and also that smaller pores are generated during sintering. On the contrary, samples sintered at temperature lower than 1050 °C had dense structures. The dense character of the samples is related to a balance between the evaporation rate of substances and the mass transfer rate. A faster evaporation rate of substance compared to the mass transfer rate impedes the closure of pores and the structures is less dense. The density is the lowest when sintered at 1100 °C since the porosity is the highest: at higher temperature, the content of liquid phase increases and so the mass transfer rate increases, and pores shrink.

The porous materials have low thermal conductivity at room temperature and at lunar surface temperature (123 °C) as showed on table 6. The thermal conductivity increases dramatically for porous media at 600 °C due to thermal radiation in pores.

*Table 6. Thermal conductivity and specific heat of air sintered samples and vacuum sintered samples at 25 °C, 123 °C and 600 °C [19]*

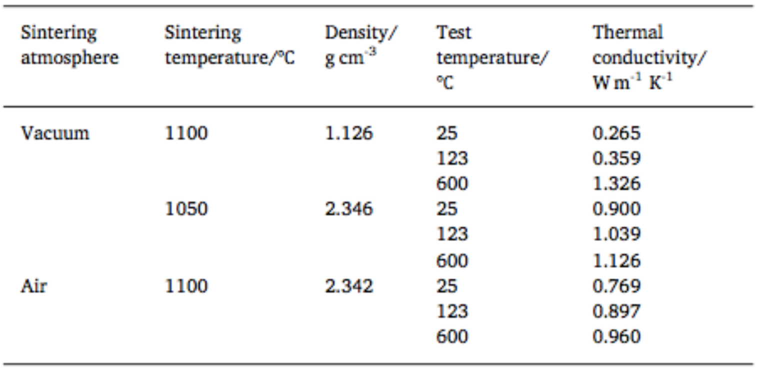

| Sintering atmosphere | Sintering temperature/°C | Density/ g cm$^{-3}$ | Test temperature/ °C | Thermal conductivity/ W m$^{-1}$ K$^{-1}$ |
|---|---|---|---|---|
| Vacuum | 1100 | 1.126 | 25 | 0.265 |
| | | | 123 | 0.359 |
| | | | 600 | 1.326 |
| | 1050 | 2.346 | 25 | 0.900 |
| | | | 123 | 1.039 |
| | | | 600 | 1.126 |
| Air | 1100 | 2.342 | 25 | 0.769 |
| | | | 123 | 0.897 |
| | | | 600 | 0.960 |

This study proved that vacuum-sintered materials could be used in space habitats as thermal insulation layers. Nevertheless, sintering experiments were carried at a vacuum degree of about $10^{-3}$ mbar which is low compared to $10^{-12}$ mbar on the Moon. Thus, the effects of vacuum might be better on the moon like the thermal properties. The advantages and disadvantages of vacuum sintering are summarised in table 7.

*Table 7. Advantages and disadvantages of vacuum sintering*

| Advantages | Disadvantages |
|---|---|
| • Sintered parts with low thermal conductivity<br>• Prevention of oxidization | • High weight loss increasing with temperature<br>• Presence of macro-pores, which can be controlled with sintering temperature<br>• Shrinkage dependent on the sintering temperature |

### 2.3.1.3 Thermite reactions methods

Sintering techniques need energy to be used and the energy efficiency is critical on the Moon. Other techniques are thus under research to overcome the energy issue. Nevertheless, techniques like aluminum-regolith bricks used only a maximum of 60 wt.% of regolith which involves the input of

materials from Earth. Hobosyan and Martirosyan [20] studied the sintering of lunar regolith via thermite reactions and used the simulant JSC-1A. They mixed the regolith powder with aluminum and Polytetrafluoroethylene: use of Al alone did not provide sufficient energy to the system. The samples were heated via a combustion flame that propagates throughout all the mixture placed in a die.
The samples had a hard and porous structure mainly due to escaping of gaseous phases. A minimal amount of 1.5 wt.% of Teflon (for 12 wt.% Al) was necessary to make to combustion wave propagate spontaneously. The use of Teflon activates Al by removing the oxide layers on the particles. Higher content of Teflon gives rise to higher porosity as showed on figure 8.

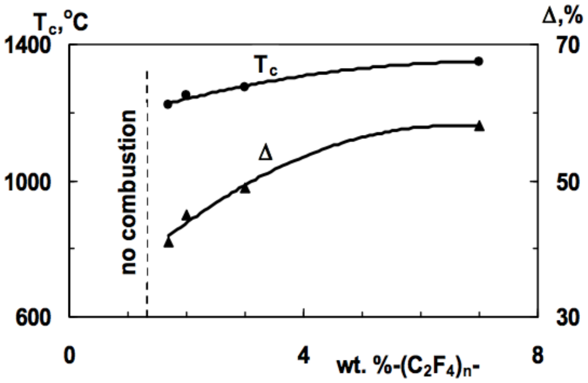

*Figure 8. Combustion temperature and product porosity as a function of Teflon concentration in the mixture [20]*

This technique provides a promising alternative to other sintering process which demands high amount of energy. However, the lunar regolith has to be mixed with other substances to overcome heating issues even if the amount of added materials was lowered.

Faierson and al. [21] studied the feasibility of manufacturing a voussoir structure via geothermite reactions. A geothermite reaction is a reaction between minerals and a reducing agent, which exhibits a thermite-type of reaction behavior. They mixed 67 wt.% of JSC-1A regolith with 33 wt.% aluminum and used several batches of simulant with different average particle sizes (JSC-1A with an average particle size of 185 μm and JSC-1AF with an average particle size of 25 μm). The mixtures were poured into a silica crucible and the reactions were initiated with electric current through NiCr wires. Figure 9 shows how the heating is conducted.

Reactions were quicker to initiate when using the JSC-1AF. Some residual unreacted mixtures were found at the edges of the crucible with the simulant JSC-1A. Smaller particle sizes have higher surface area where reactions can occur and propagate. Moreover, larger quantities of outgassing were observed with JSC-1AF and thus, surface cracking and deformation were more important [21].

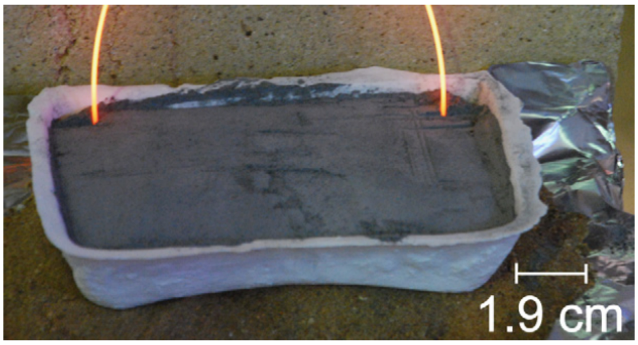

*Figure 9. Heating procedure of mixture of regolith and aluminum [21]*

Geothermite reactions are promising to build bricks but mechanical properties must be studied to determine whether the manufactured bricks are suitable for lunar space habitats. Their advantages and disadvantages are summarised in table 8.

*Table 8. Advantages and disadvantages of thermite reactions techniques*

| Advantages | Disadvantages |
|---|---|
| • Reduction of energy needed<br>• Limited equipment is required<br>• Quick reactions with smaller particles | • Addition of Al or other substances like Teflon<br>• Porous structures<br>• Little information about mechanical properties<br>• Sieving or crushing required for lunar regolith<br>• Deformation and surface cracking (even more with smaller particles) |

## 2.3.2 Additive manufacturing (AM) processes

### *2.3.2.1 Introduction to additive manufacturing*

Additive manufacturing (AM), also well-known as 3D-printing, is defined in ISO/ASTM 52900 as 'process of joining materials to make parts from 3D model data, usually layer upon layer, as opposed to subtractive manufacturing and formative manufacturing methodologies' [22].

The additive manufacturing technologies encompasses a wide range of different processes as shown on figure 10. The ISO/ASTM defines seven classes of AM processes. These seven classes are [23]:

- *Binder Jetting*: a process in which a liquid bonding agent is selectively deposited to join powder materials.
- *Directed Energy Deposition*: a process in which focused thermal energy is used to fuse materials by melting as they are being deposited.
- *Material Extrusion*: a process in which material is selectively dispensed through a nozzle or orifice.
- *Material Jetting*: a process in which droplets of build material are selectively deposited.
- *Powder Bed Fusion*: a process in which thermal energy selectively fuses regions of a powder bed.
- *Sheet Lamination*: a process in which sheets of material are bonded to form a part.
- *VAT Photopolymerization*: a process in which liquid photopolymer in a vat is selectively cured by light-activated polymerization.

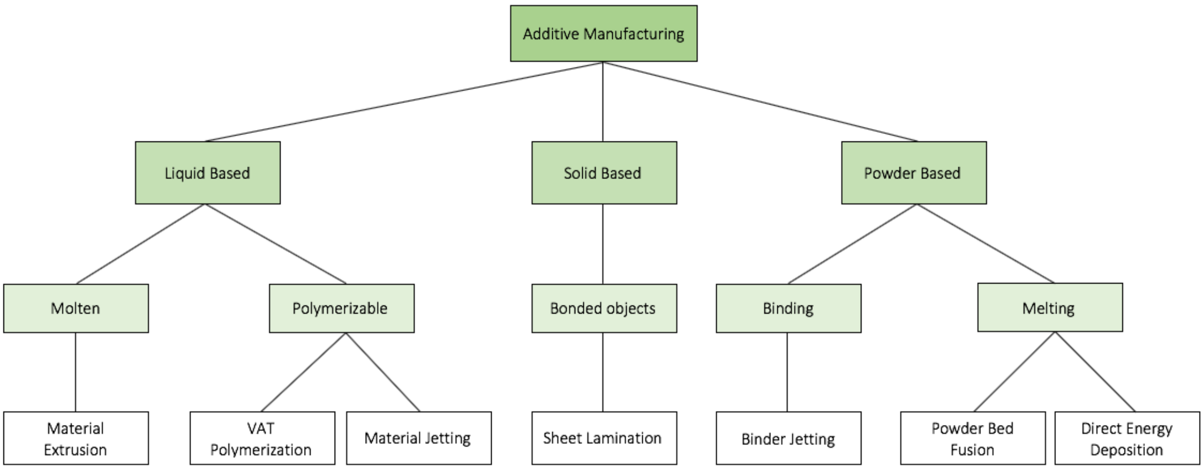

*Figure 10. Classification of Additive Manufacturing processes (adapted from [24])*

Additive manufacturing technique is very attractive for its cost-effectiveness. It lets produce complex-shaped parts as a single unit object by printing it layer by layer conversely to conventional techniques. AM reduces the production time and can be used to produce customized parts at a mass production rate at lower costs [25].

Several processes of additive manufacturing will be discussed below. The different techniques have been selected regarding our objective which is to 3D-print lunar soil and even to manufacture a functionally graded material composed of lunar soil and a metal.

### *2.3.2.2 Stereolithography*

#### Principles

Stereolithography (SLA) is an additive manufacturing technique historically used to print polymers. It is defined in ASTM standard as ‘a vat photopolymerization process used to produce parts from photopolymer materials in a liquid state using one or more lasers to selectively cure to a predetermined thickness and harden the material into shape layer upon layer’ [26]. The conventional stereolithography uses an ultraviolet laser beam to solidify and cure the polymer. The laser beam path is controlled by a computer using a sliced computer-aided design (CAD) model.

The resin consists of photoinitiators, polymerizable oligomers or prepolymers, a reactive diluent and additives. Under light exposure, prepolymers react through a chain reaction initiated by reactive species to transform into a crosslinked polymer.
The monomers in the resin usually do not initiate reactive species under irradiation and so, initiators are needed. These initiators will start the polymerization through a light-polymer interaction. The first step of the process is a photophysical stage involving no chemical reactions but only motions of electrons. Functional groups of the initiators will absorb incident photons promoting transition to an excited state. Two specific conditions must be met to make absorption take place:

- The energy of the photon must be at least equal to the energy difference between the ground state and the excited state:

  $$\Delta E = E_{excited} - E_0 = h\nu \tag{1}$$

  with h, Planck constant; ν, frequency of the photon; and, $E_{excited}$ ($E_0$) the energy of the excited state (ground state)
- The dipole moment of the molecule must change during the transition due to a specific interaction between the electric component of the incident photon and the molecule.

Then, a curing reaction will take place. This reaction is an exothermic polymerization process creating a highly cross-linked network. The curing mechanism is divided into 2 main steps: gelation and vitrification as shown on Figure 11.

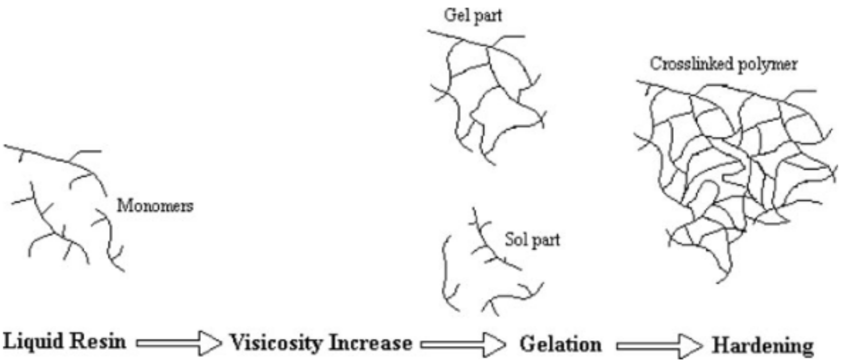

Figure 11. The cure mechanism [27]

Gelation is a nonreversible event where the viscosity increases rapidly due to formation of a cross-linked polymer network and the processability decreases dramatically. Two phases coexist: gel phase and sol phase. The sol phase remains soluble in the solvent while the gel phase is the phase already gelled and which has become insoluble. Gelation is the transformation from a viscous liquid to an elastic gel or rubber. As the reaction goes on, the sol phase proportion decreases, and the resin starts to have a solid shape.

Vitrification is a thermo-reversible process corresponding to the transition from liquid to glassy state. The transformation rate decreases, and the reaction becomes controlled by diffusion of reactive species. Vitrification is also an important event because it determines the final degree of conversion achieved. It controls the properties and the durability of the cured polymer. Indeed, the inhomogeneity of the cured polymer is determined by this process [27].

As discussed previously, the resin is composed of different species. The prepolymers forming the polymer network after reactions give the bulk properties of the material while diluents are added to change properties of the resin to make processability easier (decreasing viscosity, modifying hardness or glass transition temperature). Photoinitiators are of particular importance because they control the reaction rate. Two types of photoinitiators exist:

- *Radical initiators* (figure 12): they absorb incident light and form radicals. The radicals attack double bonds in the monomer. The reaction takes place until a termination process occurs when the species lose their activity by coupling of two radicals. This process in sensitive to oxygen since radicals can be captured by oxygen.
- *Cationic initiators* (figure 13): they initiate the polymerization process by forming an acidic molecule under light exposure. Onium salts are often used to form $H^+$ which then reacts with double bonds of the polymer. This process is not sensitive to oxygen. Moreover, control of cationic polymerization degree is more difficult because the reactions can keep on after the light is switched off [28].

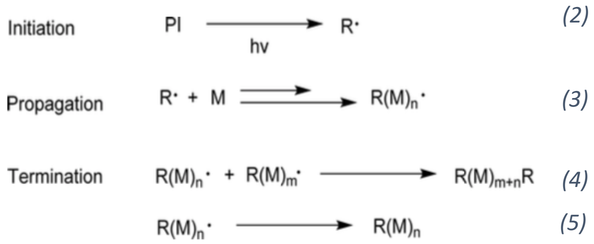

Figure 12. Schematic illustration on initiation, propagation and termination of radical photopolymerization [28]

$$\text{Initiation} \quad Ar_3S^+X^- \xrightarrow[hv]{} Ar_2S + Ar^+X^- \text{ or } Ar^{\bullet} + Ar_2S^{\bullet +}X^- \tag{6}$$

$$Ar^+X^- \text{ or } Ar_2S^{\bullet +}X^- \xrightarrow[RH]{} H^+X^- + \text{additional products} \tag{7}$$

$$\text{Propagation} \quad H^+X^- + M \rightrightarrows H(M)_n{}^+X^- \tag{8}$$

*Figure 13. Schematic illustration on initiation and propagation of cationic photopolymerization (triarylsulfonium salt as an initiator) [28]*

### Stereolithography adapted to ceramic 3D printing

This multistep technique (figure 14) can also be used to print component made out of metals or ceramics. The ceramic or metal powder is mixed with a specific resin to act as a binder and the resin is then removed. Ceramic particles are inert and do not react during the SLA process. The ceramic stereolithography (CSL) have additional steps compared to conventional SLA. Firstly, the photocurable polymer resin polymerized under light exposure and forms a polymer network enclosing the ceramic particles. The component is called *green body*. The cured resin is then removed by an appropriate thermal treatment: this is the debinding step. The piece is finally sintered to improve its properties [29].

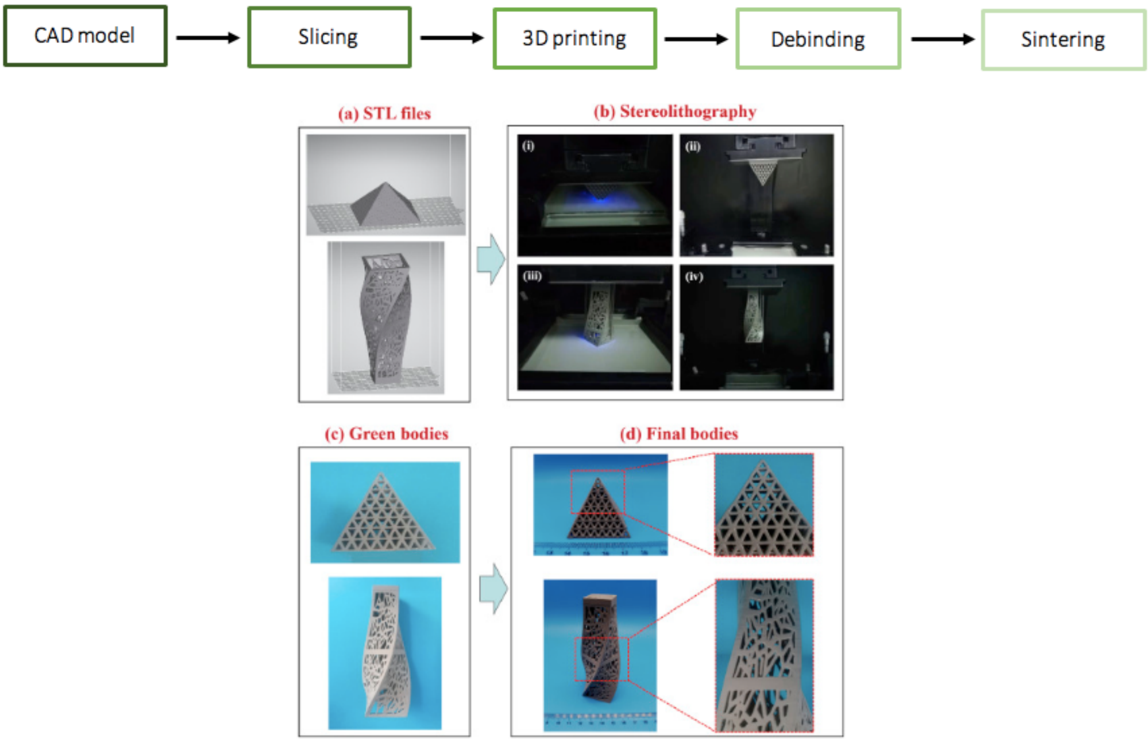

*Figure 14. Steps of Ceramic Stereolithography [30]*

Addition of ceramic particles cause disturbance due to light scattering. The cure depth is then strongly influence by the particle size and the light scattering. Moreover, adding ceramic particles leads to an increase of the viscosity that can impede a good control of the CSL process. To achieve a good processability and complex shape, the resin must be fluid enough and the upper limit (3 Pa.s with shear rates of 10 $s^{-1}$ ) corresponds usually to a maximum ceramic loading of less than 50 vol.%. The influence of the particle size has also been studied. The Figure 15 shows that a special balance between coarse and fine particles have to be met to achieve the require viscosity [28].

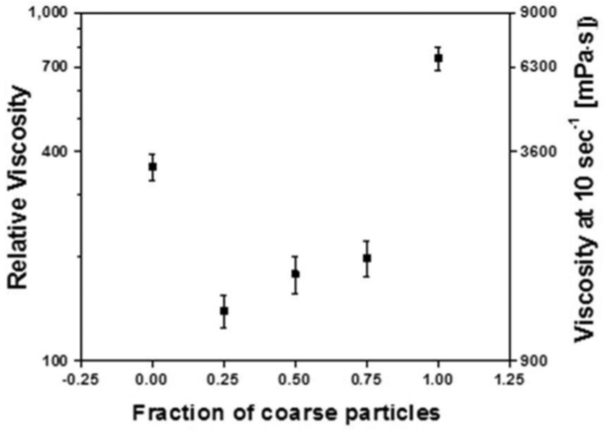

*Figure 15. Effect of particle size distribution on the relative viscosity of suspension. 60 volume percentage of silica dispersed suspensions are prepared by two different particle sizes; coarse ($d_c$: 26 µm) and fine ($d_f$: 7 µm) fused silica suspensions [28]*

The table 9 summarises advantages and disadvantages of stereolithography.

*Table 9. Advantages and disadvantages of stereolithography*

| Advantages | Disadvantages |
|---|---|
| • Good surface finish<br>• More accurate and complex shape can be produced by this technique<br>• Can produce small parts with high precision but also large parts whilst maintaining a high precision<br>• No mould required, only a CAD model | • Requires specific polymeric resins and additives<br>• Multistep process lasting several hours<br>• Expensive process<br>• Difficult to achieve high density<br>• Complex curing process and complex kinetics<br>• Smaller (down to nano) particle size is preferred |

### 2.3.2.3 Digital Light Processing

#### Principle

Digital Light Processing (DLP) is a VAT Polymerization technique. This process is closely linked to SLA: the main difference is the type of light source used to cure the resin. Both techniques rely on using photopolymer resins cured under light exposure. DLP process uses a digital projector screen to flash the resin and cure it layer by layer (figure 16). DLP is faster, especially for large parts, than SLA because it can cure one layer at one time while SLA cures the resin point by point with a laser. The light projected is directed with a Digital Micromirror Device (DMD) to the tank filled with resin. The DMD is made of thousands of micromirrors that can be tilted independently to be turned ‘on’ or ‘off’. When the light hits the resin, one layer is cured accordingly to the 3D sliced model. The tank of resin is then moved up or down of one layer to keep on curing and produce the desired part.

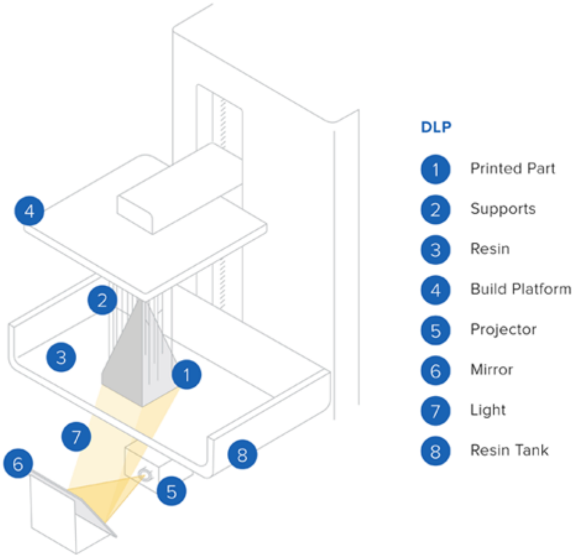

*Figure 16. Schematic diagram of DLP printer [31]*

As for SLA, the technique can be used for ceramics by mixing photopolymerizable resin with a ceramic powder. The printing stage is then followed by debinding stage to remove the resin and by sintering stage to increase the cohesion of the ceramic powder and its mechanical properties.

The XY resolution of DLP depends on the resolution of the projector since it is the size of the pixel, generally between 35 to 100 μm. DLP offers high accuracy like SLA. Calibration is important to deal with non-uniform light distribution due to optical distortion of lenses. Besides, as parts are used based on voxels, curved lines will appear as steps and might cause stress concentration (figure 17). However, it is on a very small scale.

*Figure 17. Effect of voxels on curved lines [31]*

### Applications with lunar soil simulants

DLP has already been studied for lunar applications. Researchers from China studied the feasibility of this technique with the simulant CLRS-2, whose composition is given in Table 2. Liu and al. [11] compared samples of different layer thickness (25, 50 and 100 μm) fabricated in three different exposure time (30 s, 60 s, 150 s) and sintered in air. The powder was grinded to reduce the particle size in order to achieve good properties for the slurry used in DLP: before grinding, $d_{50}$ was 60.6 μm and after grinding it was reduced to 15.3 μm. DLP offers the possibility of high dimensional accuracy and good surface finish as proved by the manufactured parts shown on figure 18. The samples after sintering underwent a homogeneous shrinkage, and no defects or cracks were visible on the printed and sintered samples. It was also observed that the shrinkage was higher with the increasing layer thickness.

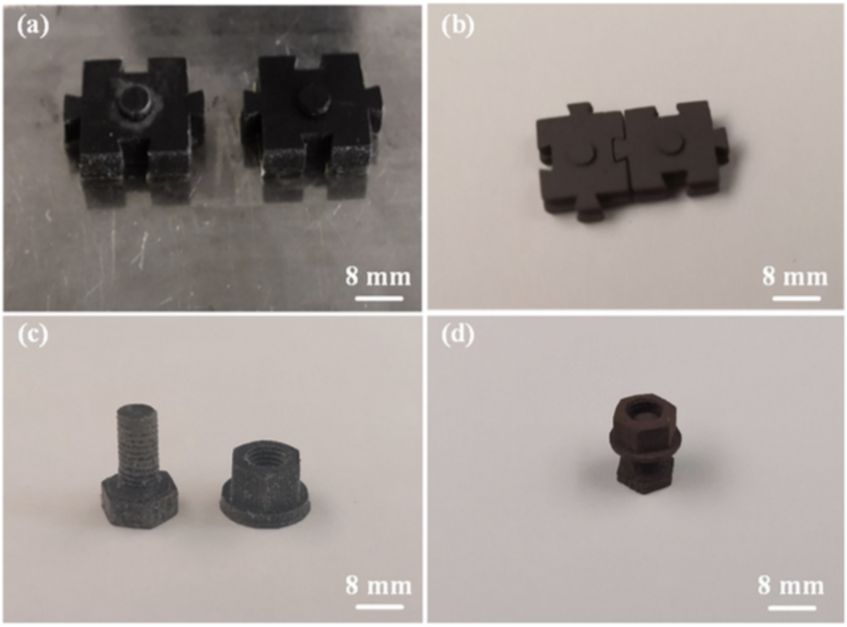

*Figure 18. The pictures of (a, c) the DLP 3D printed CLRS-2 components and (b, d) the corresponding sintered components with the layer thickness of 100 µm [11]*

During sintering, no major phase changes were observed: only a slight decrease in the content of amorphous phases were observed (figure 20) and might be explained by the low cooling rate which lets phases crystallize. Moreover, temperature did not show significant influence: a mass change of less than 1 % was measured up to 1300 °C. The mass change is related to the evaporation of volatile constituents like water or sulfur dioxide but is also due to the oxidation of iron (figure 19).

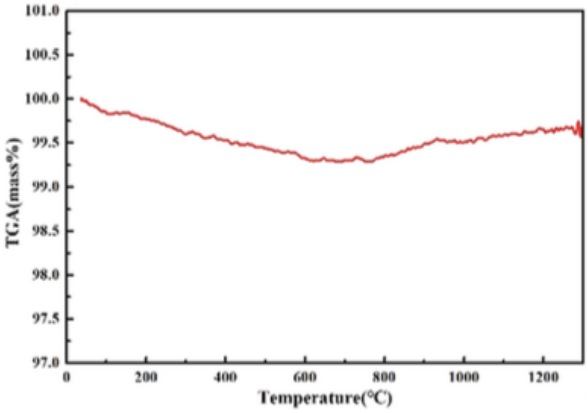

*Figure 19. TGA of CLRS-2 regolith simulant [11]*

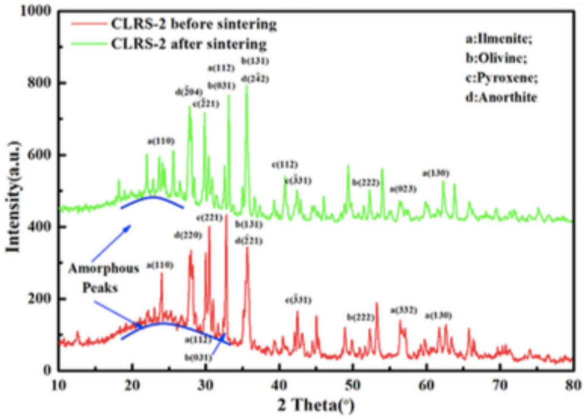

*Figure 20. XRD patters of CLRS-2 regolith simulant before and after sintering [11]*

Liu and al. [11] reported that sedimentation can occur with slurry of coarser particles and they observed especially sedimentation for the 100 μm thick samples since the exposure time was higher. Moreover, the mechanical properties (compressive strength and flexural strength) were higher with decreasing layer thickness. This improvement in mechanical properties might be due to smaller pores size in the samples of thinner layers. The higher mechanical properties in this work compared to other research is also related to the specific composition of the simulant. The composition of CLRS-2 offers good potential for this technique because slower evaporation leads to less pore formation [11].

The effect of the sintering environment on the properties of CLRS-2 lunar simulant samples fabricated via DLP was studied by Dou and al. [32]. They used a powder with an average particle diameter of 15.3 μm. They fabricated samples with layer thickness of 50 μm and sintered the samples in either air or Ar and either at 1100 °C or at 1150 °C. Air-sintered samples showed higher shrinkage than Ar-sintered samples, and shrinkage increases with increasing temperature. Complex phases changes were observed in both sintering environments. One important observation for Ar-sintered samples was the transformation of ilmenite into metallic iron and rutile that allows these samples to be transported by magnets since they are paramagnetic.

Mechanical properties of the samples increased with increasing temperature regardless of the sintering environment (table 10). The samples air-sintered at 1150 °C have the better mechanical properties and it must be related to the melting of minerals during processing which bound the particles together. Furthermore, liquid phase sintering was only observed for the air-sintered sample at 1150 °C which explains the increase in mechanical properties.

*Table 10. Mechanical properties of sintered CLRS-2 regolith simulant [32]*

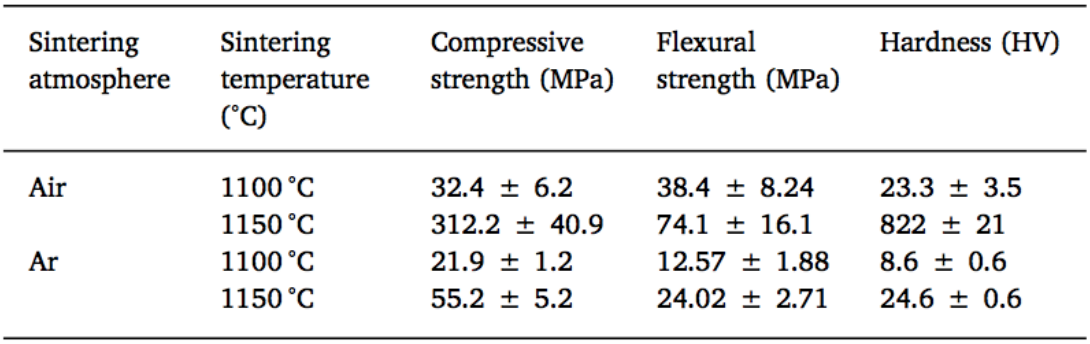

| Sintering atmosphere | Sintering temperature (°C) | Compressive strength (MPa) | Flexural strength (MPa) | Hardness (HV) |
|---|---|---|---|---|
| Air | 1100 °C | 32.4 ± 6.2 | 38.4 ± 8.24 | 23.3 ± 3.5 |
| | 1150 °C | 312.2 ± 40.9 | 74.1 ± 16.1 | 822 ± 21 |
| Ar | 1100 °C | 21.9 ± 1.2 | 12.57 ± 1.88 | 8.6 ± 0.6 |
| | 1150 °C | 55.2 ± 5.2 | 24.02 ± 2.71 | 24.6 ± 0.6 |

To conclude, DLP is a promising technique for lunar applications. It offers high accuracy, good surface finish and also, allows fabrication of samples with mechanical properties high enough for space habitats. Properties of materials can be increase by decreasing the layer thickness and increasing sintering temperature. Chemical composition plays an important role and must be taken into account while considering lunar soil regolith.

### 2.3.2.4 *Selective Laser Melting (SLM)*

#### Principles

Selective Laser Melting (SLM) is a powder based additive manufacturing process. The parts are built layer by layer thanks to a high-energy beam directed on the powder bed and controlled with computer (figure 21). In this process, the particles are fully melted and then solidified to form a component [29]. To perform SLM, process parameters and materials properties have to be studied to optimize the technique for each specific application. The main process parameters involved in SLM are scanning velocity, laser power, spot beam size, laser wavelength, hatch distance … Besides these parameters, the choice of the substrate plate and its temperature, the powder size or the inert gas are important to achieve good results.

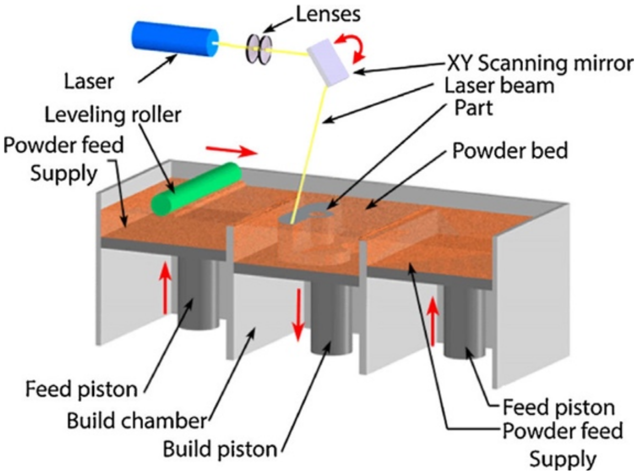

*Figure 21. Schematics of additive manufacturing (AM) by selective laser melting (SLM) [33]*

It is widely used to 3D-print metallic parts, but efforts are done to use SLM for ceramics powders since no post-processing treatments are required with SLM. Nevertheless, important limitations exist for ceramic applications of this technique. They are cited below [29]:

- Cracks induced by huge temperature difference during the processing due to very short period of interaction between laser and ceramic powder
- Low flowability of ceramic after melting impeding the formation of a compact layer
- Porosities form due to insufficient melting and are detrimental for the mechanical properties of the ceramic parts
- Balling effect, which is an unfavourable defect due to poor wetting between the molten liquid and the solidified layer, might occur due to low conductivity of ceramic powder

The advantages and disadvantages of SLM are summarised in the table below.

*Table 11. Advantages and disadvantages of SLM*

| Advantages | Disadvantages |
|---|---|
| • Can produce high quality components in low to medium quantities<br>• Good repeatability<br>• Complex shape can be manufactured<br>• Low waste compared to conventional techniques (no machining)<br>• Production of nearly full dense parts | • Residual stresses (cracking)<br>• Porosity (requires post-processing treatments)<br>• Lack of knowledge about the interaction between laser and ceramics<br>• Powder sieving or crushing is required<br>• Slow process<br>• Powder heterogeneity causes variations in energy density |

### Lunar applications

Fateri and Gebhardt [1] studied the optimization of SLM parameters to print lunar soil simulant. For their study, they used the simulant JSC-1A whose composition is given Table 2 and close to the composition of lunar mare areas regolith. JSC-1A has a wide range of particle sizes as shown on the Figure 22. In SLM, the energy density per unit mass is directly affected by the variation of the particles size and can cause heterogeneous structure. The JSC-1A powder was thus filtered to use particles of diameter smaller than 63 μm to homogenise the energy absorption. Moreover, the particles exhibit irregular shape. The granular particles cannot be spread smoothly and heterogeneity in mass distribution are then inevitable. The heterogeneity in voids and mass distribution cause variation of energy density during SLM. Conversely, the composition of the particles is relatively homogeneous, and they are mainly composed of silicon, aluminium, calcium and oxygen.

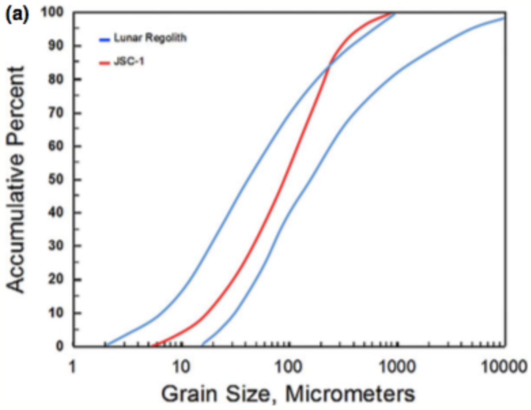

*Figure 22. Particle size distribution of the JSC-1A and lunar regolith [1]*

Fateri and Gebhardt used a SLM machine with an Yb:YAG fiber laser whose wavelength is 1070 nm. The absorption unit of the JSC-1A simulant is 1.1 at this wavelength, which corresponds to an absorption rate of 92.06 % according to Lambert-Beer law. They started by manufacturing a cubed sample of 10 mm x 10 mm x 3 mm using a power of 50 W and a scan speed of 50 mm/s. They optimized the layer thickness with some attempts to reduce as much as possible the re-exposure area and a thickness of 100 to 300 μm was chosen. The authors proved that using SLM transforms the crystalline structure of the powder into an amorphous structure (Figure 23 and Figure 24).

SLM process was also studied by other authors. Goulas and al. [34] studied the properties of JSC-1A manufactured with a SLM machine using an Yb fiber laser (wavelength of 1,06 – 1,09 μm, maximum power of 50 W, laser spot diameter of 80 μm). These authors observed the same peaks as for the raw powder telling that no significant change in crystalline phases occurred, but these peaks were wider. They concluded that more amorphous phases were present. Thus, SLM parameters might influence the amorphization of phases.

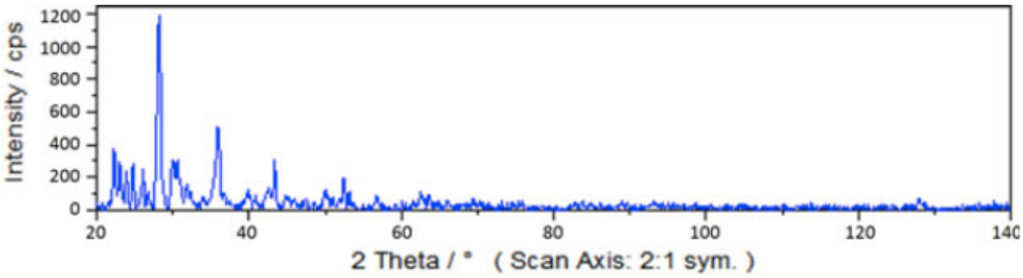

*Figure 23. X-Ray diffractogram of lunar simulant (CuK$\alpha$ radiation) [1]*

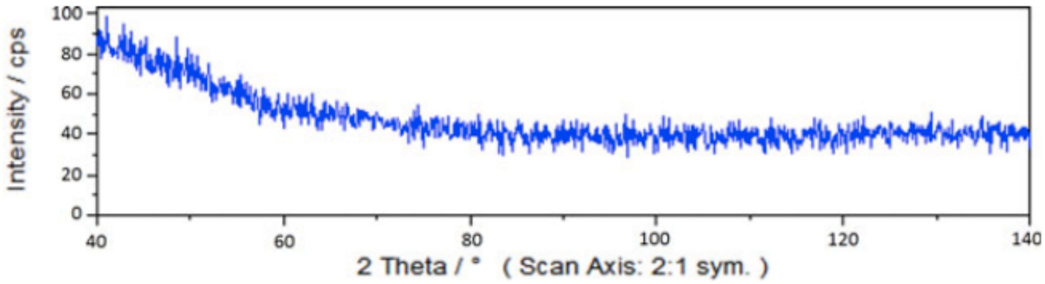

*Figure 24. X-Ray Diffractogram of fabricated SLM process parts using lunar regolith simulant (CrK$\alpha$ radiation) [1]*

The hardness measured via nanoindentation was HVIT = 1245 Vickers which is 44 % higher than the value of a reference fused silica part using the same equipment. The parts exhibit an average surface roughness of Ra of 1.5 $\mu$m and Rz of 7.5 $\mu$m.

Goulas and al. [34] found a microhardness of 660 HV for their SLM samples. Both researchers used the same simulants but different techniques to measure the hardness. We can conclude that both samples have high hardness, but it must be noted that nanoindentation is a local measurement of hardness while micro-indentation gives an average value of hardness.

The authors [1] used the SLM technique to build other parts such as net shape matrix objects (figure 25), nuts or gears to prove the promising feature of this technique. These parts have high surface hardness but show brittle behavior which might be improve by post-processing treatments.

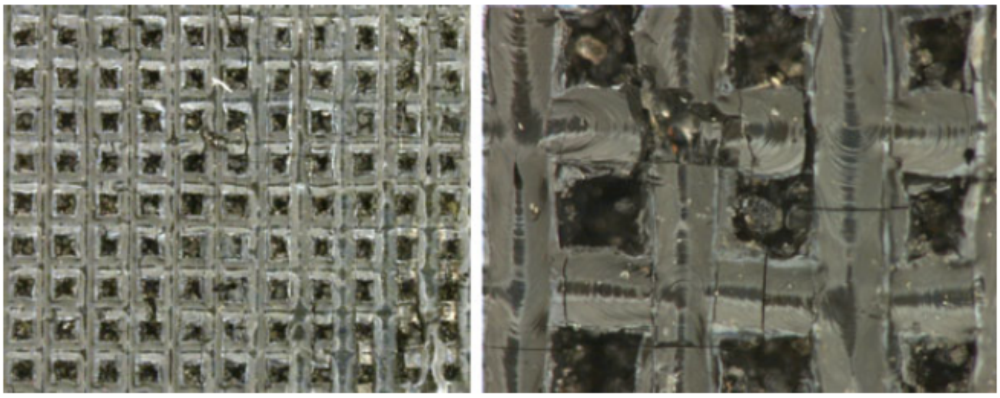

*Figure 25. Net shape matrix object with cubic walls of 200 $\mu$m x 200 $\mu$m and cubic gaps of 250 $\mu$m x 250 $\mu$m fabricated from JSC-1A using SLM [1]*

Moreover, Goulas and al. [34] showed that no large mass loss occurred during SLM of the lunar regolith samples (figure 26). The slightly loss of mass might be related to moisture evaporation and the oxidation of iron also contributes to a small increase of the mass.

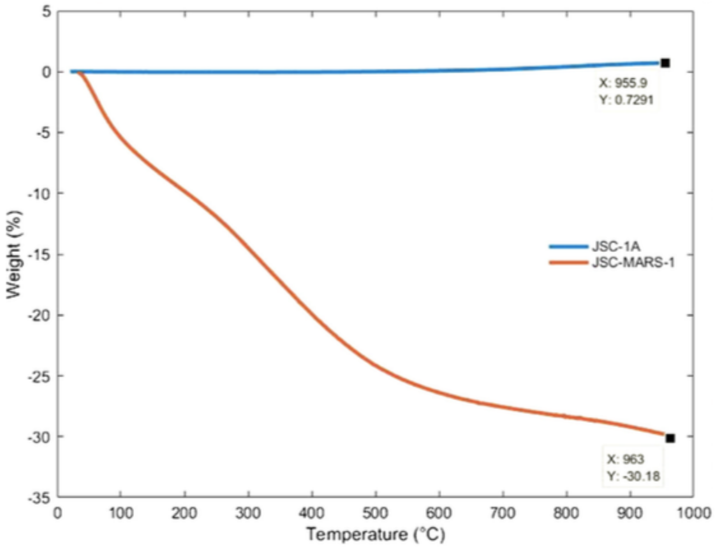

*Figure 26. TGA curves overlay of Lunar and Martian regolith simulants [34]*

### *2.3.2.5 Solar sintering*

Using additive manufacturing on the Moon is promising, but the different processes need devices brought from earth. Using the Sun as a source of energy will give an unlimited source of energy already available on the Moon. Researches have been done on the feasibility of 3D-printing with solar energy.

Meurisse and al. [9] studied the feasibility of solar sintering. They started by using a concentrated sunlight in a solar furnace facility in Köln and sintered regolith simulant. They did 1D and 2D sintering experiments to prove the concept and the instability of the light source caused poor sintering. Figure 27 shows the inhomogeneity of the sintering in a 2D part.

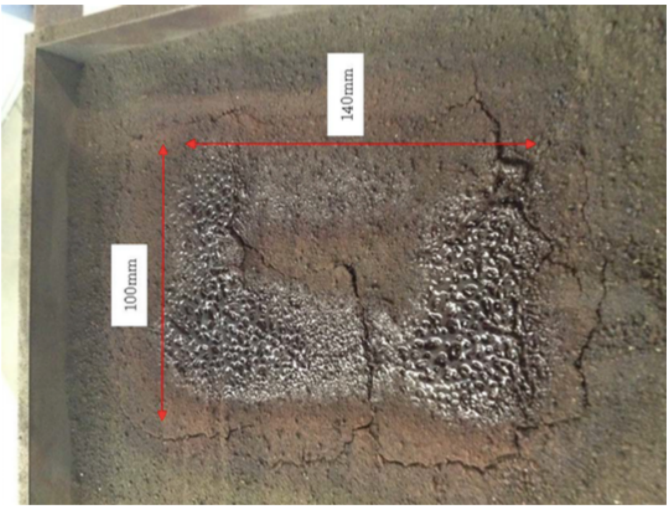

*Figure 27. 2D unhomogeneously sintered part of as-received JSC-1A regolith simulant [9]*

They studied the technique with Xenon light to have a stable light source with the same spectrum as solar light. The authors managed to form “bricks” with a speed of 48 mm/s: a higher speed lead to formation of too loosely sintered parts. Nevertheless, many challenges appeared. Long sintering process leads to high thermal stresses in the parts because of the slow sintering speed and the high cooling rate at the edges of the crucible. It can be improved by sintering the successive layers one along the length and one along the width.

Moreover, the parts were weak and sintering process had to be improved to be promising. Tomography (figure 28) and SEM images showed open pores up to 0.60 mm preventing from good bonding between layers. Closed pores were also visible and due to melting during sintering. The melt does not embed surrounding grains, and this can explain why overlaid layers are poorly bonded. They also proved that the strength of the parts is only related to bonding between successive layers and that densification was negligible to enhance the strength.

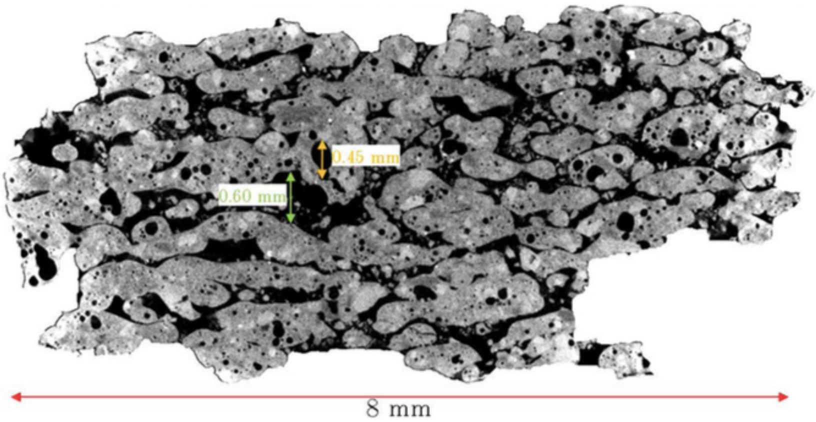

Figure 28. Tomography of a 3D printed brick sample [9]

After solar sintering feasibility has been proven [9], Fateri and al. studied solar sintering under vacuum and compared with solar sintering under ambient conditions [1]. They managed to sinter parts under ambient conditions with a compressive strength of 2.49 MPa and a Young's modulus of 0.21 GPa. However, when applying the same process parameters under vacuum, the layers melted completely due to lack of air convection. They changed the process parameters by lowering the beam intensity from 1.2 MW/m² to 1 MW/m² and by increasing the scanning speed from 47 mm/s to 65 mm/s to manufacture sintered parts. AM parts under vacuum had more pores and exhibited a foamy structure (figure 29). The structure might be due to outgassing of the grains when partially molten. Moreover, the density was lower for the parts sintered under vacuum that confirms the higher porosity and the foamy structure.

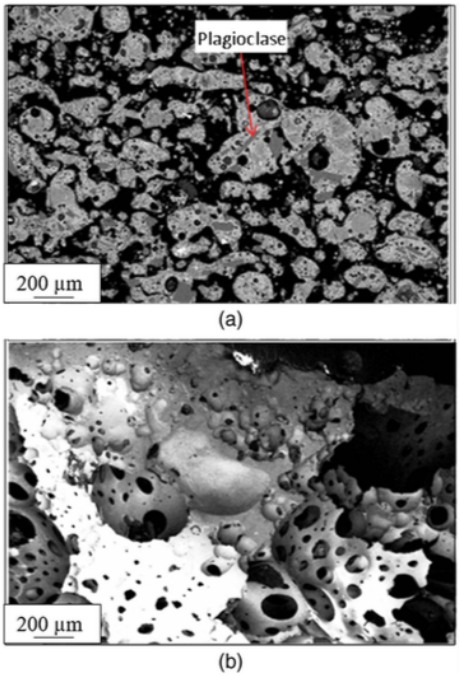

Figure 29. SEM back-scattered image of AM solar sintered regolith in (a) air; and (b) vacuum [1]

These two studies confirm that solar sintering is a promising alternative for lunar applications. However, the parts manufactured showed mechanical properties that should be improved to be suitable for space habitats. Table 2 summarises the advantages and disadvantages of solar sintering.

*Table 12. Advantages and disadvantages of solar sintering*

| Advantages | Disadvantages |
|---|---|
| • Use of solar light source, more stable on the Moon<br>• No need of binders | • Difficulty when sintered under vacuum<br>• Low mechanical properties<br>• Poor bonding between successive layers<br>• Difficult to balance sintered and molten phases<br>• No prediction on the equipment lifetime<br>• Few investigations carried out on this technique |

#### 2.3.2.6 D-shape process

A novel 3D-printing process have been studied as an alternative for lunar space habitats. Cesaretti and al. [7] studied the feasibility of building a whole structure with this new technique. They started with a design study taking into account the harsh lunar environment and then, they implemented the technique with the lunar simulant DNA-1 (Table 2).

The D-shape process consists of a printing head that is moved in a x-y frame to print the desired feature previously modelled on computer. A liquid binder is sprayed over the granular material on the desired areas to be bound: the salt binder reacts chemically with the metal oxides. The reaction is exothermic, and the granular material is segregated in a matrix generated via a reticulation process.

For vacuum purpose, they re-designed the D-shape process. Indeed, it was needed to keep the ink in gaps smaller than 200 μm and so the ink must be injected directly inside the regolith and not sprayed on top of it. The lunar regolith has enough small particles to keep the gaps between particles in this order of magnitude (at least 48 % of particles must be smaller or equal to 200 μm in a packed volume to achieve gaps smaller than 200 μm [7]).

The regolith was mixed with MgO because DNA-1 does not contain enough MgO to promote reactions with the ink made of water (77 %) and dry salts. Lunar regolith has a higher content of MgO than DNA-1 but it may still be too low to react without addition of MgO. The manufactured parts were porous and anisotropic (Figure 30, table 13 and 14).

*Table 13. Mechanical properties of the D-shape regolith samples [7]*

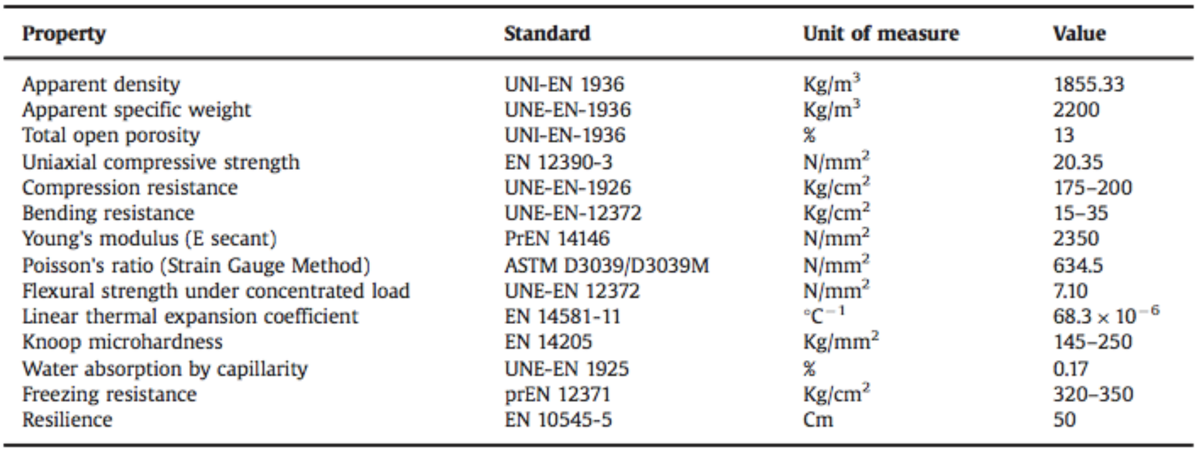

| Property | Standard | Unit of measure | Value |
|---|---|---|---|
| Apparent density | UNI-EN 1936 | Kg/m$^3$ | 1855.33 |
| Apparent specific weight | UNE-EN-1936 | Kg/m$^3$ | 2200 |
| Total open porosity | UNI-EN-1936 | % | 13 |
| Uniaxial compressive strength | EN 12390-3 | N/mm$^2$ | 20.35 |
| Compression resistance | UNE-EN-1926 | Kg/cm$^2$ | 175–200 |
| Bending resistance | UNE-EN-12372 | Kg/cm$^2$ | 15–35 |
| Young's modulus (E secant) | PrEN 14146 | N/mm$^2$ | 2350 |
| Poisson's ratio (Strain Gauge Method) | ASTM D3039/D3039M | N/mm$^2$ | 634.5 |
| Flexural strength under concentrated load | UNE-EN 12372 | N/mm$^2$ | 7.10 |
| Linear thermal expansion coefficient | EN 14581-11 | °C$^{-1}$ | 68.3 × 10$^{-6}$ |
| Knoop microhardness | EN 14205 | Kg/mm$^2$ | 145–250 |
| Water absorption by capillarity | UNE-EN 1925 | % | 0.17 |
| Freezing resistance | prEN 12371 | Kg/cm$^2$ | 320–350 |
| Resilience | EN 10545-5 | Cm | 50 |

XRD measurements did not provide enough inside to tell whether the regolith reacted during processing.

*Figure 30. (a) 3D drawing of the convex artifact, (b) unpolished printed piece built using the DNA-1 simulant (395 mm x 395 mm x 195 mm) and (c) particular of the artifact surface after dust removal [7]*

*Table 14. Advantages and disadvantages of D-shape process*

| Advantages | Disadvantages |
|---|---|
| • Allows large scale manufacturing in one single printing process<br>• No need of sieving or crushing of the lunar soil regolith | • A huge printer must be brought to the Moon<br>• Use of an inorganic binder and an ink<br>• Delamination and low shape accuracy<br>• Expensive |

## 2.3.3 Overview of all consolidation techniques

The following table 15 clusters all the advantages and drawbacks of the different techniques discussed previously. It gives a quick overview of all the techniques to compare them.

*Table 15. Summary of the advantages and drawbacks of the different techniques used to consolidate lunar regolith.*

| Consolidation techniques | | | Advantages | Disadvantages | FGMs Feasibility |
|---|---|---|---|---|---|
| Additive Manufacturing | Material Extrusion | Sulfur Concrete [35] [36] | • Easiness of the manufacturing<br>• Presence of FeS on the Moon<br>• Cheap process | • Feasibility of extraction from ores<br>• Low impact resistance<br>• Relatively high rate of sublimation of sulfur | - |
| | Power Bed Fusion | Selective Laser Melting [1] [34] | • Can produce high quality components in medium quantities<br>• Good repeatability<br>• Complex shape can be manufactured<br>• Low waste Nearly full dense parts | • Residual stresses (cracking)<br>• Porosity (requires post-processing treatments)<br>• Interaction between laser and ceramics<br>• Powder sieving or crushing is required<br>• Slow process<br>• Powder heterogeneity causes variations in energy density | + |
| | | Solar Sintering [9] [37] | • Use of solar light source, more stable on the Moon<br>• No need of binders | • Difficulty when sintered under vacuum<br>• Low mechanical properties<br>• Poor bonding between successive layers<br>• Difficult to balance sintered and molten phases<br>• No prediction on the equipment lifetime<br>• Few investigations carried out on this technique | + |
| | Binder Jetting | D-shape Process [7] | • Large scale single step printing<br>• No need of powder sieving/crushing | • A large and expensive printer<br>• Use of an inorganic binder and an ink<br>• Delamination and low shape accuracy | - |
| | Photopolyme-rization | Stereolithography [28] [27]/ Digital Light Processing [32] [31] [11] | • Good surface finish<br>• More accurate and complex shape can be produced by this technique<br>• Small and large parts with high precision<br>• No mould, only a CAD model | • Requires specific polymeric resins and additives<br>• Multistep process lasting several hours<br>• Expensive process<br>• Difficult to achieve high density<br>• Complex curing process and complex kinetics<br>• Smaller (down to nano) particle size is preferred | + |
| Conventional or hybrid fabrication | | Spark Plasma Sintering [17] [13] | • Microstructure control due to low temperature and short time<br>• High density due to higher heating rate and pressure<br>• Sintering dissimilar materials<br>• Fast and FGMs can be produced<br>• Cost of SPS is 50 – 80% lower than other sintering techniques<br>• 900°C enough to sinter regolith<br>• Good mechanical properties | • Only simple symmetrical shape can be prepared<br>• Expensive DC generator required<br>• For very small powder (less than 100 nm), significant temperature gradient can lead to non-uniform densification<br>• Sieving or crushing needed for lunar soil regolith<br>• Limited to simple shapes | + |
| | | Vacuum Sintering [19] | • Parts with low therm. conductivity<br>• Prevention of oxidization | • High weight loss increasing with temperature<br>• Presence of macro-pores<br>• Shrinkage dependent on the temperature | + |
| | | Thermite reactions [20] [21] | • Reduction of energy needed<br>• Limited equipment is required<br>• Quick reactions with smaller particles | • Addition of Al or other substances<br>• Porous structures<br>• Little information about mechanical properties<br>• Sieving or crushing required for lunar regolith<br>• Deformation and surface cracking (even more with smaller particles) | - |

The choice of consolidation techniques for lunar regolith is very broad. They all offer different advantages and promising results. However, some main drawbacks disregard some of them for the current research. SPS, DLP and laser scanning (as single bead alternative to laser based powder bed fusion AM technique) have been thus chosen for their easiness, feasibility for FGM and ability to produce parts with good properties.

## 2.4 Functionally Graded Materials

### 2.4.1 Introduction

Functionally graded materials (FGM) are a class of advanced materials characterized by spatially variation in composition across the volume, contributing to corresponding changes in material properties in line with the functional requirements [38]. They have been created to replace composites for specific applications. Composites appeared to fail under harsh working conditions, since they are strongly dependent on the properties of the interfaces between the fibers and the matrix. The interface is suppressed in the FGMs and so they do not suffer from the same failures as for composites [39].

FGMs offer many advantages compared to composites or conventional alloys. They are designed for specific applications and they allow to benefit from the different used materials. As shown in Figure 31, the properties varies along the material without sharp change causing high stresses and which may lead to brutal failures. FGMs are materials that meet different functionalities: corrosion resistance, wear resistance, control of deformation, high mechanical properties, …

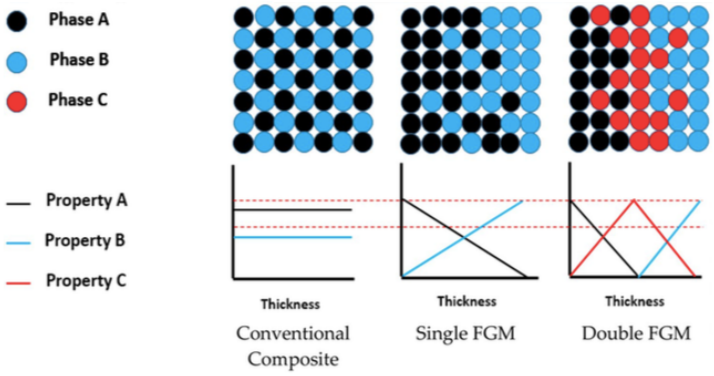

*Figure 31. Variation of properties in conventional composites and FGMs [40]*

FGMs is a new type of materials. It was first introduced in 1984 when researchers in Japan needed to find a material for a space plane project. They needed to manufacture a material able to withstand a temperature gradient of about 1000 K, with a maximum temperature of 2000 K. They tested composites in these working conditions, and they all failed at the interface. Researchers decided to gradually add the second material into the first material to avoid this sharp interface. They referred to their gradient-interface material as a functionally graded material.

Different types of FGMs exist nowadays. The most common way to classify them is shown on Figure 32 and the three mains classes will be discussed further below.

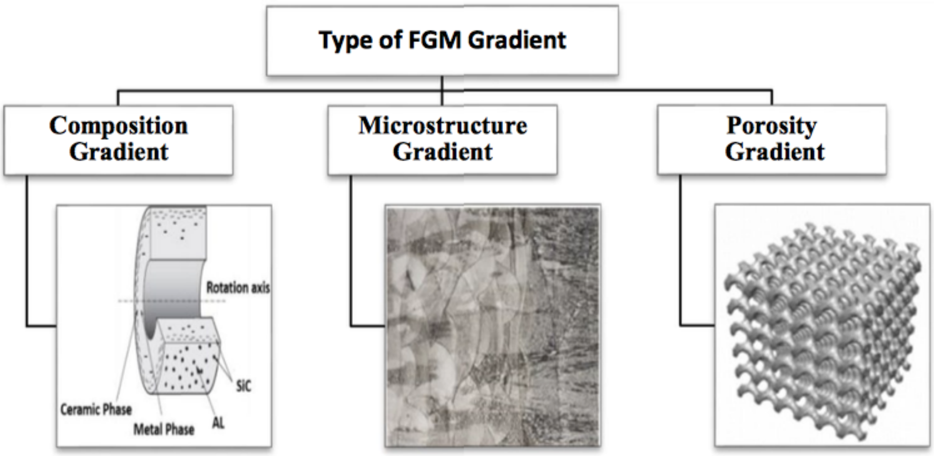

*Figure 32. Three different types of FGM [40] [41]*

### 2.4.2 Types of Functionally Graded Materials

- Chemical Composition Gradient: a material where the chemical composition varies gradually along a direction. It can be achieved with single phase or a multiphase material [42] (Figure 33).

In the case of a single phase material, the chemical composition gradient is related to a difference in solubility of elements of one phase in the other phase and it often occurs during sintering process.

In the case of multiphase material, the chemical composition and phases vary across the bulk of the material. It is made by varying the proportion of the different materials used to achieve a gradient of composition as shown in the figure below.

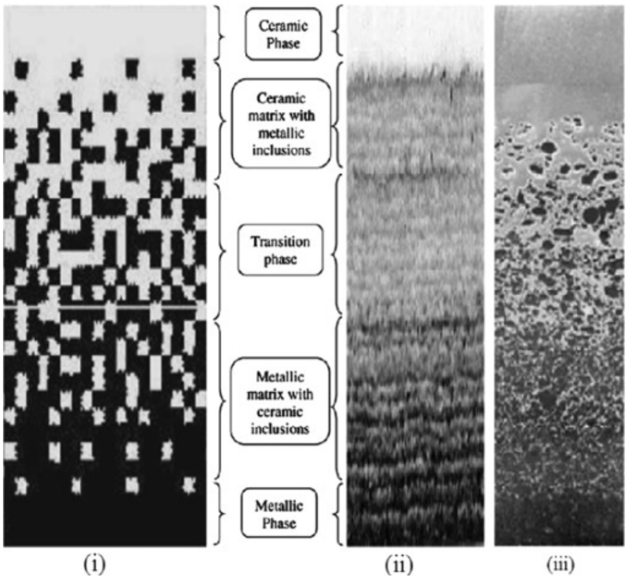

*Figure 33. Gradation of microstructure with metal–ceramic constituents (i) smoothly graded microstructure (ii) enlarged view and (ii) ceramic–metal FGM [43]*

- **Porosity Gradient**: a material in which the porosity varies along its spatial direction in the bulk material: the shape and size of the pores varied and are designed to give the material the targeted properties (Figure 34). This type of FGMs can be either porosity density gradation or pore size gradation. The influence of the powder particles size is important to achieve a gradient of porosity.

They are especially important for biomedical purposes since they mimic the natural constituents that they replace. Graded porosity materials help in the integration of the implant and for the healing processes. Moreover, porosity-graded materials reduce the overall weight of an implant and improve the modulus of elasticity to match the one of the human tissues [42].

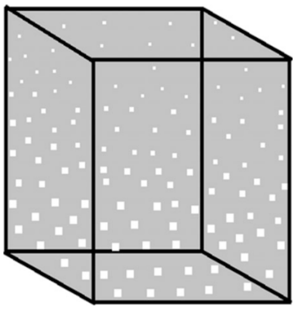

*Figure 34. Schematic diagram of porosity-graded FGM [42]*

- **Microstructure Gradient:** a material in which the microstructure changes gradually to meet the properties requirements of the material (Figure 35). This gradient of microstructure can be achieved during the solidification processes by having different cooling rates in the material. When a piece of material is quenched, its surface will undergo a solidification with a high cooling rate whereas the inner part will solidify more slowly. As a result, the surface will be hard, and the microstructure will be different in the inner part leading to other properties.

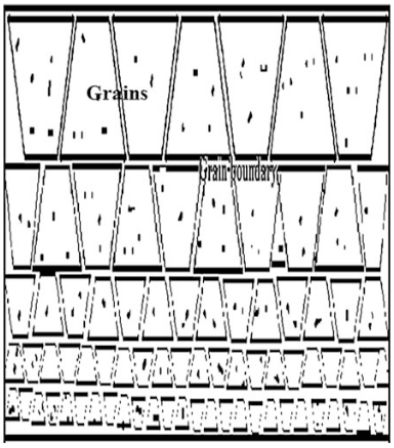

*Figure 35. Schematic diagram of graded microstructure [42]*

They are mostly used for applications when a hard surface is needed to resist wear and a tough core to resist the high impact that occurs during the operation. They are used for example for ring gears or turbines applications.

### 2.4.3 FGMs for lunar applications

FGM would be used as the outer shell of the lunar habitats. Instead of a cover made out of 100 % regolith, it may be interesting to manufacture a shell made out of lunar regolith and metal. The metal would be extracted from lunar regolith through techniques that are not currently in the scope of this research. The potential metals for FGMs are titanium, titanium alloys, steels, magnesium, aluminium and aluminium alloys. Different techniques are already used to manufacture ceramic/metal graded materials and would be studied for this specific case. Additive manufacturing or Spark Plasma Sintering would be promising in this regard.

However, some specificities and concerns should not be forgotten. FGM offer often good combination of properties but they also have drawbacks. Using dissimilar materials is not as easy as manufacturing a part made out of one material. Some concerns are listed below:

- Dissimilar materials can have very different thermal expansion coefficient and it is especially relevant in the lunar environment where the gradient of temperature is up to 200 °C. Nevertheless, by manufacturing carefully a chemical composition gradient FGM or by adding buffer layer, the mismatch can be controlled.
- Optimal manufacturing parameters (energy, environment composition, …) can be different for the different materials and a compromise must be found to optimise the process and to achieve good properties.
- Poor bonding between successive layers due to incompatibility between the materials can lead to cracking and early failure of the materials. Buffer layers can help to improve bonding between metals and ceramics to release stresses at interfaces [44].

## 2.5 Conclusions

This literature review was carried out to give an overview of the research on lunar in-situ resources utilization. Human settlements on the Moon involves the manufacturing of adequate space habitats that withstand within the harsh environment of the Moon. However, bringing building materials from Earth would be too costly for the potential outcome. Using in-situ resources is thus seen as the best option to settle humans on the Moon. Researches are undergoing to determine whether lunar regolith can be used as a construction material and to determine the most suitable manufacturing technique to build these lunar habitats. This literature review can be summarised as:

- Lunar regolith soil is the superficial dust found on the Moon. Its composition differs on location, the particles are of irregular shape and the regolith has a wide particle size distribution that must be consider in manufacturing processes.
- Additive Manufacturing techniques, also known as 3D-printing, are of particular interest because they are namely considered fast and without much waste compared to conventional techniques. Additive Manufacturing is divided into many sub-processes that offer their own advantages. However, the processing parameters have to be optimized to obtain high densification of the lunar regolith and, good mechanical and thermal properties.
- DLP is considered as a promising technique for lunar applications because no post-processing steps are needed, and good properties can be achieved after sintering. Nevertheless, this technique involves the use of a photopolymerizable resin that will have to be brought from Earth.
- SPS, as a conventional fabrication technique, is also considered for this project for its easiness and speed. However, the regolith size distribution is not optimal for the process and a crushing or sieving step will be necessary when using SPS.
- Lunar construction materials have to exhibit special properties related to the harsh lunar environment. The main properties are a good thermal fatigue resistance due to the huge gradient of temperature found on the Moon (200 K), a good impact toughness to resist meteoroids impacts and a good solar/cosmic radiation resistance to offer a good barrier towards the radiation on the Moon for humans.
- In order to achieve this combination of properties, the manufacturing of functionally graded materials is thought as an alternative. Indeed, using lunar regolith in combination with metals could lead to better properties. The outer shell will be made of lunar regolith to protect the habitat from environmental threats while the inner shell will be made of metals for additional protection and thermal properties.

## 2.6 Research objectives

Based on this literature review, the research on the feasibility of space habitats using in-situ resources is at its early stages and more in-depth knowledge is required. The main research objective of this thesis is to:
*"Investigate what is the most suitable consolidation techniques for both lunar dust and functionally graded materials (FGMs)"*

Based on the main objective the following research questions are set:

1. Determine how process parameters affect the developed microstructural and densification properties.
2. Investigate feasibility and type of FGM manufacturing and its properties.
3. Simulate selected manufacturing process to analyse the thermal properties of the materials in order to understand the relations between processing parameters and the material characteristics.
4. Provide a link to actual lunar applications based on material constraints.

# 3 Materials and Methods

## 3.1 Materials

### 3.1.1 Characterisation of the lunar regolith simulants powder

Three regolith simulants were evaluated for manufacture of a functionally-graded material: EAC-1A, LHS-1 (Lunar Highlands Simulant) and LMS-1 (Lunar Mare Simulant). Selection of these simulants is based on resemblance to Apollo sample bulk chemistry, and mineralogical diversity of the location (Mare and Highlands). EAC-1A simulant was sourced from the European Astronaut Centre, Cologne, Germany; LHS-1 and LMS-1 simulants were sourced from CLASS Exolith Lab, Orlando, USA [45] [6].

#### *3.1.1.1 Bulk chemistry and mineralogy*

Use of simulant powders for the current study is necessary due to the limited availability of lunar soil. While Apollo missions and robotic lunar landers are the benchmark for simulant development, some differences between the terrestrial simulants and the actual lunar material are to be expected. Table 16 and table 17 show that the oxide and mineralogical compositions of the chosen simulants can be considered comparable to Apollo lunar samples. Lunar Highlands soils are predominantly comprised of anorthosite, a rock which is largely made up of plagioclase feldspar. Lunar Mare soils contains volcanic rock that erupted at the lunar surface and produced lava flows and pyroclastic deposits [46]. Figure 36 shows XRD analysis of the three simulants: EAC-1A, LHS-1 and LMS-1, and confirms the presence of plagioclase, pyroxenes and iron oxide.

*Table 16. Oxide composition (given in wt%) of three lunar regolith simulants (EAC-1A, LHS-1, LMS-1 [47]) and the lunar Apollo samples from Mare and Highlands regions [46].*

| | EAC-1A | LHS-1 | LMS-1 | Apollo Mare | Apollo Highland |
|---|---|---|---|---|---|
| $SiO_2$ | 43.70 | 44.18 | 42.18 | 37.60 | 45.50 |
| $TiO_2$ | 2.40 | 0.79 | 4.62 | 12.10 | 0.60 |
| $Al_2O_3$ | 12.60 | 26.24 | 14.13 | 8.74 | 24.00 |
| $Cr_2O_3$ | - | 0.02 | 0.21 | 0.42 | - |
| $Fe_2O_3$ | 12.00 | - | - | 21.50 | 5.90 |
| $FeO_x$ | - | 3.04 | 7.87 | - | - |
| MgO | 11.90 | 11.22 | 18.89 | 8.21 | 7.50 |
| MnO | 0.20 | 0.05 | 0.15 | 0.22 | - |
| CaO | 10.80 | 11.62 | 5.94 | 10.30 | 15.90 |
| $Na_2O$ | 2.90 | 2.30 | 4.92 | 0.39 | 0.60 |
| $K_2O$ | 1.30 | 0.46 | 0.57 | 0.08 | - |
| $SO_3$ | - | 0.10 | 0.11 | - | - |
| SrO | - | - | - | - | - |
| $P_2O_5$ | 0.60 | - | - | 0.05 | - |
| **Total** | **98.40** | **100** | **99.56** | **99.58** | **100** |

*Table 17. Summary of mineralogical content (in wt.% ) of three lunar regolith simulants (EAC-1A, LHS-1 and LMS-1) [45] in comparison to mineralogical data from Apollo 17 samples. Note that Opaques is a mineral classification encapsulating oxides and sulphides, primarily ilmenite and iron oxide.*

| | EAC-1A | LHS-1 | LMS-1 | Apollo 17 |
|---|---|---|---|---|
| Plagioclase | 17.0 | 32.8 | 74.4 | 18.8 |
| Glass | - | 24.5 | 24.2 | 3.4 |
| Basalt | - | 19.8 | 0.5 | - |
| Ilmenite | - | 11.1 | 0.4 | - |
| Pyroxene | 22.0 | 7.5 | 0.3 | 44.6 |
| Olivine | 14.0 | 4.3 | 0.2 | 4.0 |
| Iron Oxide | 13.0 | - | - | - |
| Opaques* | - | - | - | 27.1 |
| Other | 8.0 | - | - | 1.4 |
| **Total** | **74.0** | **100** | **100** | **99.3** |

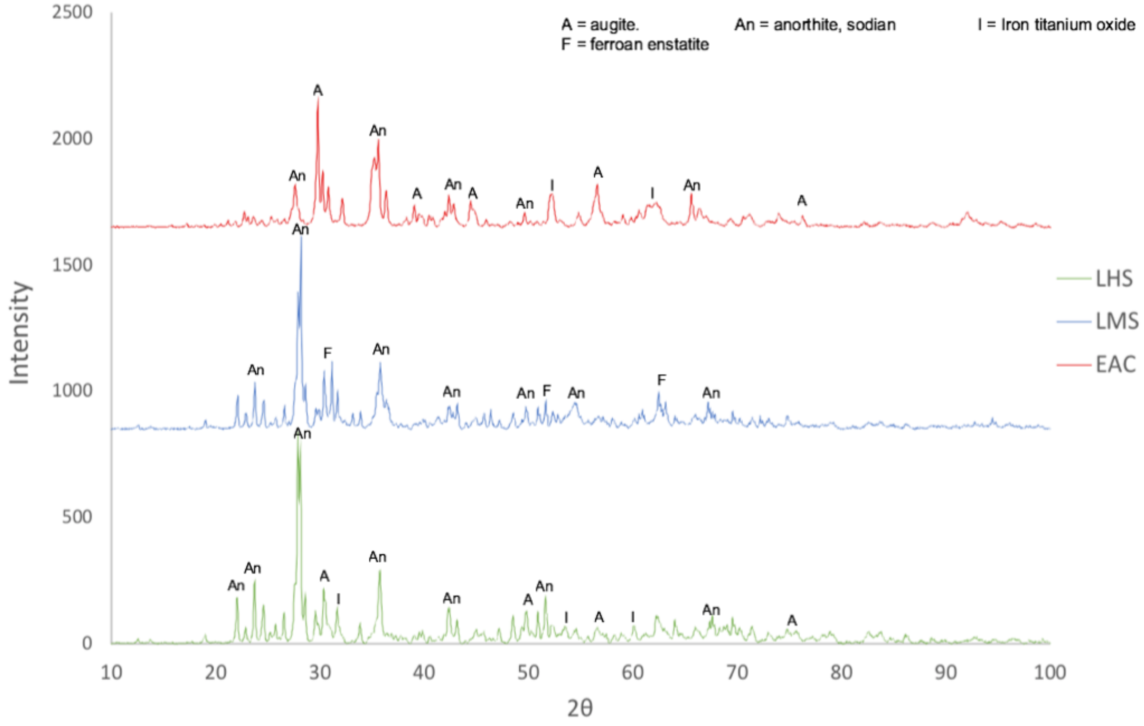

*Figure 36. XRD analysis of three regolith simulants: EAC-1A, LHS-1 and LMS-1*

#### 3.1.1.2 Particle size distribution

Lunar regolith samples from Apollo missions were found to have log-normal size distribution with mean diameters typically between 45 µm and 100 µm, although particles can be as small as 10 nm [45], [48]. The particle size distribution of the three simulants is given in figure 37a. All simulants exhibit a wide particle size range, namely 0.02 µm - 2000 µm for EAC-1A and <1 µm - 1000 µm for LHS-1 and LMS-1. The mean particle size is 10.5 µm for EAC-1A, 94 µm for LHS-1 and 63 µm for LMS-1. All simulants display a significant fraction of large grains (>1 mm), which is problematic for additive manufacturing.

Due to this, all three simulants underwent sieving through 50 or 100 µm mesh sieves to allow better sintering. Moreover, a 30g batch of EAC-1A was milled in a Retsch planetary ball mill in an argon atmosphere using tungsten carbide balls (5 and 10 mm). The powder was milled for 30 hours at a speed of 300 rpm with a ball to powder mass ratio of 10:1. The contamination was kept very low and the maximum particle size was reduced to 22 µm with mean particle size of 5 µm.

#### 3.1.1.3 Particle shape

The particle shape has great influence over the flow and packing behaviour of powders, which affects in turn the properties of the consolidated material. Lunar particles are irregular in shape and have high cohesion in comparison to terrestrial materials, due to the environmental factors of the lunar surface; as a result, lunar regolith is highly abrasive (figure 36 and figure 37 b-d) [49]. This abrasive property is difficult to simulate using Earth material, which should be considered during this feasibility study. From initial observations, LMS-1 and LHS-1 particles exhibit larger particle elongation and lower circularity than EAC-1A.

#### 3.1.1.4 Bulk density

Most AM techniques involve the loose deposition of one material layer over another one. For this reason, poured bulk density was measured instead of tapped density. Poured density is useful in this study to determine the quantity of material required for the manufacturing process. Measurements on lunar soil samples, namely Apollo 14 and Apollo 15, have revealed bulk densities that vary from a minimum 0.87 g/cm$^2$ to a maximum 1.89 g/cm$^2$**.** The reason for this variation is related to specific gravity, re-entrant intra-granular voids, particle shape, particle size distribution, and surface texture.

Poured bulk density was measured for simulants EAC-1A, LMS-1 and LHS-1 in accordance with ASTM D7481-18 (Standard Test Methods for Determining Loose and Tapped Bulk Densities of Powders using a Graduated Cylinder)[26]. 100 g of powder was poured into a 100 mL graduated cylinder and levelled; the density was calculated from the mass of the sample divided by the untapped volume occupied by the simulant. Three measurements were carried out per sample, with results derived from the mean. In comparison with lunar samples, the simulants exhibit similar poured bulk densities of 1.50 g/cm$^3$ for EAC-1A, 1.60 g/cm$^3$ for LMS-1 and 1.61 g/cm$^3$ for LHS-1.

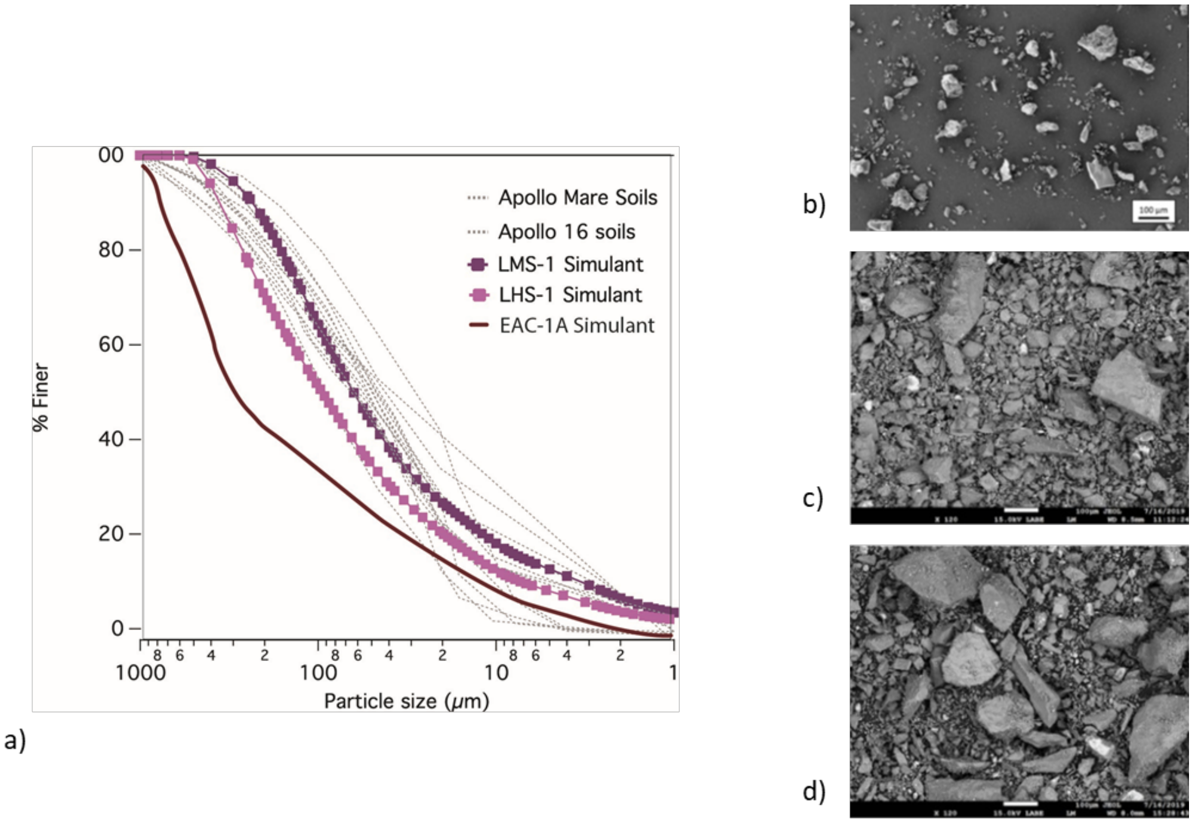

*Figure 37. Simulant powder characterization. a) Average particle size distribution for EAC-1A, LHS-1 and LMS-1 [45]. Apollo data is shown for comparison, and has been adjusted to remove the >1mm fraction. b)c)d) SEM images displaying as-received particle shape for* EAC-1A (b), LHS-1 (c) and LMS-1 (d) simulants.

### *3.1.1.5 Thermal analysis*

Regolith is a multi-constituent aggregate consisting of several mineralogical components. It is useful to understand the thermal behaviour of these components in order to estimate appropriate processing temperatures. A technique coupling Thermogravimetric Analysis (TGA) with Differential Scanning Calorimetry (DSC) was used to identify thermal transition temperatures for each sample. Using a calibrated Mettler Toledo TGA/DSC 3+ instrument, all three simulants were heated from room temperature to above 1400°C at a rate of 10K/min for EAC-1A and LHS-1 samples and a rate of 50K/min for LMS-1 sample. The tests were performed under an argon atmosphere with a constant gas flow of 70 ml/min. Additionally, a blank curve was obtained under the same conditions as each sample, in order to account for buoyancy and the effects of the instrument.

Figure 38 shows DSC curves normalized to sample temperature for EAC-1A, LMS-1 and LHS-1 simulants. All three samples exhibit transformations in the 1100 – 1350 °C region. This is consistent with the melting of basalt, ilmenite and glass [50], [51] which are present in the given simulants in varying quantity, see Table 17. The exhibited thermal behaviour may also be attributed to the melting or partial-melting of plagioclase. In lunar regolith the plagioclase is assumed to be of the high-Ca type anorthite which has a melting temperature around 1550 °C. However the presence of $Na_2O$ oxide in the bulk chemistry suggests plagioclase may have undergone partial melting, as the plagioclase solidus temperature is known to decrease with increasing sodium content [52], [53]. Thus, at sintering temperatures in the range 1250 – 1350 °C or above, some regolith melting should be expected.

From the TGA results, the following values of mass loss were recorded, in the temperature range 30 - 1350 °C. When heated above 1350 °C, mass losses of 0.97 % for LMS-1, 1.07 % for LHS-1 and 2.75 % for EAC-1A were observed. These losses can be attributed to loss of water and the release of other volatiles at higher temperatures. To emulate lunar surface conditions most effectively, simulants should be furnace dried to remove volatiles before processing.

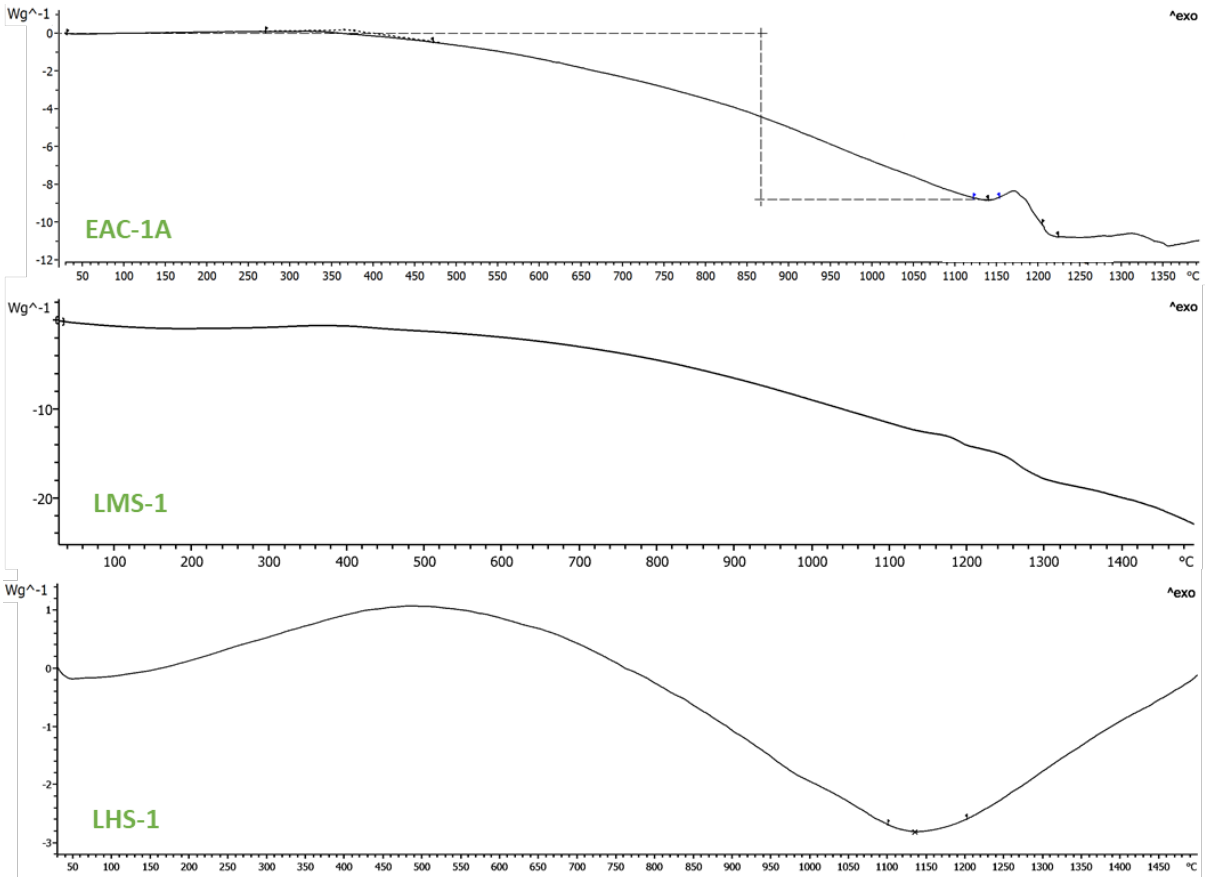

*Figure 38. DSC traces for EAC-1A (above), LMS-1 (centre) and LHS-1 (below)*

### 3.1.2 Metallic powders

For the purpose of functionally graded materials, different metals have been selected according to the elements available on the Moon. Elements such as titanium, iron or aluminium are abundant in the lunar soil. Different methods of extraction would have to be investigated to determine how to get these metals from the lunar soil.
In regard to this research, 2 different types of materials have been chosen: stainless steel 316L and $Ti_6Al_4V$.

The stainless steel powder with a particle size range from 0 to 30 μm was provided by Admatec (Alkmaar, The Netherlands) and the $Ti_6Al_4V$ with a particle size range of 15 to 45 μm was provided by

AP&C advanced powder & coatings. These different metal powders have been consolidated using a Spark Plasma Sintering device.

## 3.2 Consolidation experiments

### 3.2.1 Digital Light Processing

Digital Light Processing was performed by Admatec (Alkmaar, The Netherlands) using EAC-1A simulant powder. Some first trials were made with the as-received lunar regolith powder. The as-received powder was mixed with a resin to form a slurry and perform a Depth-of-Cure experiments. The resulting print was unsuccessful: subsequent layer did not adhere together.
The powder was then sieved through a 30-μm sieve (Figure 39) to improve the slurry properties.

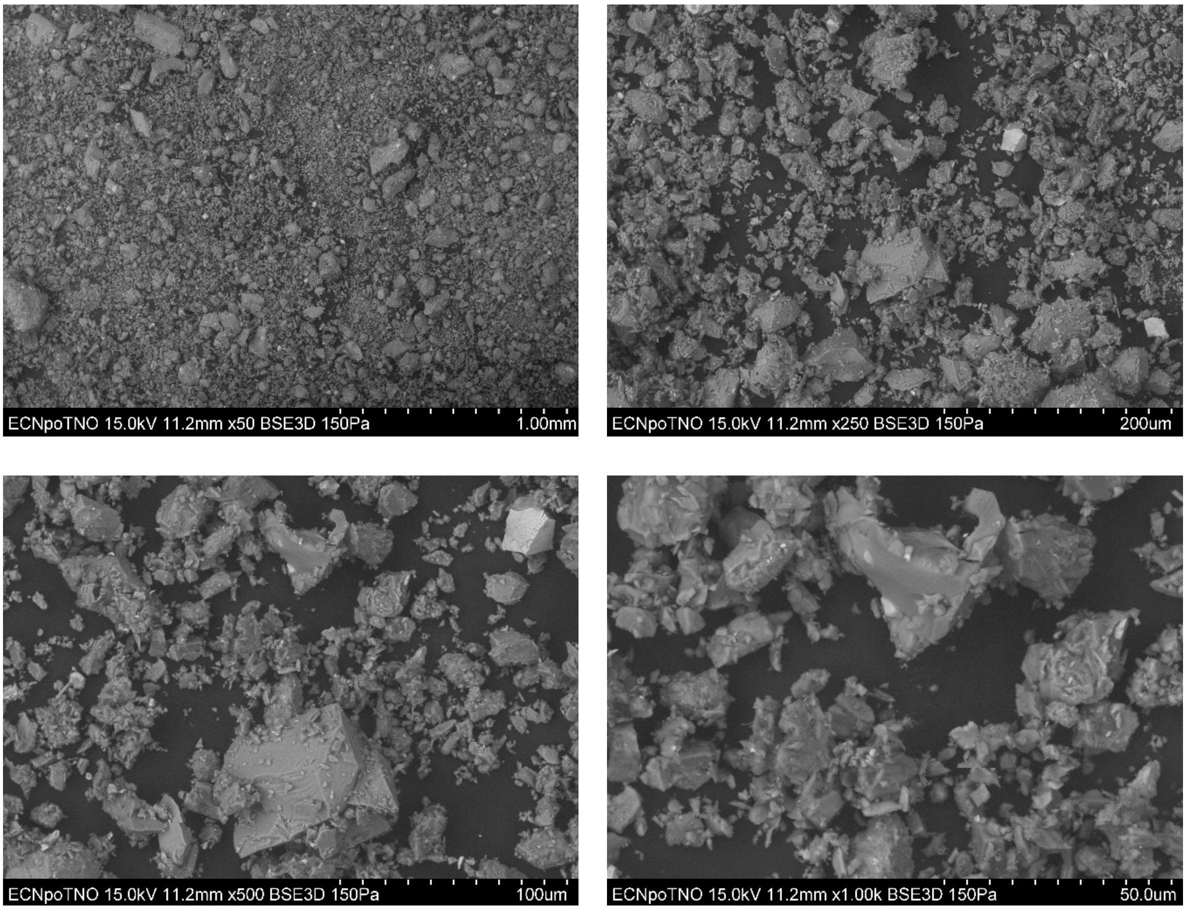

*Figure 39. SEM images of the morphology of the sieved EAC-1A material, material smaller than 30 μm*

The sieved powder was used for the final slurry composed of:

- Solid content of sieved EAC-1A is 41 %
- Resin, for making the printed structure
- Photo initiator (PI), to make the polymerization reaction of the resin start with UV-light
- Addition of chemical content to make water debinding possible
- Chemical additions to make the interaction between the resin and sieved EAC-1A optimal

The slurry was then printed to shape 4 rectangular samples of 5 mm high, 5 mm thick, and with a length of about 100 mm. They were printed with a layer thickness of 50 μm and a Depth of Cure of 100 μm to allow better binding of adjacent layers. The layer thickness is chosen to be higher than the maximum particle size and the Depth of Cure depends on the energy used, the properties of the powder and on the solid content. The energy is calculated as the power of the light engine times the time. Moreover, it has been found out in the past that only the energy matters (E=P*t) and that an optimization of both parameters (power and time) are not required: only the value of their product is relevant. The Depth of Cure is then equal to 2 layers, which is a rather optimal number for a printing process in general.

Water debinding was first performed for 1 day followed by a debinding in a furnace. The debinding in a furnace involved slow heating in air with stops at 150, 300, 400 and 600 °C to obtain the optimal removal of all the resin and to be able to lower as much as possible the remaining carbon amount.

The bars have been sintered in a furnace in an air atmosphere. The first sintering temperature was set to 1050 °C and kept for 1 hour, with a slow heating rate of 100 °C/h. An additional sintering run at 1075 °C was undergone to improve sintering of the bars.

### 3.2.2 Spark Plasma Sintering

Spark Plasma Sintering has been studied as a technique to consolidate the lunar regolith simulants (as post DLP shaping and bending step), the metal powders and eventually the functionally graded materials. An optimization of the parameters for SPS was required for the different materials.

All the powders were compacted in a Spark Plasma Sintering machine (SPS, FCT Group, Germany, Figure 40) under vacuum in a graphite die and graphite punches. A 0.2 mm thick graphite foil was used to avoid adhesion and reaction between the powders and the graphite mould. Besides this foil, boron nitride spray was used to reduce carbon diffusion into the sample. The samples were sintered at different temperatures and different pressures. The detailed overview is given below for the different powders.

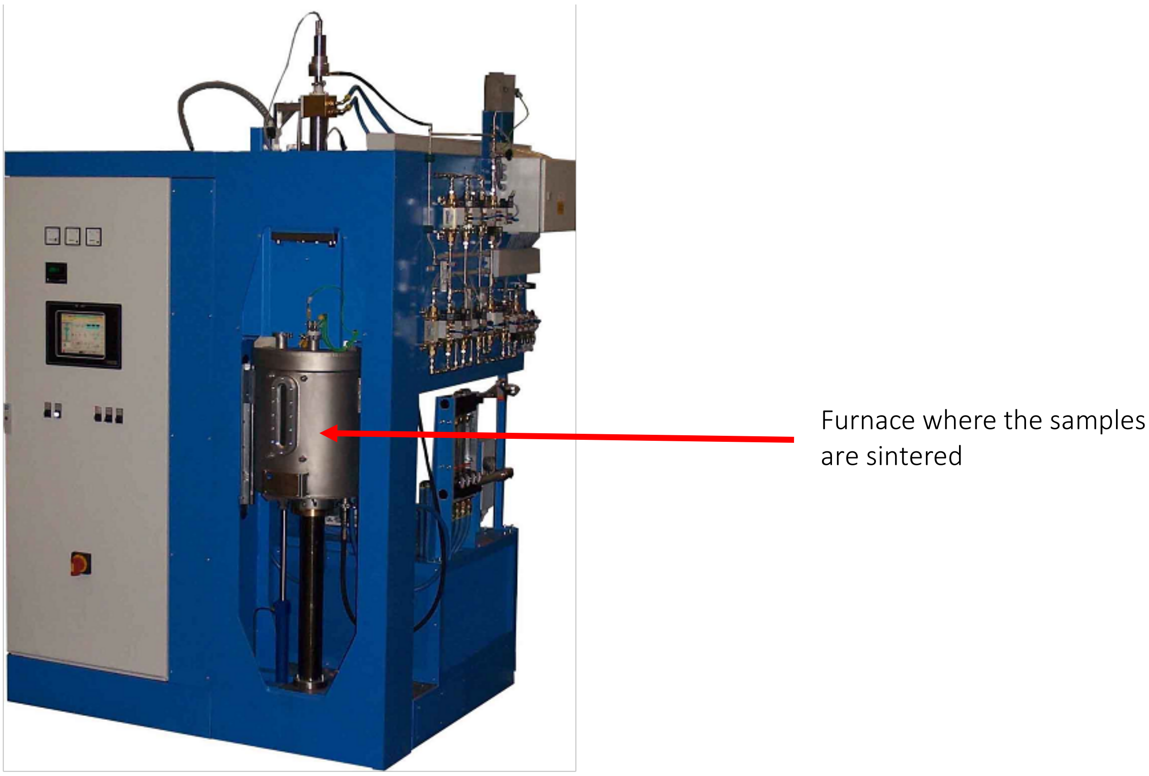

*Figure 40. Spark Plasma Sintering device (used in this study and available at MSE, TU Delft)*

### 3.2.2.1 *Lunar regolith simulant*

Zhang and al. [13] have published a paper on consolidation with this technique and with this type of material. They however used a different lunar regolith simulant and a different SPS device. However, the parameters used for this study were mostly based on their research.

For SPS experiments (Figure 41 and table 18), 3 g of the powder was poured into a 20 mm graphite mould and pre-pressed to 10 kN before being set up into the SPS machine. The parameters used for the different experiments are given in the table 18 below.

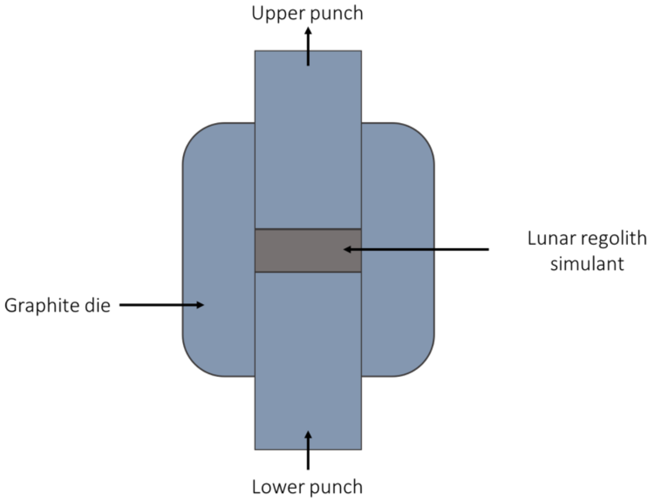

*Figure 41. Spark Plasma Sintering set-up*

*Table 18. SPS parameters for lunar regolith simulants samples*

| Samples | Lunar regolith simulant | Sintering temperature (°C) | Pressure (MPa) | Holding time (min) | Maximum particle size (µm) |
|---|---|---|---|---|---|
| 1 | LHS-1 | 900 | 80 | 10 | 200 |
| 2 | LHS-1 | 975 | | 20 | 100 |
| 3 | LHS-1 | 975 | | | 50 |
| 4 | LHS-1 | 1025 | | | 50 |
| 5 | LHS-1 | 1050 | | | 50 |
| 6 | LHS-1 | 1075 | | | 50 |
| 7 | LMS-1 | 1050 | | | 50 |
| 8 | EAC-1A | 1050 | | | 22 |
| 9 | EAC-1A | 1050 | | | 50 |
| 10 | EAC-1A | 1050 | | | 100 |

The maximum temperature used was 1075 °C to avoid melting of the powder and squeezing out of the mould. Indeed, Zhang and al. [13] observed melting of the powder above 1050 °C, but they used a pressure of 100 MPa. Moreover, according to the DSC measurements (figure 38) partial melting is observed above 1100 °C. Hence 1075 °C was the maximum sintering temperature used for the lunar regolith simulants.

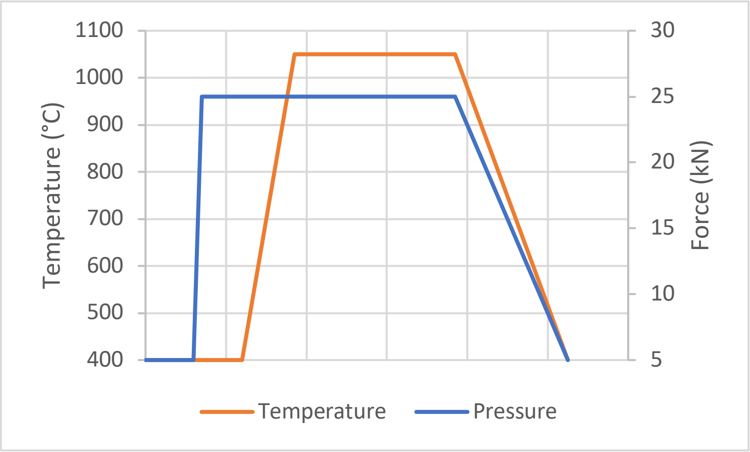

*Figure 42. Profile of force and temperature for SPS*

A typical temperature and pressure profile are given in Figure 42, with the sintering temperature of 1050 °C.

The original powders have a very wide range of particle sizes (figure 37) and thus were sieved through 50 or 100 μm mesh sieves to allow better sintering. The contamination of the powder during the milling was very low as shown on Figure 43, less than 0.1 at.% of tungsten was detected. The maximum particle size was thus reduced to 22 μm with mean particle size of 5 μm.

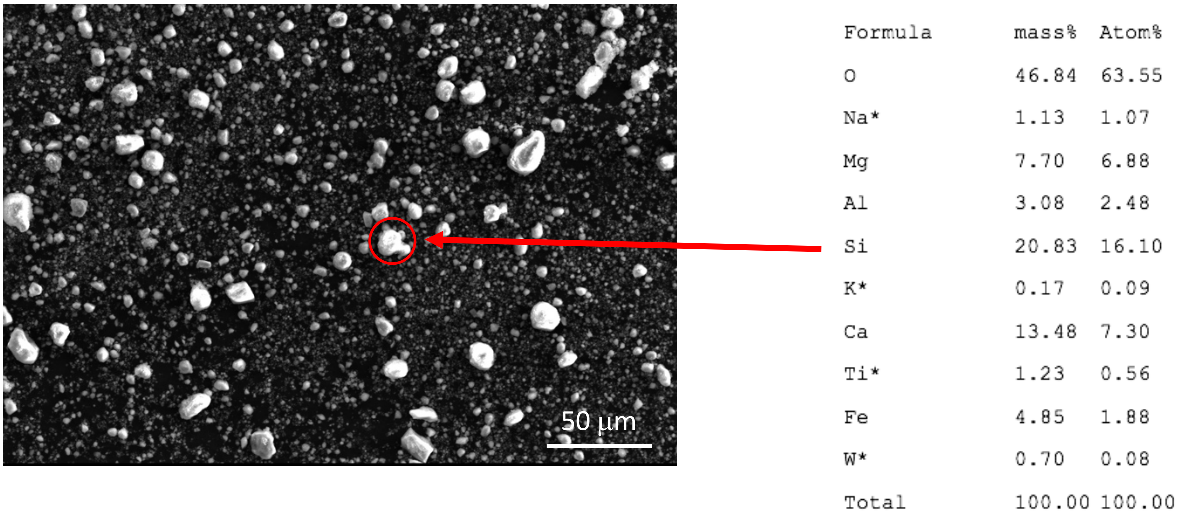

```
Formula       mass%  Atom%
O             46.84  63.55
Na*           1.13   1.07
Mg            7.70   6.88
Al            3.08   2.48
Si            20.83  16.10
K*            0.17   0.09
Ca            13.48  7.30
Ti*           1.23   0.56
Fe            4.85   1.88
W*            0.70   0.08
Total         100.00 100.00
```

*Figure 43. EDS for crushed EAC-1A powder*

### 3.2.2.2 *Metals*

Stainless steel and $Ti_6Al_4V$ powders have been studied separately to determine the optimal parameters before doing trials of functionally graded materials with the lunar regolith simulants.

#### Stainless Steel 316

Sintering steels with spark plasma sintering is not new. However, stainless steel is not as common as other steels. The parameters chosen to sinter our powder were based on the researches of Kale and al. [54] and Marnier and al. [55] and are given in the table below.

*Table 19. SPS parameters for 316 samples*

| Samples | Sintering temperature (°C) | Pressure (MPa) | Holding time (min) | Maximum particle size (µm) |
|---|---|---|---|---|
| 1 | 1050 | 50 | 10 | 30 |
| 2 | 1050 | 50 | 20 | |
| 3 | 1100 | 50 | | |

#### Ti$_6$Al$_4$V

The parameters for the sintering of Ti$_6$Al$_4$V had to be determined before performing functionally graded materials. Two sets of parameters given in Table 20 were chosen based on the researches of Kgoete and al. [56] and Falodun and al. [57].

*Table 20. SPS parameters for Ti$_6$Al$_4$V samples*

| Samples | Sintering temperature (°C) | Pressure (MPa) | Holding time (min) | Maximum particle size (µm) |
|---|---|---|---|---|
| 1 | 1000 | 50 | 10 | 45 |
| 2 | 1050 | 50 | 10 | |

### *3.2.2.3 Functionally Graded Materials*

SPS has been firstly performed for the different materials alone to be able to determine some optimal parameters (pressure, temperature, holding time, maximum particle size) for each material. The second stage of this research was to combine a layer of lunar regolith simulant with a layer of a metal (figure 44 and 45). Two main type of experiments were considered: a one-step sintering experiment where both powders are sintered under the same conditions, or a two-step experiment where the powder are sintered one after each other under different parameters.

The optimal parameters for the lunar regolith was chosen as a sintering temperature of 1050 °C, a pressure of 80 MPa, a holding time of 20 min. Moreover, the crushed powder EAC-1A was selected to obtain better sintering. The choice of these parameters is based on the microstructural results and densification of the lunar regolith samples.

A two-step experiment was chosen to sinter a FGM made of EAC-1A and Ti$_6$Al$_4$V. EAC-1A was first sintered under the optimal parameters described above and Ti$_6$Al$_4$V was then sintered under a temperature of 1050 °C, a pressure of 50 MPa and holds for 10 min at these conditions.

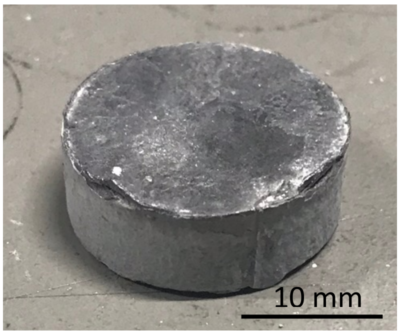

*Figure 44. FGM: Lunar Regolith and $Ti_6Al_4V$*

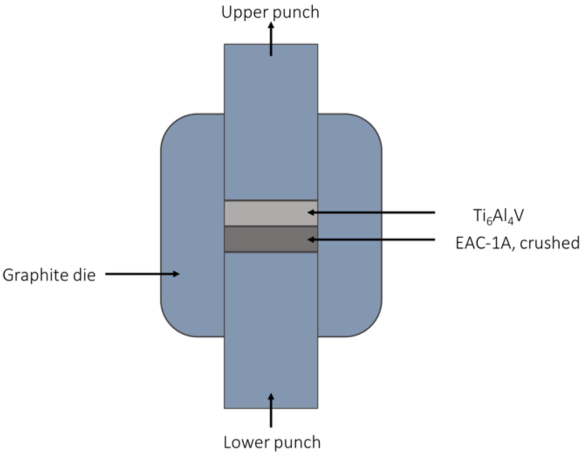

*Figure 45. Spark Plasma Sintering set-up for FGM EAC-1A/$Ti_6Al_4V$*

The optimal sintering parameters for stainless steel 316 are 1100 °C, 50 MPa and a holding time of 20 min. These parameters were close to the ones used to sinter crushed EAC-1A. Three different experiments were then done with these parameters. A two-step experiment was performed with the sintering of the stainless steel layer as a first layer followed by the sintering of the lunar regolith simulant layer (figure 46-a). Two one-step experiments were also performed. Two experiments of sintering both layers at the same time was undergone: one experiment using the optimal conditions for stainless steel sintering (figure 46-c) and a second experiment was performed under the optimal conditions for the lunar regolith simulant (figure 46-b).

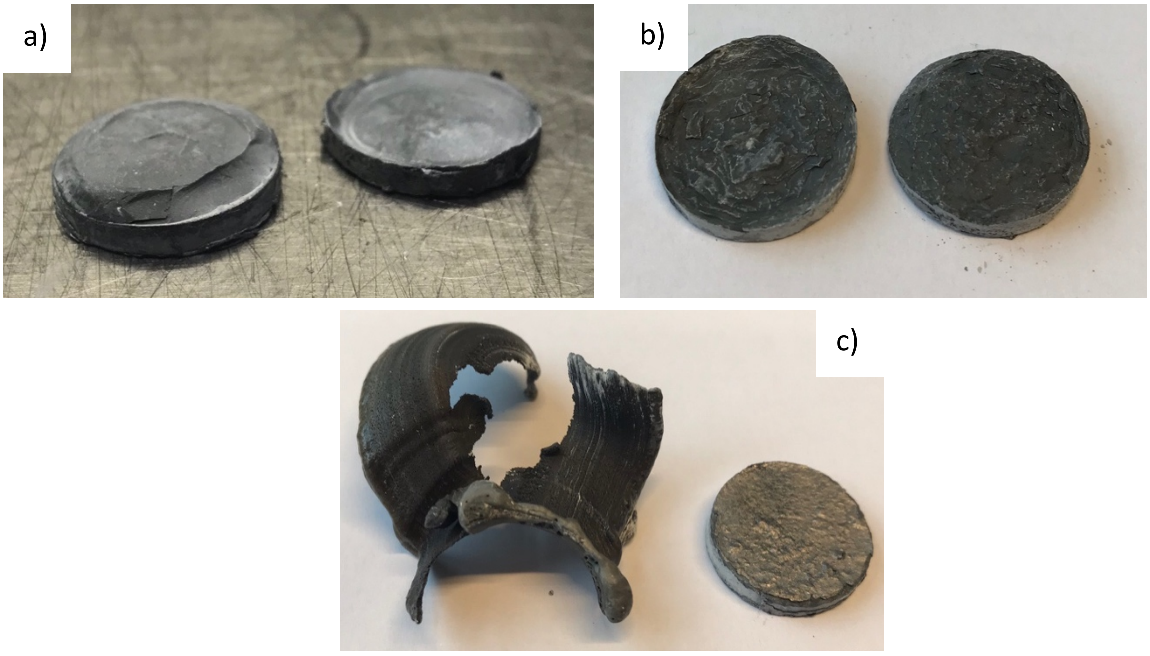

*Figure 46. EAC-1A/316L: a) sintered in 2 steps, b) sintered in 1 step at 1050 °C/80 MPa/20min, c) sintered in 1 step at 1100 °C/50 MPa/20 min*

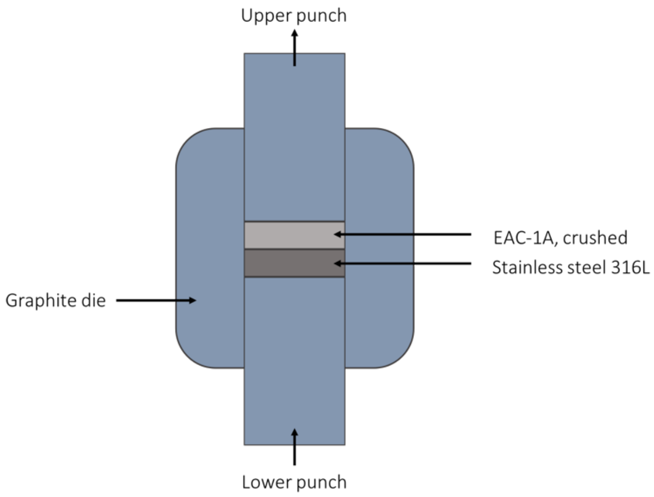

*Figure 47. Spark Plasma Sintering set-up for FGM EAC-1A/316*

### 3.2.3 Laser melting experiments

The lunar regolith simulant LMS-1 was used to Laser Scan lines. The laser specifications are: Yb:YAG continuous disk laser with a wavelength of 1030 nm. The power was in the range of 160 - 8000 W and the scanning speed was up to 200 mm per second. The spot size of 0.2 mm at focus was used. The powder was sieved through a 100 μm-sieve and deposited on a ceramic plate. In literature, some parameters were found to be optimized for selective laser melting or other laser additive manufacturing techniques of lunar regolith simulant. They had one common point, which is that a very low surface energy density, often less than 5 J/mm² should be used [58], [59], [60], [61]. The parameters had to be adapted to our own laser at TU Delft. The parameters used is this study are shown below in Table 21 and were chosen to have the energy density as low as possible.

The base substrate was a ceramic plate, which commonly used for high temperature ovens, instead of the common steel substrate used with this laser. The choice for ceramic plate is based on findings by Sitta and Lavagna [59], who found a poor wettability of the lunar regolith simulant on a steel substrate. Other metallic substrates were used for their research, but they achieved better results when using a refractory clay as a substrate.

*Table 21. Parameters for laser scanned lines*

| Samples | Lunar regolith simulant | Maximum particle size (μm) | Laser Power (W) | Beam spot size (mm) | Scan speed (mm/s) |
|---|---|---|---|---|---|
| 1 | LMS-1 | 100 | 160 | 0.2 | 100 |
| 2 | | | | 0.4 | |
| 3 | | | | 0.6 | |

In this work, some trials on a steel plate have been performed to study the influence of substrate and determine the potential feasibility of using the lunar regolith as a coating on metallic substrate. The same parameters were kept for these trials as for the ceramic plate. However, additional laser lines have been also conducted, which included an overlapping of 50 % to study the influence of remelting.

## 3.3 Characterisation techniques

### 3.3.1 Archimedes density measurement

A dry weighing technique has been used to determine the density of the SPSed samples. Prior to the measurement of the density, all surfaces of the samples were ground (SiC 80) to remove the layer of graphite foil present after the SPS experiments. They were then cleaned using iso-propanol in an ultrasonic bath for 10 min.

The density measurement is based on Archimedes principle (figure 48). The samples are first weight dry and then weight immerged in distilled water using the balance Mettler PM480 DeltaRange®. The density is then determined from the difference between the two values. This technique only gives the apparent density: only open pores are taken into account and not the closed pores where the distilled water cannot penetrate.

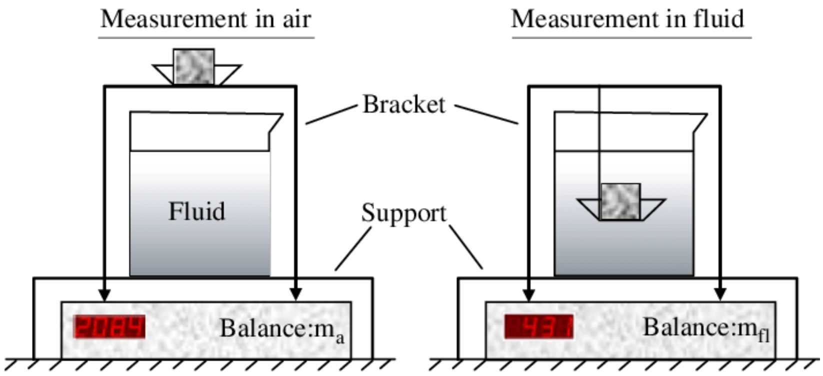

*Figure 48. Archimedes method [77]*

The density is calculated as follows:

$$\rho = \rho_{water} * \frac{m_a}{m_a - m_{fl}} \tag{9}$$

The relative density (%) of the samples is determined by dividing the measured density by the theoretical density of the lunar regolith simulant. The approximations of the density of fully dense specimens made of the lunar soil simulants can be calculated based on their compositions and on the density of each of these oxides. The calculated theoretical densities are then 3.36 g/cm$^3$ for EAC-1A, 3.27 g/cm$^3$ for LHS-1 and 3.34 g/cm$^3$ for LMS-1. The theoretical densities could also be determined with XRD as shown in appendix 1.

### 3.3.2 Microstructural investigation

Spark Plasma Sintered samples were discs of diameter of 20 mm and thickness of 4 mm. The specimens were first cut into 2 half-discs to be able to analyse the cross-sections. Different techniques have been tried to cut the samples: regular saw (manual cutting), cutting wheel or Electrical Discharge Machining. The samples were too strong to be cut with regular cut-off wheels and were not conductive enough to be cut with Electrical Discharge Machining. They had to be water-jet cut to avoid any damages of the samples or of any saw that might be used. The water-jet cutting was performed by WestEnd Machinefabriek in Lisse. The specimens were then embedded into a conductive resin. Following, the embedded samples were ground (SiC 80, 180, 320, 800, 1200 and 2000) and polished (MD Mol 3 μm and MD Nap 1 μm). The samples were observed using an optical microscope Olympus BX60M Trinocular Inspection Microscope and using a Scanning Electron Microscope.

The porosity level of the different samples has been measured with the optical images along the thickness of the samples. Moreover, the thickness of the most sintered layer of the samples has been measured with the optical microscope taking the average of 10 measurements along the length of the samples. The porosity of the sintered layer of the samples was measured: 4 locations were analyzed per sample and 5 measurements were done on each location to determine the average over these measurements.

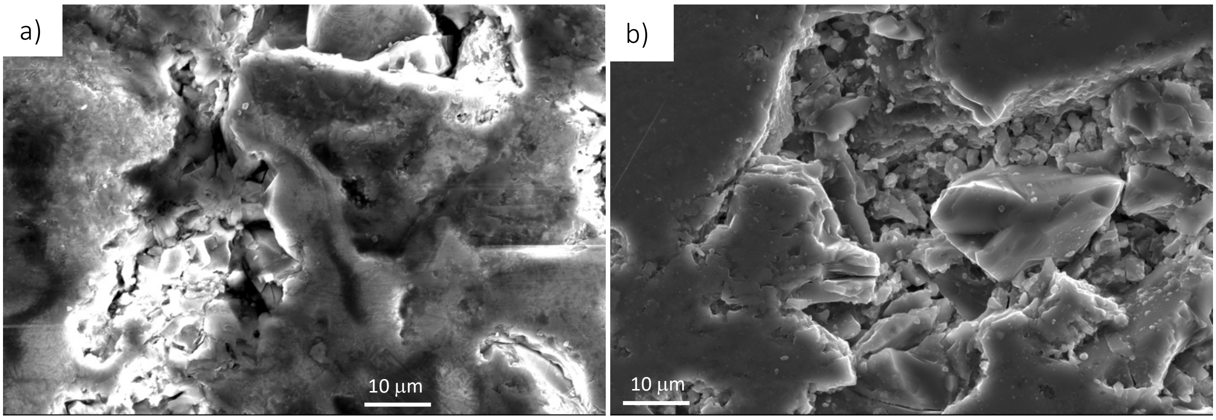

*Figure 49. SEM images of LHS-1: a) Non-coated sample, b) coated sample*

The samples were poorly conductive and two different ways have been used to be able to observe the samples under a SEM. The samples were either observed in low vacuum to be able to do EDS analysis or were coated with a thin layer of carbon (figure 49). SEM was used to perform EDS analysis and determine the oxides or phases present in the materials; and observe whether necking occurred during the consolidating experiments.

### 3.3.3 XRD Analysis

XRD analysis was performed to determine the compositions of the sintered samples and the laser scanned lines. It was performed to determine whether the sintering temperature and the particle size distribution have an influence on the oxide composition and phase formation. The analysis of the sintered samples was performed with a Bruker D8 Advance diffractometer using a Cu Kα radiation. The step size used was 0.033° 2θ with 45 kV and 40 mA current in a 2θ range of 10° - 100°. The samples were polished with SiC 180 on the most sintered side to remove the remaining graphite foil and to enable XRD analysis.

The laser scanned lines were analyzed to determine whether the material turns amorphous or remains crystalline after being printing with laser additive manufacturing technique. This analysis was performed with Bruker D8 Discover diffractometer, Incoatec Microfocus Source (IμS) using a Cu Kα radiation. The step size used was 0.033° 2θ with 50 kV and 1000 μA current. The substrate was also analyzed with the same conditions to compare its XRD pattern with the one of the scanned lines.

### 3.3.4 Hardness Testing

The microhardness measurements were carried out using an automated Vickers hardness machine, Dura Scan (Struers) and were only carried out for the SPS samples. A load of 0.3 kgf was used to measure the hardness of the lunar regolith sintered samples because the first measurements revealed that the material was very brittle and cracked under higher load (figure 50). The hardness measurements were carried out along the most sintered layer of the different samples: 5 to 10 measurements were done to obtain an average of the hardness for each sample.

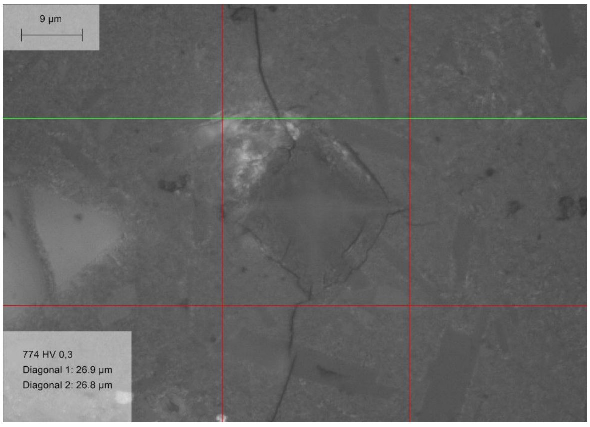

*Figure 50. Cracks under force during microhardness testing*

For the metallic sintered samples, a load of 0.5 kgf was used to measure their hardness. The hardness was measured on different locations of each sample and the average was calculated.

The fracture toughness of the most sintered sample was determined using the Vickers indentation crack length method. The Young modulus of the material was determined using the load-displacement curve obtained during the indentation.

The model used for this study is the one developed by Anstis [62] whose equation is given below:

$$K_C = 0.0016.\left(\frac{E}{HV}\right)^{0.5}\left(\frac{P}{c^{1.5}}\right) \tag{10}$$

This equation gives the relationship between the fracture toughness $K_C$ (in MPa.m$^{1/2}$) and the Young modulus E (in GPa), the Vickers hardness HV (in GPa), the indentation load P (in N) and the crack length from the centre of the indentation to the crack tip (in m).

## 3.4 Modelling of DLP

The sintering stage can be modelled in order to be understand and optimize the sintering of new or a combination of existing materials. In this study, a continuum mechanics approach and a model at the macroscopic level was considered to evaluate shrinkage of the samples and temperature evolution within the sample [63].

The sample before sintering is a porous medium and its behaviour can be studied by continuum mechanics. The solid is composed of a solid part (the particles) and porosities. The porosities are considered to be homogeneously distributed and the solid phase has an isotropic and non-linear viscous behaviour. During the sintering, it is expected that the porosity will decrease, and the density will increase, while the sample will shrink during sintering. The relative density ($\rho$) is then related with the porosity ($\theta$) level as follows:

$$\rho = 1 - \theta \tag{11}$$

During sintering, the sample shrinks and its volume decreases, but the mass remains the same. The mass conservation principle can be applied as follows:

$$\frac{\dot{\rho}}{\rho} = tr(\underline{\dot{\epsilon}}) \tag{12}$$

with $\underline{\dot{\epsilon}}$ the strain rate of solid phase.

Moreover, the momentum conservation law is applicable to continuum solid and the equation is as follow considering a quasi-static transformation:

$$\Delta\underline{\sigma} + f = 0 \tag{13}$$

with $\underline{\sigma}$ the Cauchy stress tensor and f the external force applied.

The sintering process implies the heating of the powder and the mechanical phenomenon is coupled with a thermal phenomenon. The conservation energy equation is then:

$$\rho C_{eff}\dot{T} - \nabla\left(K_{eff}\nabla T\right) = \beta(\underline{\sigma}:\underline{\dot{\varepsilon_{vp}}} - \sigma_s \dot{e}) \tag{14}$$

with $C_{eff}$ is the heat capacity, $K_{eff}$ is the thermal conductivity, β is the viscoplastic work dissipated as heat (0 < β < 1), $\underline{\dot{\varepsilon_{vp}}}$ is the viscoplastic strain rate and finally $\dot{e}$ is the volumic strain rate.

In free sintering, stress and viscoplastic strain are negligible, hence the right side of the equation above equals to 0. Both the heat capacity and the thermal conductivity depends on the temperature and the porosity level.

This continuum mechanics approach is summarized in the graph below in Figure 51.

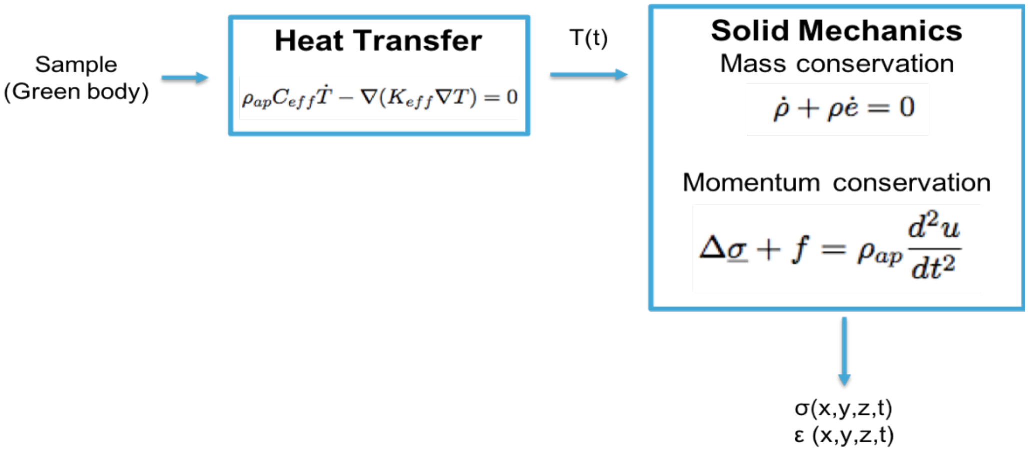

*Figure 51. Diagram of simulation steps*

A viscoplastic constitutive model is applied to determine the deformation during sintering. Indeed, the deformation during sintering is controlled by diffusion and is comparable to creep induced deformation. Moreover, thermal expansion is also relevant in the case of sintering and must be added to the viscoplastic deformation. The deformation has then three main components: an elastic deformation, a thermal deformation and a viscoplastic deformation.

The strain rate is then:

$$\dot{\epsilon} = \dot{\epsilon_e} + \dot{\epsilon_{th}} + \dot{\epsilon_{vp}} \tag{15}$$

and the viscoplastic strain rate is divided as follows:

$$\dot{\epsilon}_{vp} = \dot{\epsilon}_s + \dot{\epsilon}_c \tag{16}$$

The elastic strain $\epsilon_e$ is determined by Hooke’s law and the thermal strain $\epsilon_{th}$ depends on temperature and thermal expansion coefficient.

The viscoplastic strain is expressed as follows:

$$\dot{\epsilon}_{vp} = \frac{\underline{\sigma\prime}}{2G_p} + \frac{\sigma_m - \sigma_s}{3K_p}\underline{1} \tag{17}$$

with $\underline{\sigma'}$ the deviatoric stress, $\sigma_m = \frac{tr(\sigma)}{3}$ the hydrostatic stress and $\sigma_s$ the sintering stress.

The parameters for the viscoplastic constitutive law can be determined by different models. The model chosen has been developed by Olevsky and Skorohod (SOVS model). It is a phenomenological model commonly used for the modelling of ceramic sintering. The parameters are then:

$$G_p = (1 - \theta)^2 \eta \tag{18}$$

$$K_p = \frac{4(1-\theta)^3 \eta}{3\theta} \tag{19}$$

$$\sigma_s = \frac{3\gamma_{sv}(1-\theta)^2}{r_0} \tag{20}$$

with $\eta$ the viscosity and $\gamma_{sv}$ the surface energy.

This model has been implemented to Comsol Multiphysics®. The model consists of a heat transfer module and a solid mechanics module using the creep subroutine to implement the SOVS model.

# 4 Results & Discussion

## 4.1 Digital Light Processing

Digital Light Processing is a multi-step additive manufacturing involving printing of the slurry, debinding of the samples and sintering of the particles. The parameters for all these stages depend on the material used.

First of all, the choice of the resin and the final composition of the slurry is key in the process. Indeed, the ceramic suspensions are of high importance to carry out a successful process. The particles of lunar regolith simulant must be homogeneously and effectively dispersed into the resin and must retained stable for a certain time (time of printing and waiting time before debinding stage). The viscosity of the resin must be high enough to avoid rapid segregation of the ceramic particles because segregation of the particles would lead to inhomogeneity in the printed parts. However, the viscosity of the resin should not be too high to be able to print the specimens. The flow of the resin should be optimized by balancing the need of printing and the need to avoid particles segregation. Different DLP tests have been performed to optimize the slurry composition and, chose a special photocurable resin and a solid content of 41 %. The choice of 41 % solid content is a balance between a high volume fraction of particles that enables higher densification and less shrinkage, and a low volume fraction of particles, which leads to low viscosity of the slurry and avoids segregation of the particles [64]. The lunar regolith simulant is thus able to be mixed with a specific resin and can be printed. It should be noted that the powder was sieved to obtain a maximum particle size of 30 μm and an optimal particle size is commonly around 1 to 5 μm for ceramic powder. The use of milled powder could lead to a change of the resin used and of the solid content.

Four bars have been printed with a width and a height of 5 mm. As can be seen on Figure 52, the printing of one of the bars had to be stopped: this bar did not completely stick to the base foil. This can be due to some printing failure such as dropping or sticking or due to an improper initial layer adhering time or an improper building plate preparation [65].

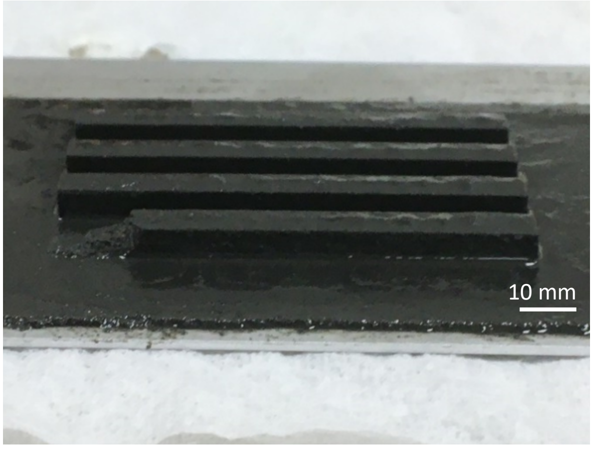

*Figure 52. DLP printed samples*

The debinding stage has been performed in a furnace. The samples were heated to a maximum of 600 °C to optimise the removal of all the resin and have as little carbon as possible in the samples. Stops at 150 °C, 300 °C and 400 °C were done during the heating to determine whether the resin was removed, or higher heating was necessary.

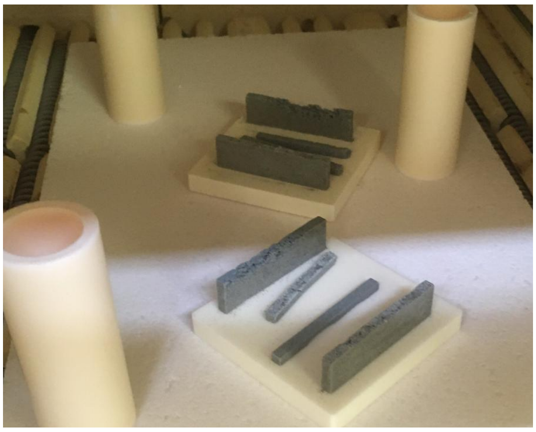

*Figure 53. DLP samples after thermal debinding treatment*

The debinding was successful and the bars remained in its shape after being heated. Moreover, the colour of the samples was grey after debinding as can be seen on figure 53, which is the same colour as the original powder before being mixed with the resin. It indicates that no significant change of the composition of the powder should have occurred.

The bars have been sintered in a furnace in an air atmosphere. The bars were first sintered at 1050 °C and hold at this sintering temperature for one hour. The heating rate was 100 °C/h. The samples were slightly sintered after this stage and very fragile. They were then sintered at 1075°C with the same holding time and same heating rate. The samples still showed poor sintering characteristics and broke into parts when touched (figure 54). Thus the bars have not been well sintered, and the sintering temperature seemed to be too low.

*Figure 54. DLP sintered samples*

First observation was a change of colour of the bars after sintering. They changed their colour to a red brick. The similar colour change was also noticed by Liu and al. [11]. It was found to be associated with the transformation of $Fe^{2+}$ to $Fe^{3+}$ via oxidation reactions.

Some sintered parts were embedded into conductive resin. Trials to grind the samples have been done with SiC 800 and SiC 1200 but the samples were too fragile: the particles did not stick together. The samples were coated with carbon to be observed under SEM.

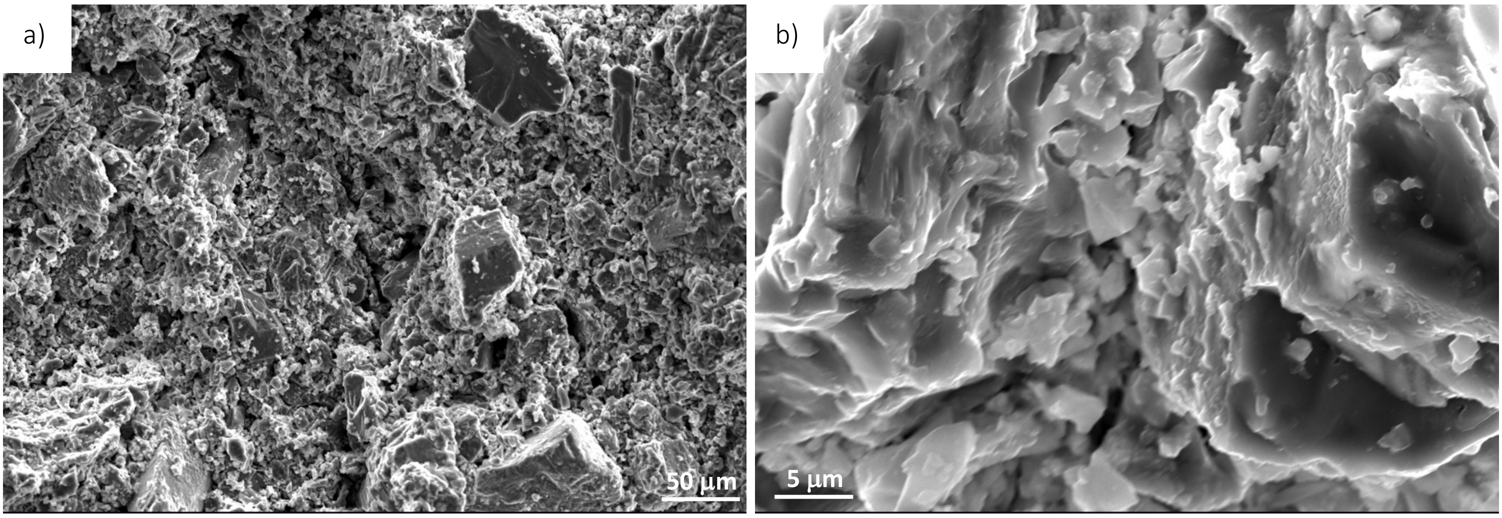

*Figure 55. SEM images of the DLP sintered samples of EAC-1A: a) low magnification (x270) and b) high magnification (x2700)*

As expected with the brittleness of the samples, the microstructure of the samples showed a very poor sintering between the particles (see Figure 55). As can be seen, the bigger particles are surrounded by smaller particles, which is beneficial for a sintering purpose as the smaller particles can close the voids between coarser particles, thus resulting in better packing and densification. However, as shown on the second image of Figure 55, only few particles have coalesced and formed necks between them. Thus sintering step requires further optimization to be successful. Some observations such as the presence of some necking is an indication that this material could (in principle) be sintered with Digital Light Processing with an optimized process.

## 4.2 Spark Plasma sintering

### 4.2.1 Spark Plasma Sintering of lunar regolith simulant

Spark Plasma Sintering was then used as sintering optimization step on the 3 different lunar regolith simulants. This technique is useful since it combines temperature and pressure to achieve high densification at lower temperature compared to other sintering techniques. The parameters to sinter this special material are unknown and an optimization was required as a first step. Only two articles are found in literature about this technique applied to this material [13] [18]. Two main parameters were considered as crucial for the sintering: the sintering temperature and the particle size distribution. Some experiments were carried out to determine the influence of these 2 main parameters.

#### *4.2.1.1 Influence of temperature*

Spark Plasma Sintering process is a successful technique to densify the lunar regolith simulants. Some first trials were made at low sintering temperature regarding the results of Phuah and al. [18] and Zhang and al. [13]. LHS-1 has been sintered at 900 °C and 975 °C. However, these sintering temperatures only gave porous samples (Figure 56) and the analysis of the influence of temperature has been further studied for the samples sintered at 1025 °C, 1050 °C and 1075 °C.

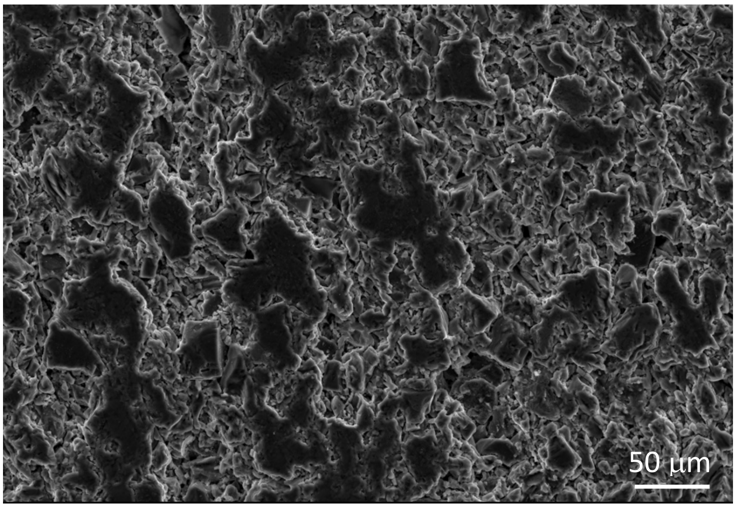

*Figure 56. LHS-1 sintered at 975 °C under 80 MPa*

Increasing the sintering temperature increases the density of the specimens and decreases the average porosity (Figure 59). The maximum density achieved was 2.704 ± 0.025 g/cm$^3$ with a sintering temperature of 1075 °C. However, during the sintering at this temperature, the travel distance of the piston was high, and it was decided not to continue sintering at this temperature: no liquid was squeezed out from the mould, but local liquid sintering could have played a role in this higher travel piston distance. The density achieved for these samples are in good accordance with the density achieved by Zhang et al. [13]: they achieved higher density, but they used a pressure of 100 MPa. However, it should be noted that not all the LHS samples were fully densified along their height (Figure 57). The samples are almost fully dense on their outer part, but in some samples the inner part is more porous. A higher pressure could then be helpful to promote a whole densification since a higher holding time did not show better results for Zhang et al. [13]. The denser structure on the edge of the sample can even be seen by naked eyes since a difference of colour exists between the densified layer and the more porous sample (see Figure 58). The denser layer exhibits a dark colour, while the remaining part of the sample and the initial powder are light grey. This phenomenon was not observed for EAC-1A and LMS-1 samples, which showed homogeneous densification (to be addressed in more detail in section 4.2.1.3).

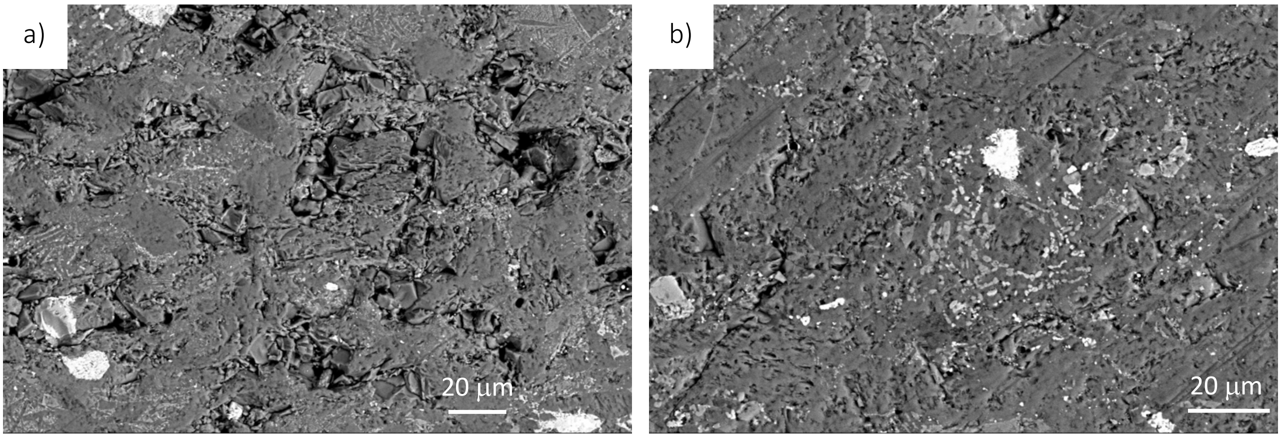

*Figure 57. SPS sintered LHS-1 sample at 1050 °C: a) middle, b) surface*

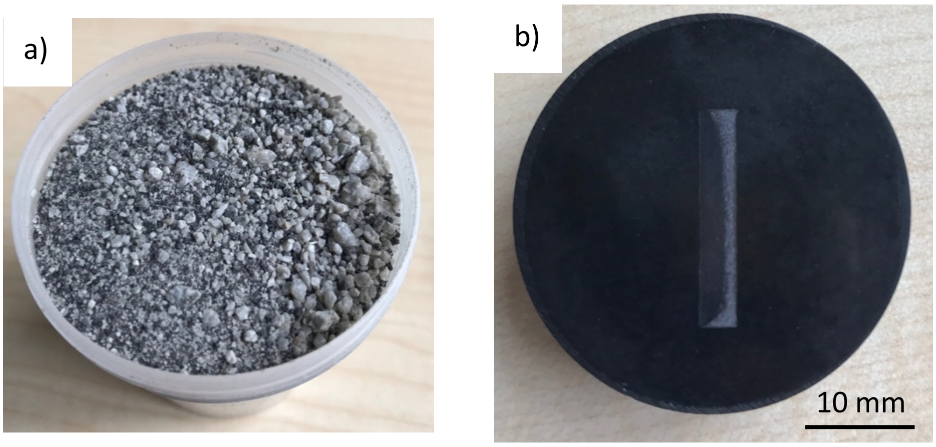

*Figure 58. a) LHS-1 powder, b) SPS sintered sample LHS-1 at 1075 °C*

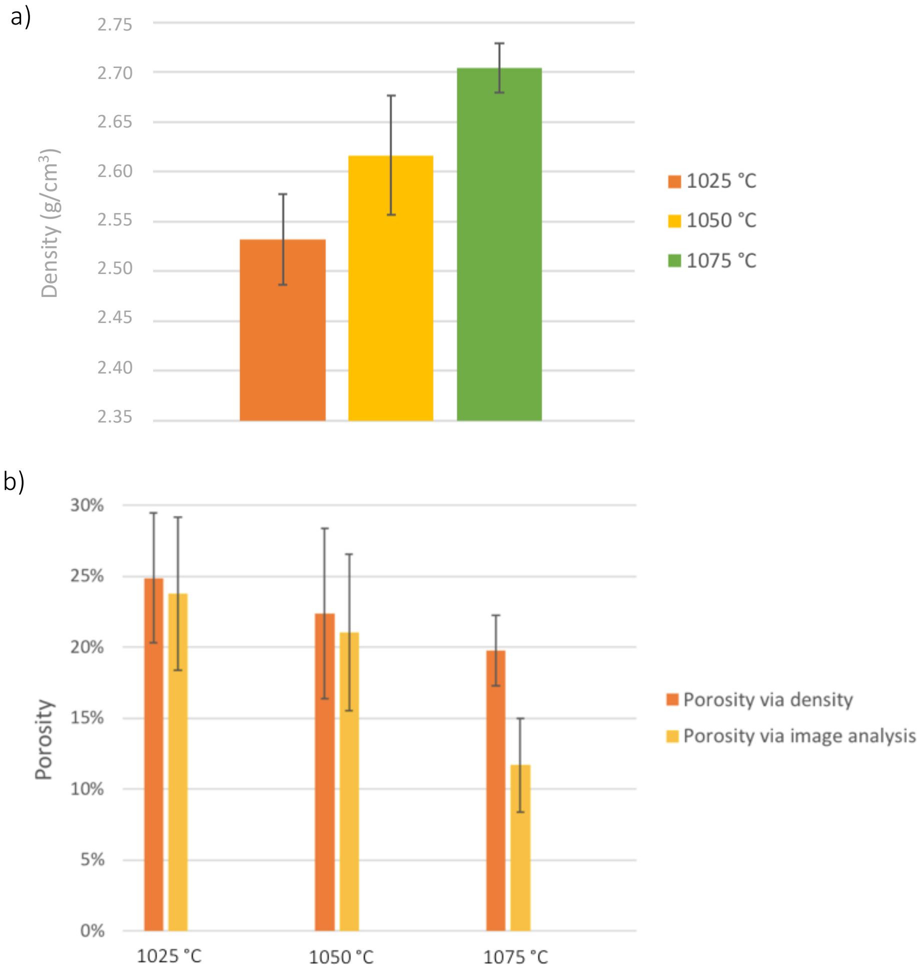

*Figure 59. a) Density and b) porosity of LHS-1 sintered samples*

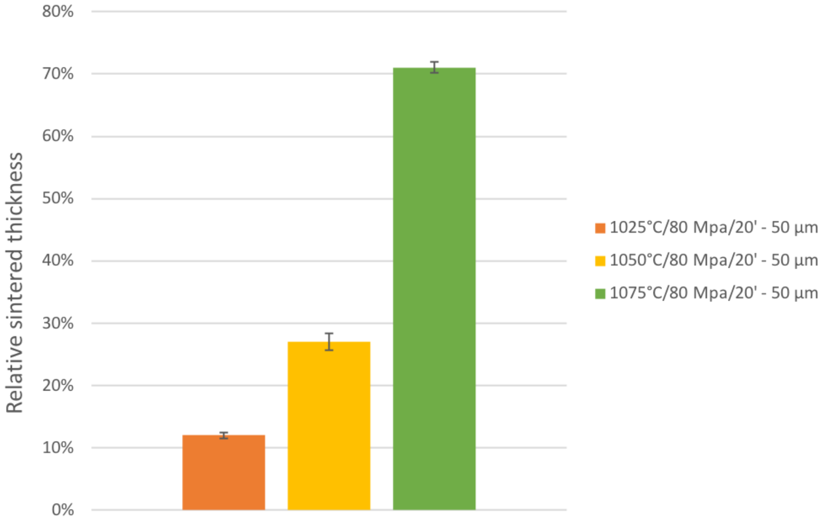

*Figure 60. Relative sintered thickness of LHS-1 sintered samples*

The microstructure of the samples was studied with SEM and their composition was also determined with XRD. Three different main phases are present in the sample whatever the sintering temperature is: an augite light grey phase [$Ca(Mg,Fe,Al)(Si,Al)_2O_6$], a sodian anorthite dark grey phase

[(Ca,Na)(Si,Al)$_4$O$_8$] and a white phase corresponding to an iron titanium oxide (figure 62). Augite is a pyroxene while sodian anorthite is a plagioclase mineral. In the as-received powder, according to the analysis made by ESA LHS is mainly composed of plagioclase minerals and also contains pyroxene. However, the exact nature of the pyroxene and plagioclase minerals are not known. During the SPS experiment, the sodian anorthite could have transformed to augite. The augite is often found as "smashed or crushed" particles within the anorthite phase as on Figure 61. This microstructure might be due to the pressure applied during SPS. The partially dissolved anorthite can be pushed in between the augite smashed particles with the application of the external pressure. Anorthite has a lower melting point and a lower modulus than augite: anorthite is then more prone to experience plastic deformation under pressure than augite and can fill the gaps between the smashed augite particles [13]. This specific microstructure is observed for all the samples at different sintering temperatures.

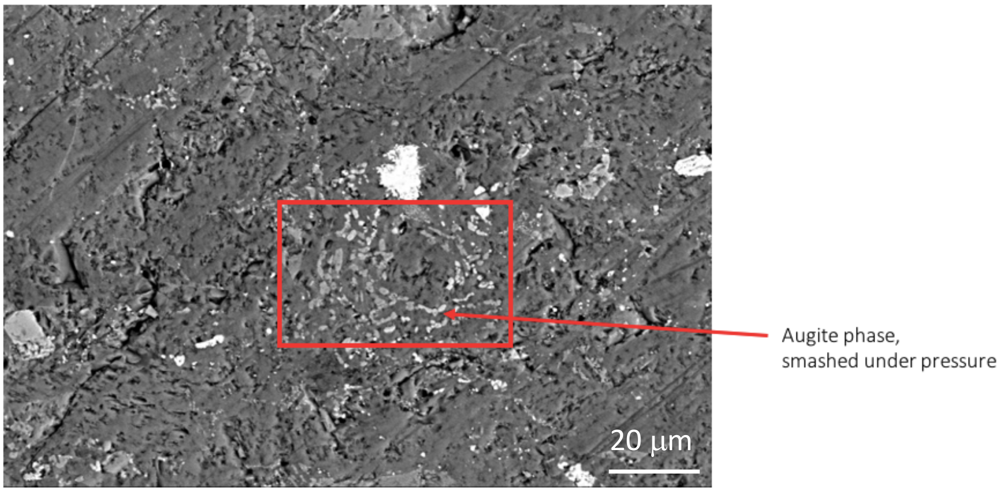

*Figure 61. Microstructure of the sintered side of LHS/1050 °C/80 MPa*

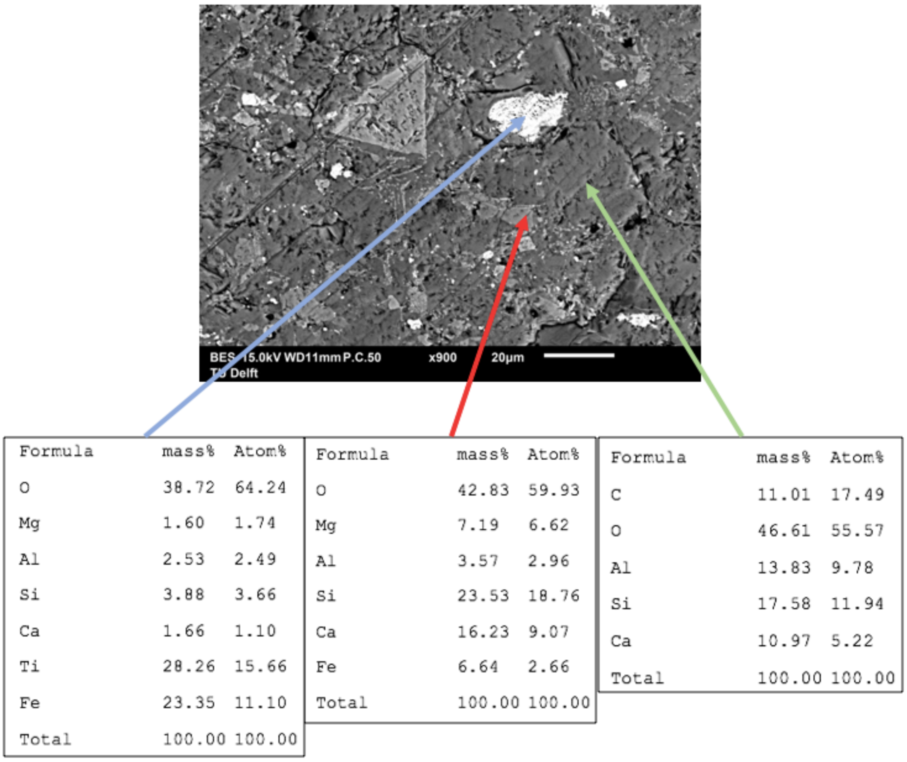

```
Formula         mass%   Atom%
O               38.72   64.24
Mg               1.60    1.74
Al               2.53    2.49
Si               3.88    3.66
Ca               1.66    1.10
Ti              28.26   15.66
Fe              23.35   11.10
Total          100.00  100.00
```

```
Formula         mass%   Atom%
O               42.83   59.93
Mg               7.19    6.62
Al               3.57    2.96
Si              23.53   18.76
Ca              16.23    9.07
Fe               6.64    2.66
Total          100.00  100.00
```

```
Formula         mass%   Atom%
C               11.01   17.49
O               46.61   55.57
Al              13.83    9.78
Si              17.58   11.94
Ca              10.97    5.22
Total          100.00  100.00
```

*Figure 62. EDS analysis of 3 phases for sample LHS/1050°C/80 MPa*

The EDS analysis was completed with XRD analysis of the surface of the different sintered samples. The XRD patterns for the three different sintering temperatures looks very similar: all samples exhibit the same diffraction peaks and are then composed of the same minerals (figure 63). The intensity of the peaks differs but no main difference is shown with XRD. It is in good accordance with the SEM images: the same three phases are distinguished: augite, sodian anorthite and an iron titanium oxide. The compositions of the sintered samples are very similar to the composition of the as-received powder: spark plasma sintering did not cause the formation of new phases or oxides.

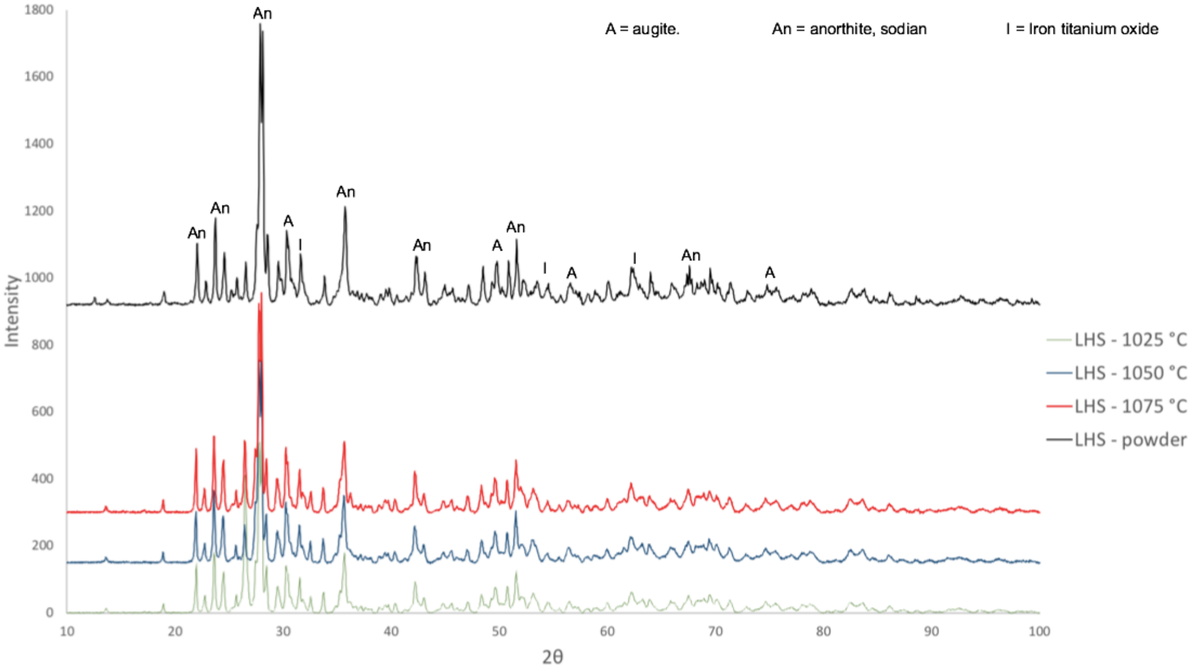

*Figure 63. XRD - LHS-1 powder and sintered LHS-1 samples*

Moreover, carbon diffused during the SPS process as shown on the EDS measurement in figure 64. Indeed, carbon was detected with EDS only on the outer part of the samples. This carbon comes from the graphite foil used to prevent the powder from sticking to the mould during SPS. Boron nitride was sprayed on the graphite foil to avoid this diffusion, but a small portion of carbon still diffuses into the samples. Carbon diffusion is a thermally activated process and so the carbon diffusion increases when using higher sintering temperatures and higher pressure. Carbon only penetrates over a small layer of the sample and this layer can be removed by mechanical polishing. On EDS, the carbon was homogeneously present and did not form carbides.

| Formula | mass% | Atom% |
|---|---|---|
| C | 11.76 | 18.28 |
| O | 48.83 | 56.99 |
| Al | 13.84 | 9.57 |
| Si | 16.30 | 10.83 |
| Ca | 9.29 | 4.33 |
| Total | 100.00 | 100.00 |

| Formula | mass% | Atom% |
|---|---|---|
| O | 52.10 | 66.57 |
| Mg | 0.99 | 0.83 |
| Al | 14.87 | 11.27 |
| Si | 22.88 | 16.65 |
| Ca | 9.17 | 4.68 |
| Total | 100.00 | 100.00 |

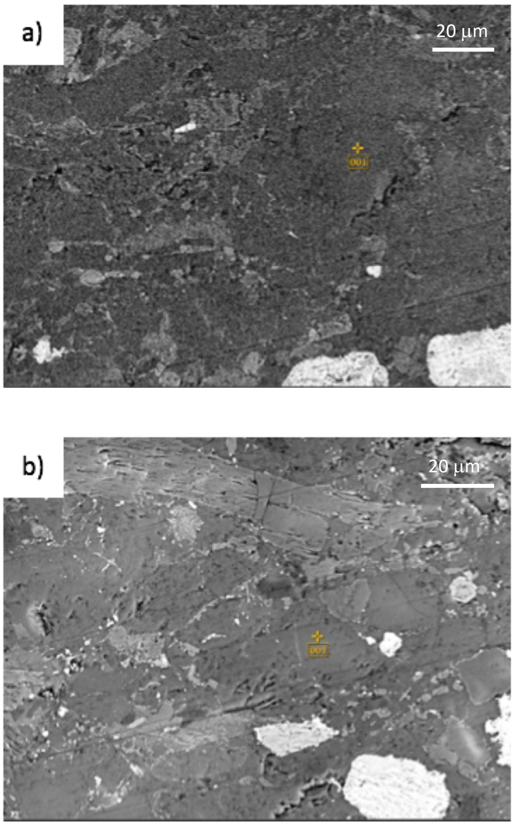

*Figure 64. Diffusion of carbon during SPS: a) EDS on side of the sample, b) EDS in the middle of the sample. Sample: LHS/1075 °C/80 MPa*

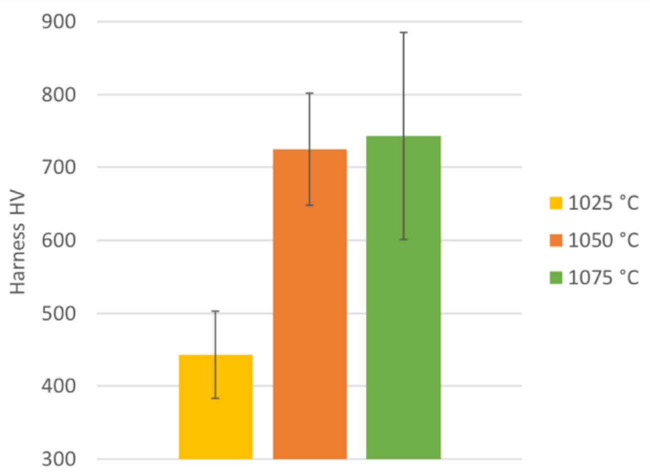

*Figure 65. Vickers hardness of samples of LHS-1 sintered at 3 different*

The Vickers hardness increases with the temperature (figure 65). A significant increase is observed between a sintering temperature of 1025 °C and 1050 °C. The hardness measurement is in accordance with the microstructure of the sintered samples. The high standard deviation is related to the different phases present in the specimens and the position of the measurement. Moreover, the measurements have been made on the most sintered layer of the sample. The sample sintered at 1075 °C is almost fully dense and so, the measurements were made on a bigger surface.

To conclude, increasing the sintering temperature enhances the densification of the lunar regolith simulant and increases the hardness. A higher sintering temperature did not influence the phase composition of the specimens which remains the same whatever the sintering temperature.

### 4.2.1.2 Influence of particle size

The particle size distribution is important to take into account when performing sintering processes. The particles must be rearranged in the mold to have as few voids as possible. Coarse particles cannot pack as tightly as small particles and voids are inevitable between the particles. However, voids between small particles are easily closed during spark plasma sintering while coarse voids are not. A good balance of small particles and coarse particles can also be advantageous because small particles surround the coarser particles and will form a matrix between them.

The first LHS-1 sintered samples at 975 °C gave an insight about the influence of the particle size: one of the samples was made with powder sieved to 100 μm and the other was made with powder sieved to 50 μm. Both samples were not highly densified, but the smaller particles help to have a more densified structure of the matrix between the voids (figure 66).

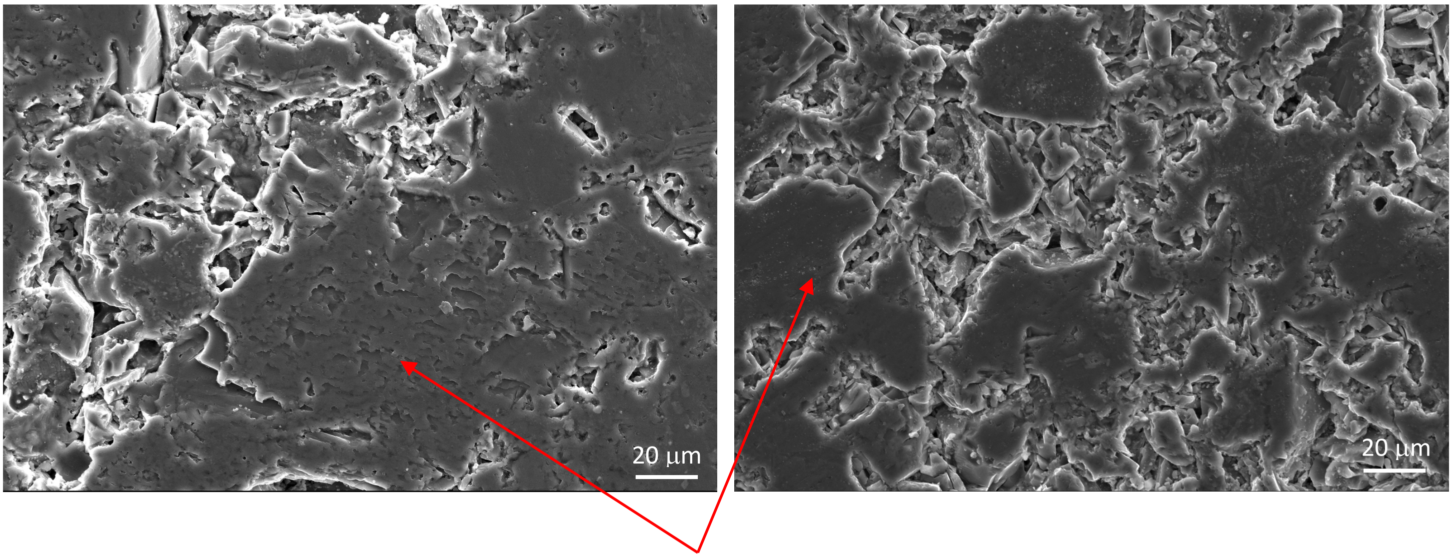

Denser matrix with smaller particle sizes

*Figure 66. Comparison of densification of matrix with different particle size of LHS-1: a) 100 µm and b) 50 µm*

As can be seen on figure 68, the samples with smaller particles showed higher densification. Moreover, the standard deviation is higher for the samples with coarser particles, which indicates that the microstructure is more heterogeneous (see figure 69). It should also be noted that more macro-pores were observed in the coarser 100 µm-sample. The presence of very coarse particles thus prevents the particles from good packing. The sample with the smallest initial particle size is the only sample that showed full densification along the vertical direction (figure 67).

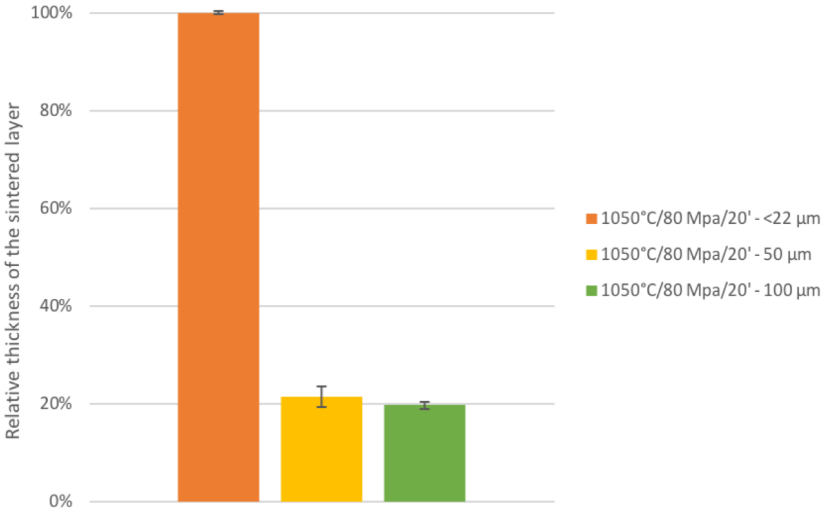

*Figure 67. Relative thickness (%) of the sintered layer of EAC-1A samples*

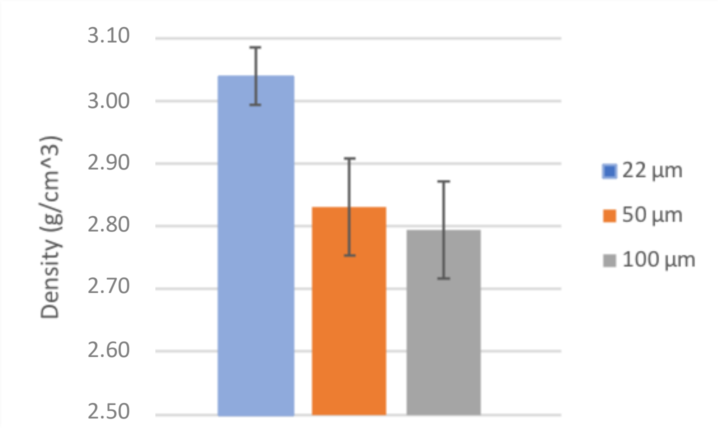

*Figure 68. Density of the EAC-1A sintered samples with different particle size*

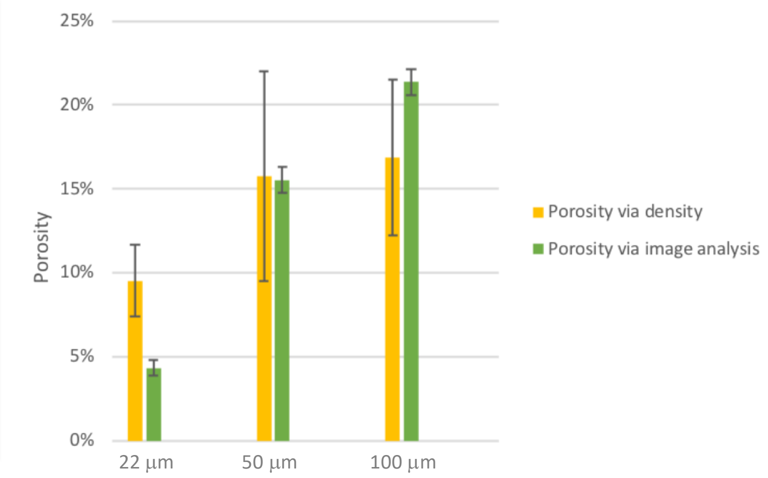

*Figure 69. Porosity of the EAC-1A sintered samples with different particle*

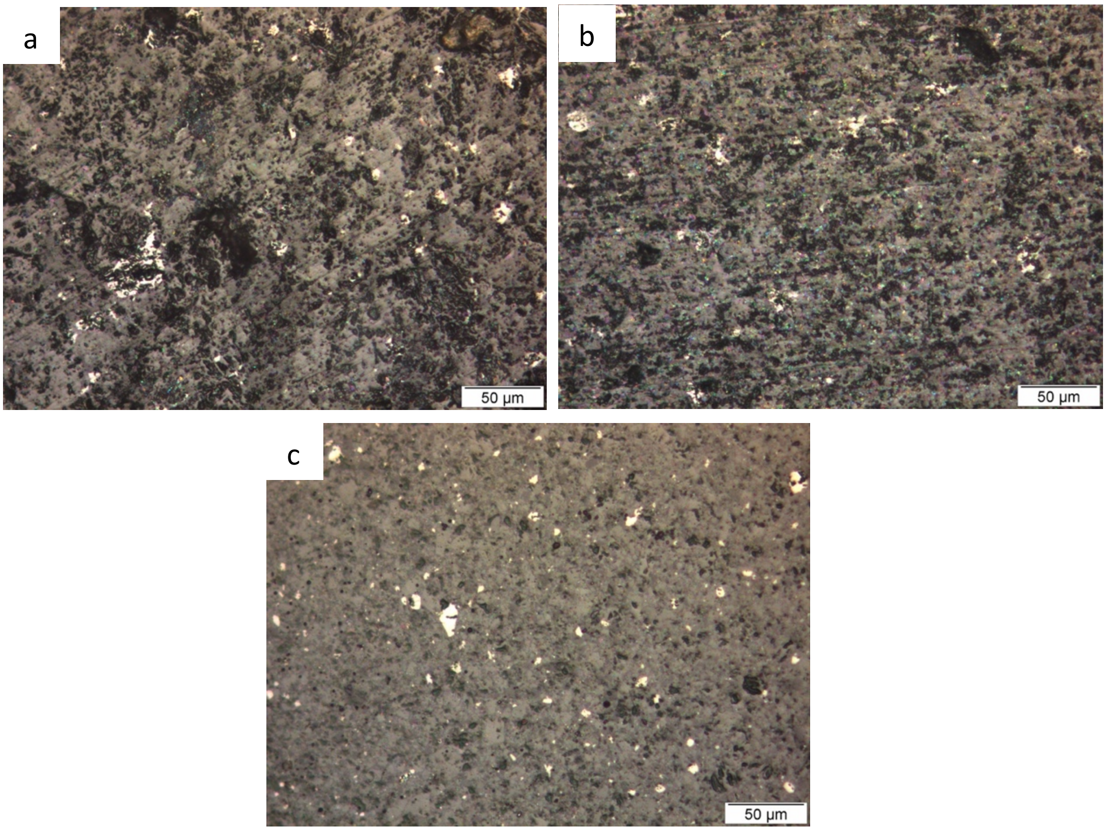

*Figure 70. Optical microscopy images of EAC-1A sintered samples of a) 100 $\mu$m, b) 50 $\mu$m and c) crushed powder.*

The higher densification of the samples with smaller particle can be related to several densification mechanisms: rearrangement of the particles, formation and growth of the sintering necks between particles, plastic deformation and densification. The smaller the particle size, the higher the surface energy driving force given in equation 21 is. The sintering of powder is enhanced by this higher driving force. It causes the migration of the particles and increases the contact area of the particles [66].

$$\Delta E = E_p - E_d \approx \gamma_{sv} W_m S_p \tag{21}$$

$$S_p \propto \frac{1}{R} \tag{22}$$

Equation 21 and 22 show the relationship between powder properties and the driving force for sintering, with $\Delta$E the intrinsic driving force, $E_p$ the surface energy of powder before sintering, $E_d$ the surface energy of powder after sintering, $\gamma_{sv}$ (J/m$^2$) the solid-gas surface energy, $W_m$ (g/mol) the molar mass of material and $S_p$ (cm$^2$/g) the specific surface area of powder, R the radius of the particle.

The tensile stress of the sintering necks increases with decreasing particles size and the strength of the sintering necks is higher between smaller particles. Only the use of crushed EAC-1A powder (with resulting 22 µm particles) led to a fully dense sample (figure 70). In the case of SPS, the surface of the particles is heated to high temperatures compared to the core of the particles due to spark discharge in the voids. In the case of small particles, the surface to volume ratio of the particle is bigger than for coarse particle. The amount of the powder subjected to high temperature is higher in the case of smaller particles, which leads to a more effective densification.

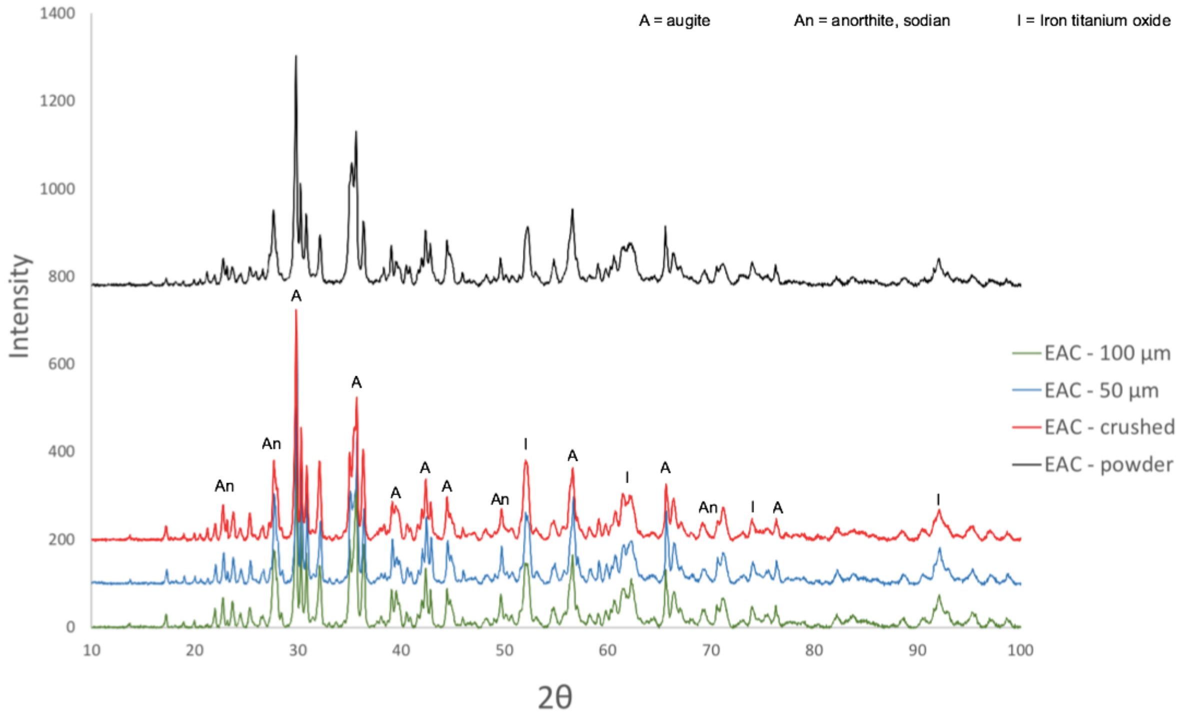

*Figure 71. XRD - EAC-1A powder and EAC-1A sintered samples*

XRD patterns (Figure 71) showed no significant differences between the samples consolidated with different particle sizes. Main identified phases were plagioclase, pyroxenes (augite and diopside) and iron titanium oxide. The composition of the sintered samples is close to the composition of the initial powder.

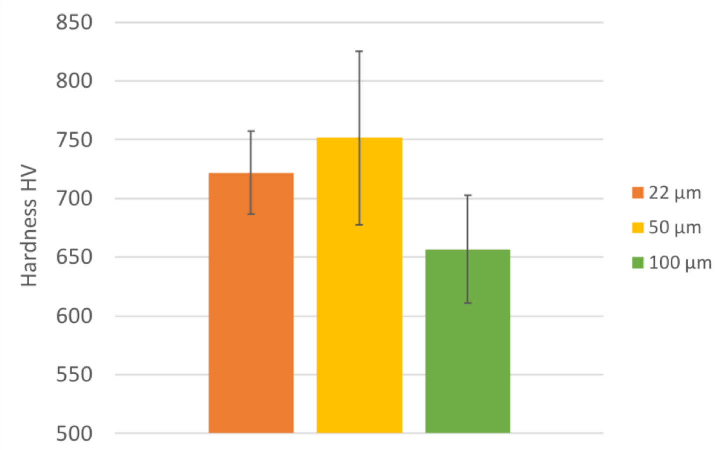

*Figure 72. Influence of particle size on Vickers hardness (EAC-1A)*

The hardness of the sample with coarse particles is lower than for the other samples (figure 72). The higher hardness for the sample with maximum 50 µm is associated with a higher standard deviation due to the different hardness of the particles. The hardness of the 22 µm-sample and 50 µm-sample are thus comparable. The hardness does not increase with powder milling because the phase composition remains similar; however it is more homogeneously distributed.

The fracture toughness was found to be 2.07 ± 0.14 MPa.m$^{1/2}$ for the most sintered sample with fine particles. This value falls between the fracture toughness of silica (0.62 – 0.67 MPa.m$^{1/2}$) [67] and the fracture toughness of alumina (3.3 – 5 MPa.m$^{1/2}$) [68]. Spark plasma sintering can be used to sinter the lunar regolith and obtained a fracture toughness similar to the one of common ceramics. This fracture toughness is relatively low for a space habitat and a thick wall would be required to avoid early fracture of the space habitats surface.

### 4.2.1.3 Influence of composition

The influence of the composition was studied by sintering the three different lunar regolith simulants under the same conditions: 1050 °C, 80 MPa and powders sieved to 50 μm. All 3 samples were densified to a similar level and none of the powders melted under these sintering conditions.

EAC-1A and LMS-1 samples were more densified than the LHS samples when comparing the density and porosity measurements (Figure 73). It should however be noted that a thicker layer of highly dense material was measured for the LHS-1 sample (Figure 74). It means that the average porosity is lower for LMS-1 and EAC-1A, but LHS-1 has a more heterogenous porosity with a highly densified part. All three simulants were found to be composed of the same oxides and minerals: thus they have comparable temperature of phase transitions, so a similar SPS behaviour can be expected.

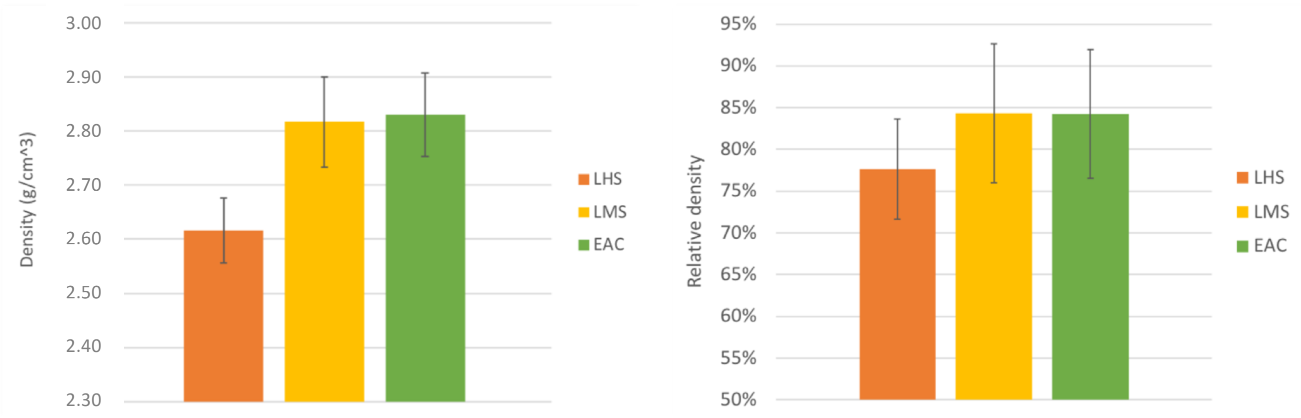

*Figure 73. Density and relative density of samples sintered under same conditions with different lunar regolith simulants*

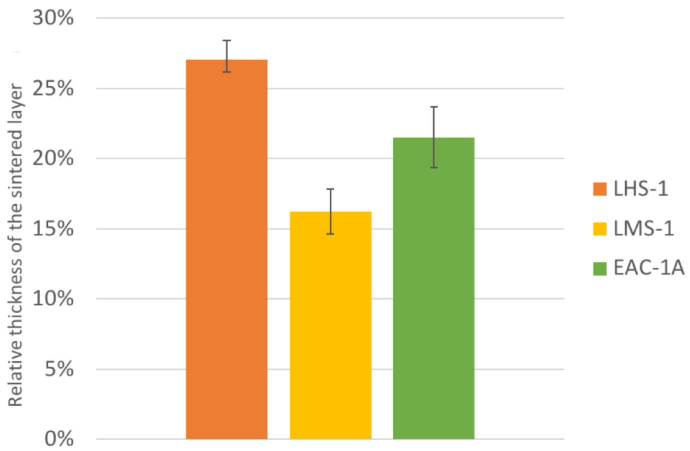

*Figure 74. Relative sintered thickness with different lunar regolith simulants*

The microstructures of the sintered samples were also comparable. All three simulants were found to be composed of the same oxides and minerals: thus they have comparable temperature of phase transitions and a similar SPS behaviour can be expected.

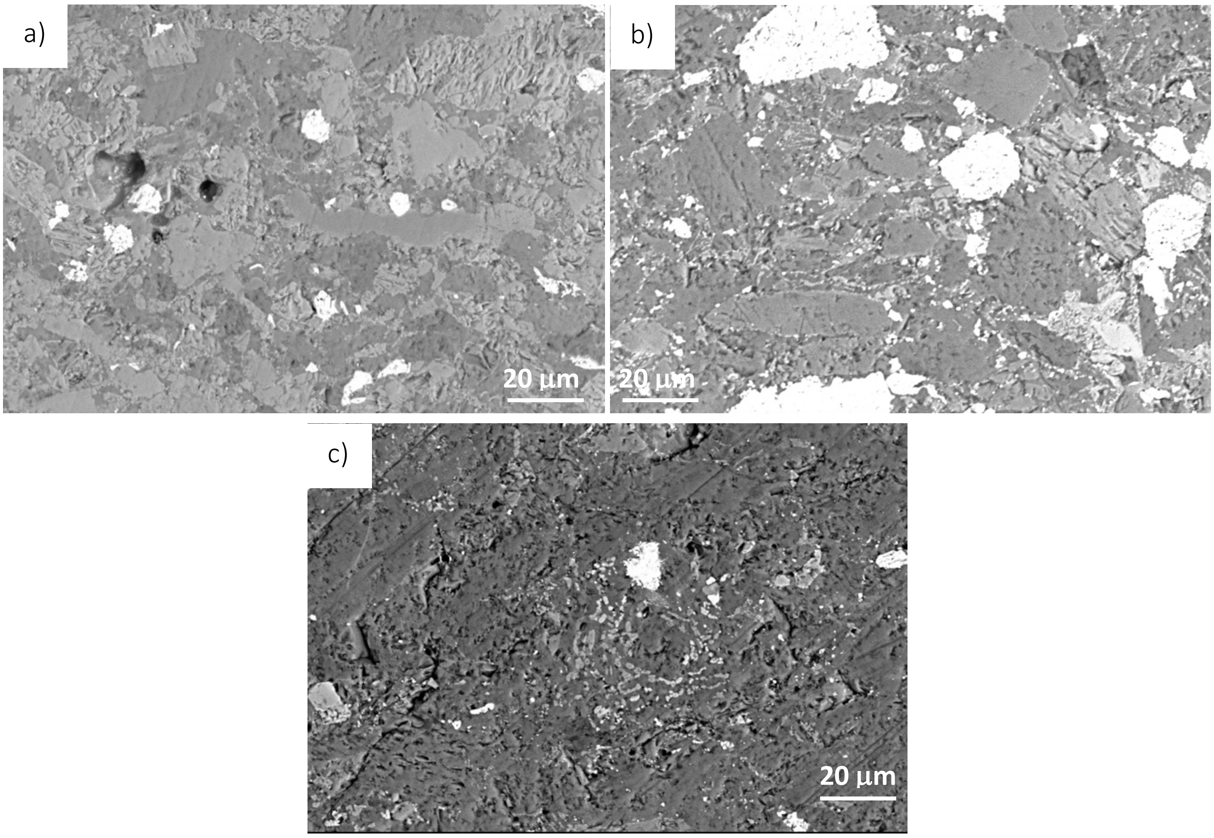

*Figure 75. SEM images of samples sintered at 1050 °C under 80 MPa with a particle size of 50 µm: a) EAC-1A, b) LMS-1 and c) LHS-1*

The Vickers hardness of the samples was not affected by the difference of simulant's composition (figure 76). The hardness of the samples has been measured only on the most sintered part of the sample. In the case of LMS, this layer is thinner, and the higher standard deviation could be explained by a low accuracy of the average. Moreover, LMS has more iron titanium oxide phases (figure 75-b) and the standard deviation could be influenced by the presence of these phases at some locations of the material.

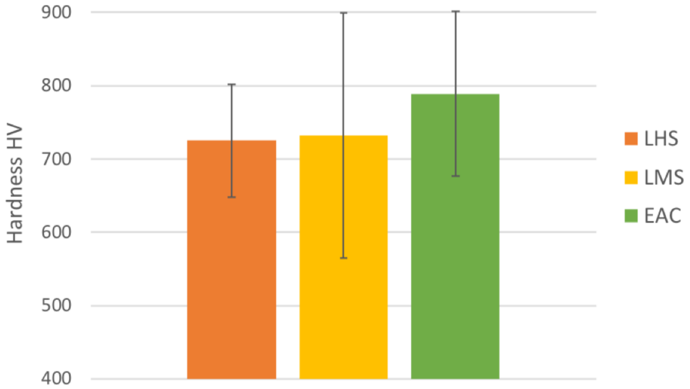

*Figure 76. Vickers hardness of sintered samples with different composition*

The different composition of the simulants does not have a significant effect on the sintering ability of the lunar regolith simulants. These results show that any type of lunar dust could be sintered with SPS whatever their composition.

### 4.2.2 Sintering of the metallic powders

The second stage of the Spark Plasma Sintering study was to determine some parameters to sinter the metallic powders that would be used for the functionally graded materials. Different set of parameters were determined with a literature research and the best combination was then chosen to perform some sintering of functionally graded materials. The parameters for the metallic powders were not firstly considered in regard to the parameters of the lunar regolith simulants but close parameters were a bonus to consider one-step sintering process.

#### *4.2.2.1 Stainless steel 316*

Three sets of parameters were chosen to sinter the stainless steel powder based on several researches [54] [55]. All 3 samples were almost fully dense after having been sintered with SPS (Figure 77).

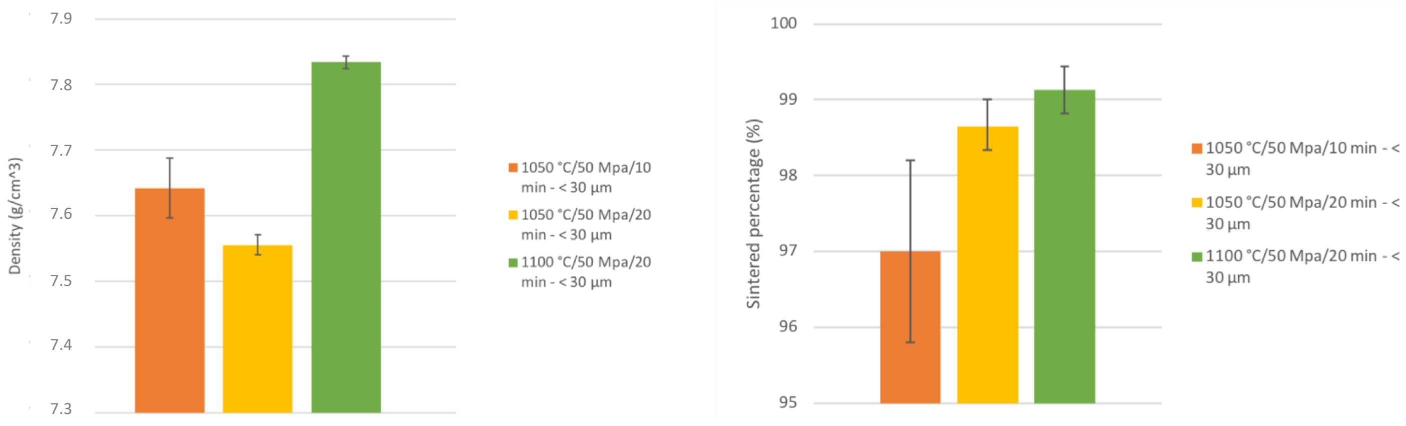

*Figure 77. Density and sintered percentage of SPS 316L*

Increasing temperature increases the density. For our experiments, it seems that increasing the holding time from 10 to 20 minutes leads to a decrease in density. However, it should however be noted that the observed density decrease is relatively low as compared to some other works showing density [55].

The decrease in density could be due to poor rearrangement of the particles during sintering preventing the pores to close or to a different balance between open pores and closed pores. The Archimedes measurements only take into account the open pores. However, considering the measurements of the porosity with optical images, the porosity reduces when increasing the temperature. Moreover, the standard deviation is much higher is the case of lower temperature and lower holding time which reveals inhomogeneity of pores distribution within the samples. Temperature seems to be the most important factor to improve the efficiency of sintering regarding both density results and hardness results.

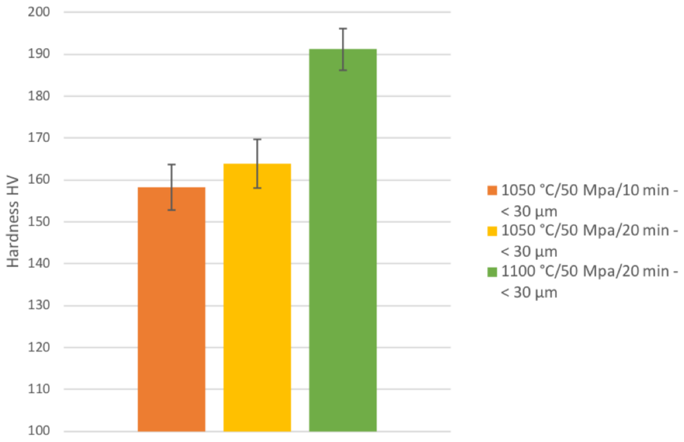

*Figure 78. Vickers hardness for SPS stainless steel samples*

The hardness (Figure 78) increases with increasing sintering temperature. The hardness for the samples sintered at 1050 °C are in the same order as the hardness of cast annealed 316 alloys. The samples sintered at 1100 °C shows a much higher hardness. The hardness was average on the whole sample and the standard deviation is quite small for all three samples: the microstructure and composition are likely to be homogeneous.

The SEM images and EDS measurements (figure 79) reveal a homogeneous microstructure for all the sample and did not show precipitates. Some nanoprecipitates such as carbides due to carbon diffusion could be there but are not visible on the magnification used. Some authors reported the presence of carbides on grain boundaries [55] but these carbides are only present on a small thickness of the samples' edges.

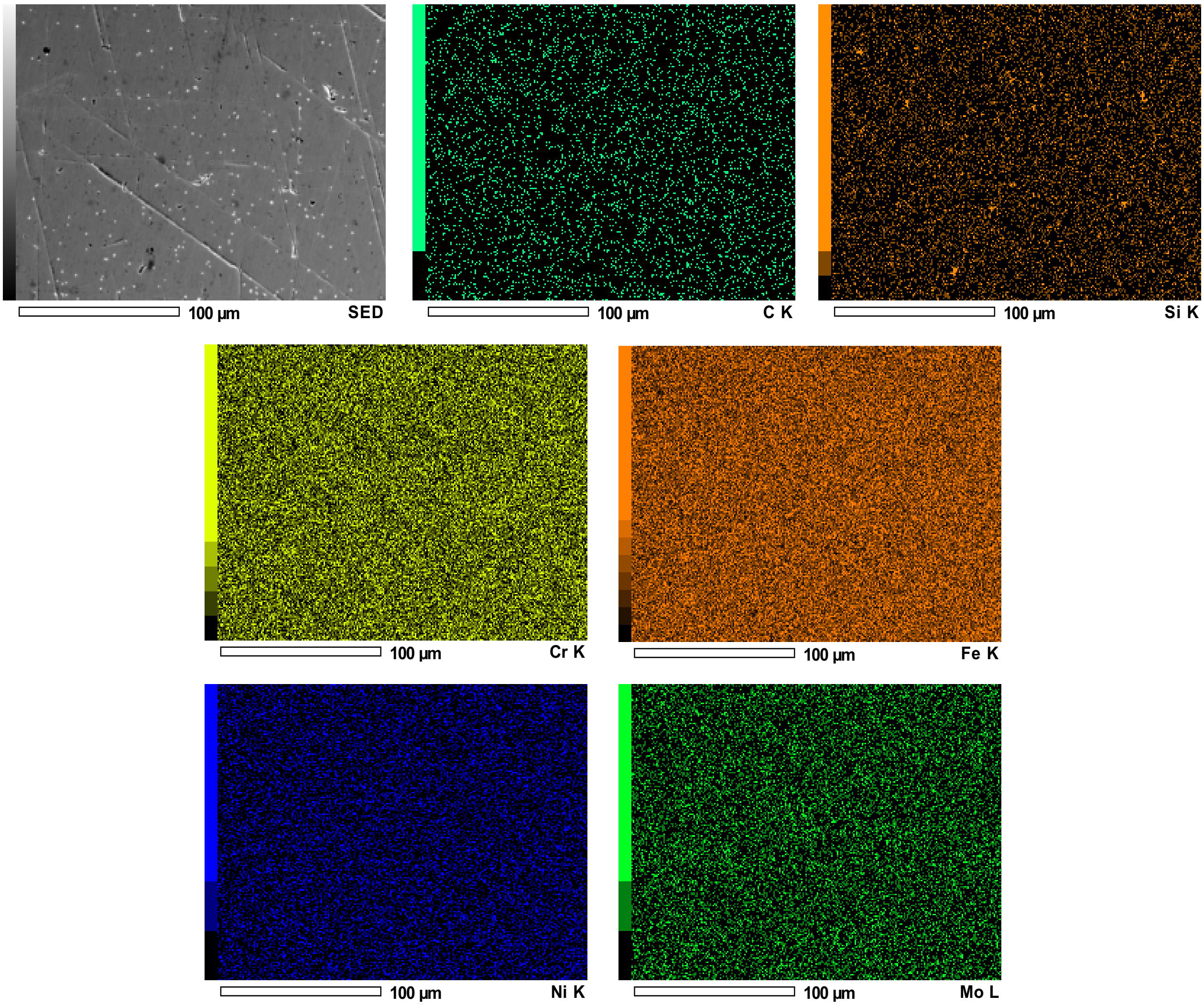

*Figure 79. EDS of sintered 316 at 1100 °C*

XRD results shows that only austenite is present in the samples (figure 80). This fully austenistic microstructure was also observed by Keller and al. [69].

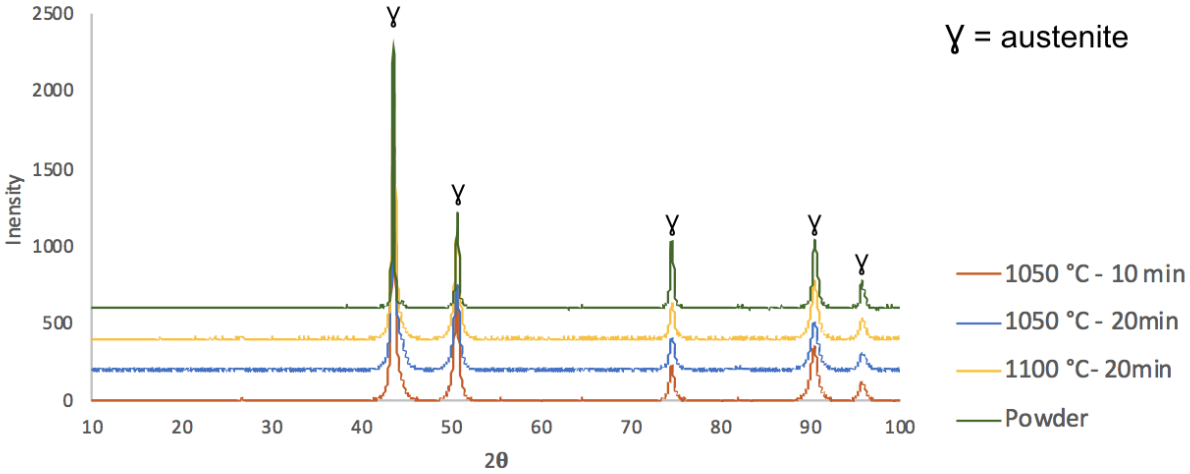

*Figure 80. XRD patterns of SPSed stainless steel as compared with as-received powder.*

### 4.2.2.2 $Ti_6Al_4V$

Two different sets of parameters were used to sinter the titanium alloy and determine which parameters gave the most densified structure. Both samples were very well sintered and showed almost no porosities (Figure 81). The high densification of the $Ti_6Al_4V$ samples is due to different mechanisms. The uniaxial pressure of 50 MPa is useful to help to rearrange the particles, to break the agglomerates and to induce plastic deformation at high temperatures. Moreover, another mechanism is important: Joule heating effect derived from the pulsed current. The current can flow through the powdered sample since titanium alloy is conductive and the particles heat up, especially at the surface of the particles. The temperature is then higher at the contact point between particles and the diffusion is increased that leads to a higher and easier densification [70].

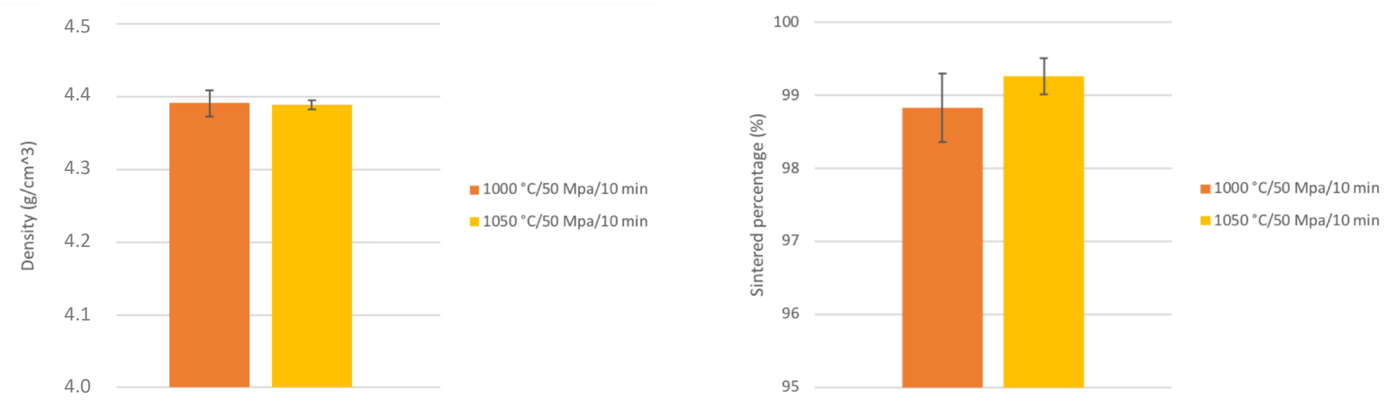

Figure 81. Density and sintered percentage of $Ti_6Al_4V$ samples

The elements Ti, Al and V are evenly distributed (figure 83), and no precipitates are formed during the sintering process. Moreover, no shapes of particles are visible which allows us to consider that sintering was successfully undergone. XRD results showed that the same phases forms at the 2 different sintering temperatures (figure 82). The $\alpha$-Ti phase is present as in the as-received powder but a second phase is detected: $Ti_{0,8}V_{0,2}$ which is a $\beta$-Ti structure.

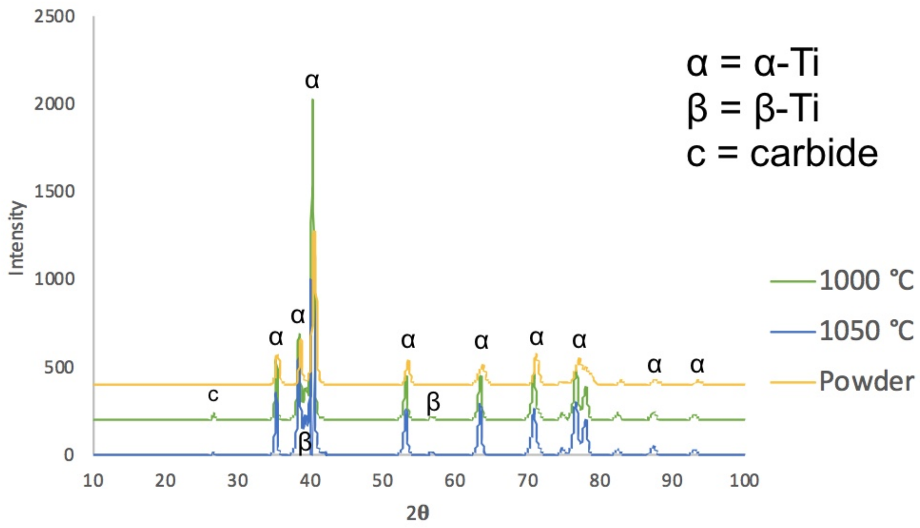

Figure 82. XRD patterns of SPSed $Ti_6Al_4V$ as compared with as-received powder.

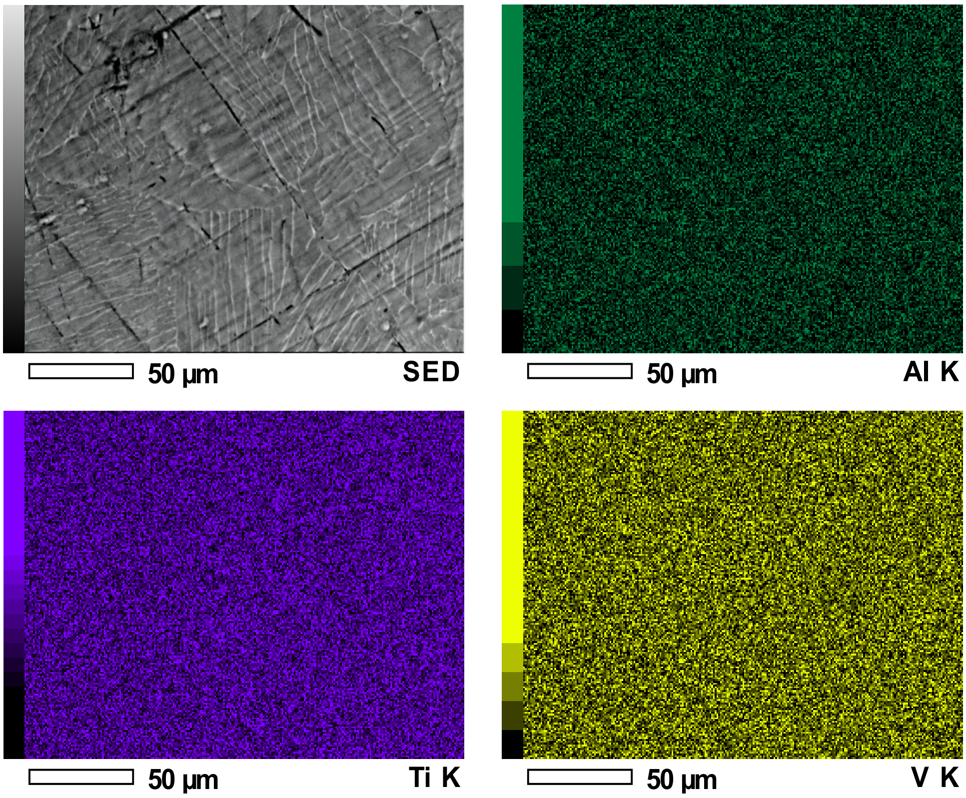

*Figure 83. EDS analysis of $Ti_6Al_4V$ sintered at 1050 °C*

The microstructure analysis reveals the presence of clusters of grains elongated in the same direction (figure 84). The recrystallisation of the grains is not hindered by the presence of intermetallic at the grains boundaries or by interstitial solute atoms as shown by Long and al. [71].

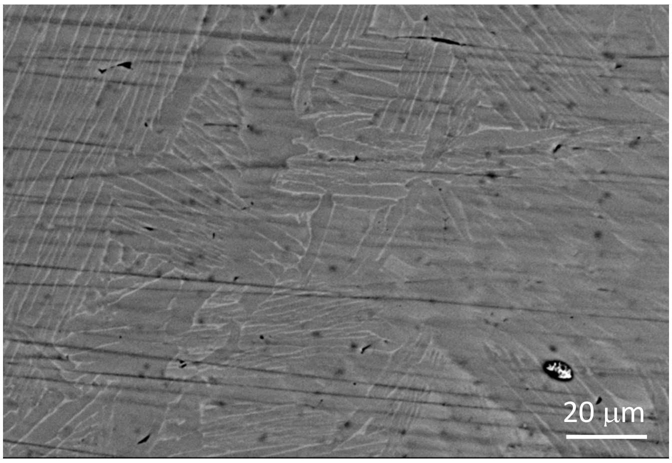

*Figure 84. Sintered Ti6Al4V showing equiaxed grains*

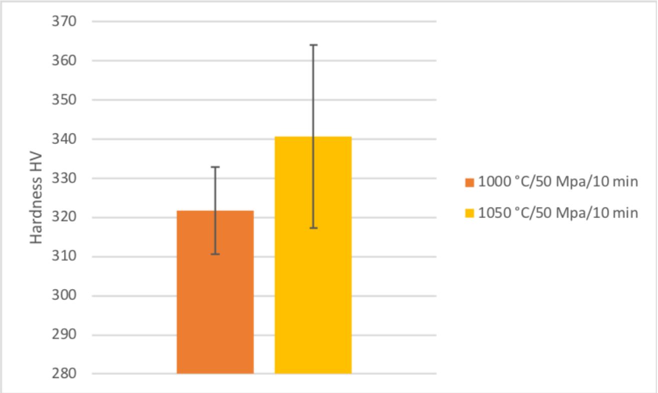

*Figure 85. Vickers hardness of $Ti_6Al_4V$*

The Vickers microhardness was 341 ± 23 $HV_{0,5}$ for the samples sintered at 1050 °C compared to 322 ± 11 $HV_{0,5}$ for the sample sintered at 100 °C (figure 85). These values are in the order of the Vickers hardness for $Ti_6Al_4V$ cast alloys [72].

The set of parameters 1050 °C, 50 MPa and holding time of 10 min was chosen as for the functionally graded materials with lunar regolith simulant. The sample was more densified, and no precipitates formation of liquid sintering occurs during the SPS process and the temperature was closer to the one chosen for the regolith.

### 4.2.3 Functionally Graded Materials

After the study of optimal parameters for SPS for the different materials, functionally graded materials were made.
The hardness profile of the FGM with different metal powders are compared below and will be discussed separately in the following sections (figure 86).

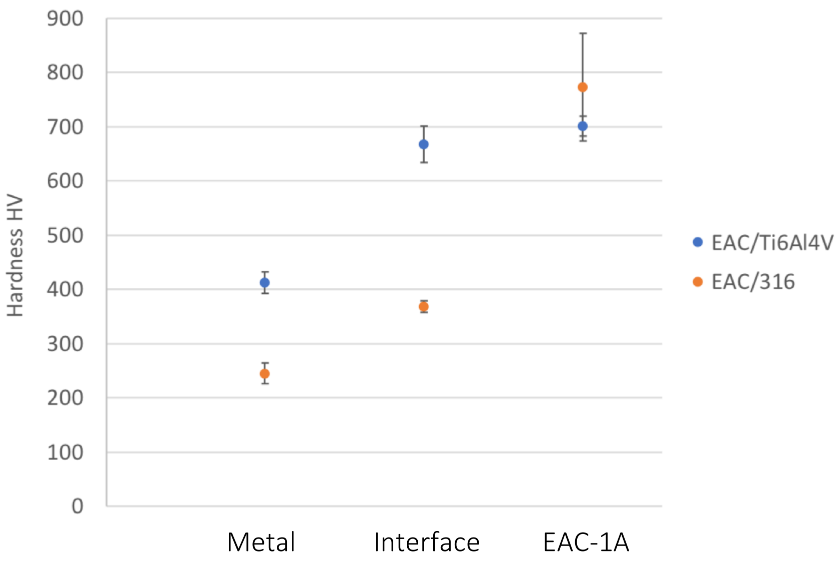

*Figure 86. Profile of Vickers hardness of the functionally graded materials*

#### 4.2.3.1 EAC-1A/316

The FGM samples of stainless steel and EAC-1A have been performed under 3 different conditions: 2 samples were made in one step and one sample was made in a two-step sintering process.

The sintering experiments in one step lead to inconsistent FGM. The one-step sintering at 1100 °C under 50 MPa leads to the complete melting of the lunar regolith simulant which squeezes out of the mould. The surface of the metal part did not show any remnants of the lunar regolith. This experiment points out that sintering at 1100 °C under 50 MPa is not possible for the lunar regolith simulant.

When sintering both powders at 1050 °C under 50 MPa, the FGM did not keep its shape and, EAC-1A and stainless steel layers were sintered separately. Both layers exhibit cracks or more pores at their side supposed to be the interface of the FGM (Figure 87).

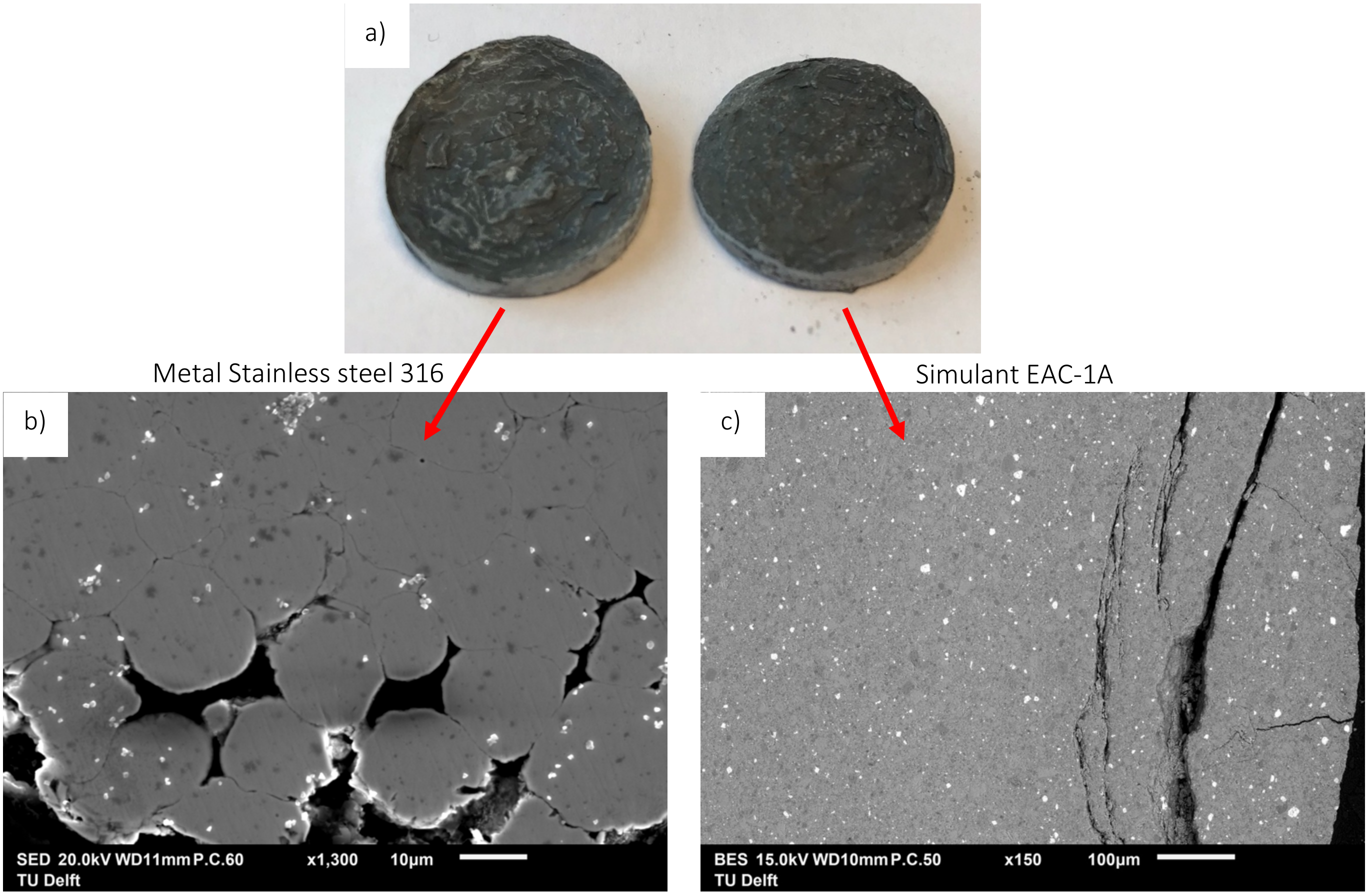

*Figure 87. a) FGM 316/EAC after sintering at 1050 °C. SEM images of the interface between the 2 materials: b) SS 316 and c) EAC-1A*

Sintering in one step has not been successful for these powders. The pressure of 50 MPa might be too low to allow good sintering of the 2 powders: a minimal pressure of 80 MPa seemed to be required to sinter the lunar regolith and a high pressure might also be required to allow sintering at the interface.

The sintering in two steps leads to a sintered specimen broke into two pieces. However, it has not been broken at the interface. Moreover, a temperature of 1100 °C is too high to sinter the lunar regolith when a pressure is applied. A maximum temperature of 1050 °C should be used to avoid melting of the powder; a temperature of 1075 °C might be used to have a local melting of the powder which could help at the interface.

A sintering in two steps proved to be more successful. The FGM broke when removed from the mould but it did not break at the interface: the sample broke within the lunar regolith layer (figure 88).
The SEM images revealed the presence of a grey phase at the interface. According to EDS (Figure 89), the interface has a higher chromium concentration than the inner layers. Chromium tends to diffuse to the interface from the stainless steel and form a high-content Cr phase that is likely to be BCC-A2 phase according to Thermocalc® calculations and composition from EDS.

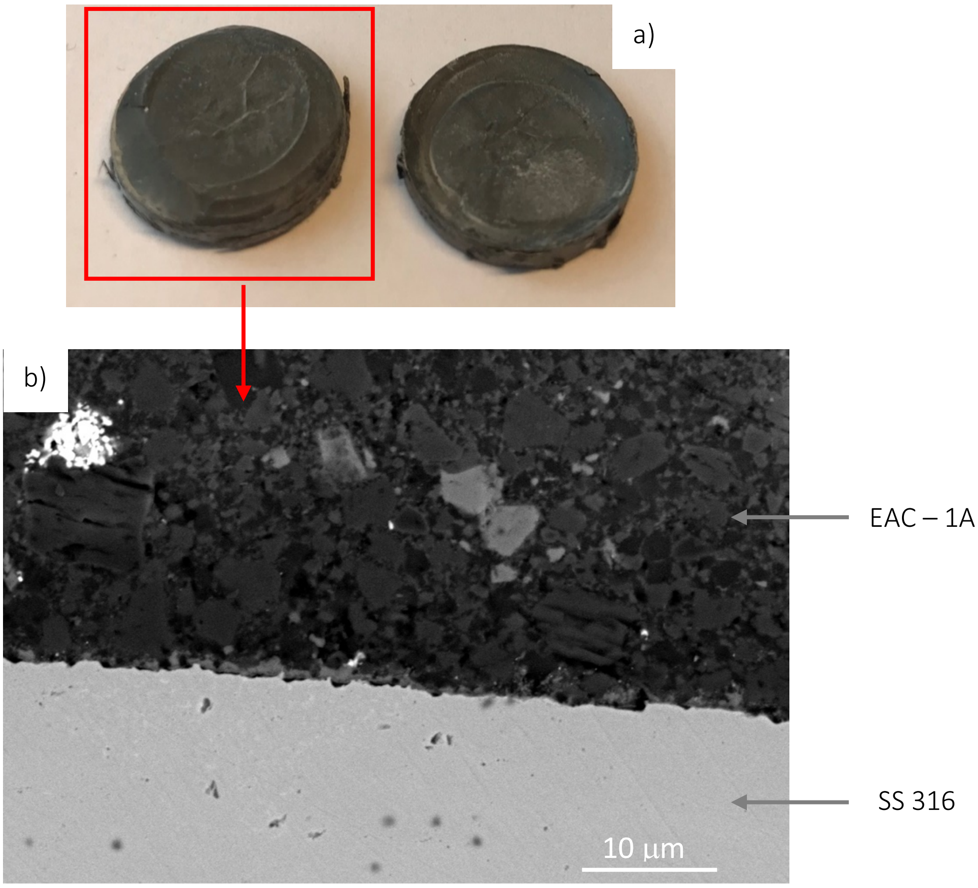

*Figure 88. a) FGM SS-316/EAC-1A after sintering in 2 steps and b) SEM image of the interface between SS-316 and EAC-1A*

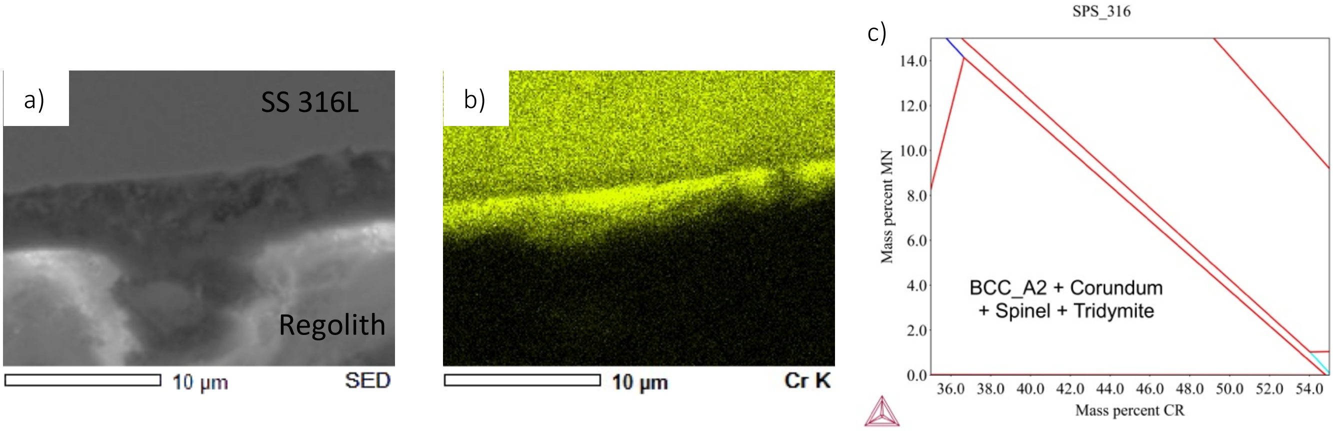

*Figure 89. a) SEM image of interface of FGM 316/EAC, b) EDS map of Cr at the interface of FGM 316/EAC and c) Thermocalc graph for Cr diffusion.*

The profile of hardness for the steel/EAC functionally graded materials showed that the interface as a Vickers hardness close to the one of the metal part. The change in hardness between the interface and the lunar regolith is then huge and this change could explain the poor sintering properties of this FGM.

Furthermore, the coefficient of thermal expansion of stainless steel 316 is twice as big as the CTE of the lunar regolith (compared with the CTE value of the lunar regolith simulant JSC-1A [73]). This mismatch in thermal properties induces thermal stresses during SPS cooling stage and these stresses can explain why the FGMs cracked during sintering.

#### *4.2.3.2 EAC-1A/Ti$_6$Al$_4$V*

The sintering of Ti$_6$Al$_4$V and EAC has been successful. The samples did not break when removed from the mould as shown on Figure 90. The Vickers hardness profile of this FGM shows a gradual increase at the interface. The hardness of the interface is close to the hardness of the lunar regolith.
The coefficient of thermal expansion of Ti$_6$Al$_4$V and lunar regolith simulant are very close (about $8 \times 10^{-6}$ $K^{-1}$ for both materials [73]): it avoids potential high thermal stresses during sintering and especially during cooling stage.

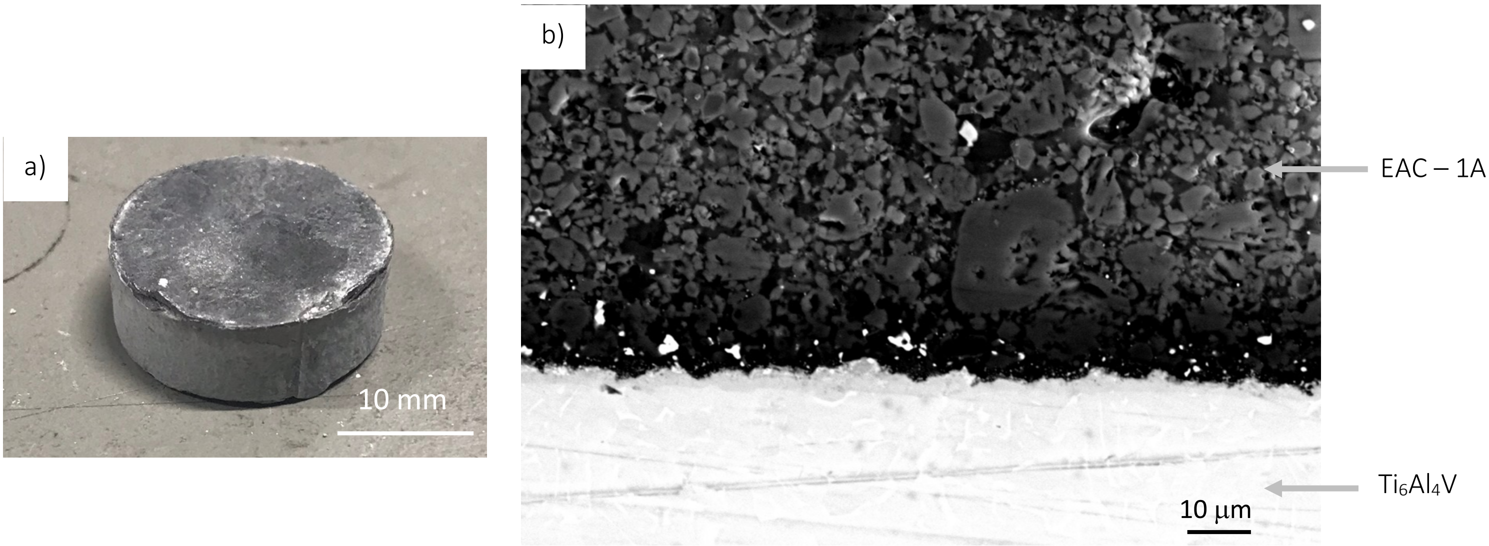

*Figure 90. a) FGM Ti$_6$Al$_4$V/EAC-1A after sintering in 2 steps and b) SEM image of the interface between Ti$_6$Al$_4$V and EAC-1A*

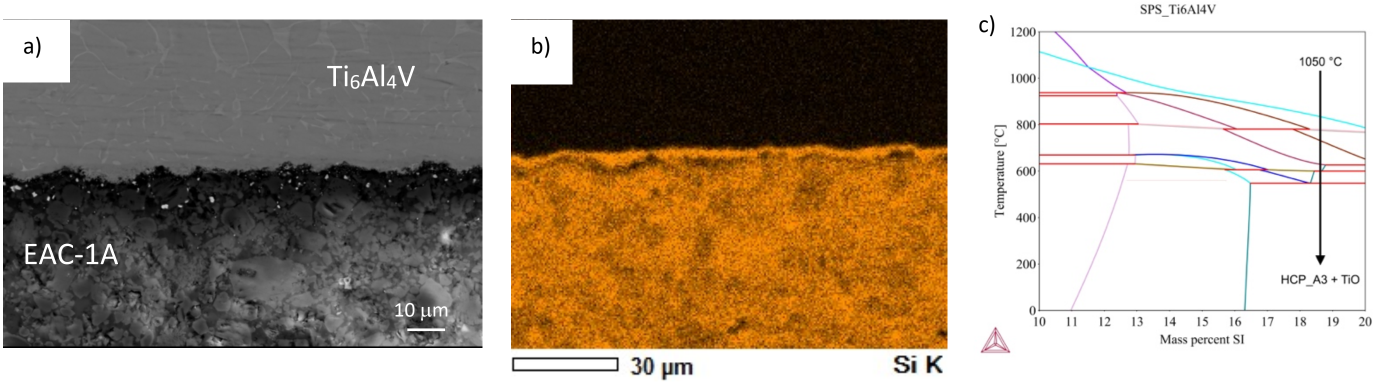

*Figure 91. a) SEM image of interface of FGM Ti6Al4V/EAC, b) EDS of Si at the interface of FGM and c) Thermocalc® graph for Ti6Al4V/EAC interface*

SEM images reveals the presence of white particles at the interfaces and did not show pores at the interface. These particles should be titanium oxide according to EDS and Thermocalc® calculations. Moreover, EDS measurements revealed a segregation of silicon at the interface (figure 91). According to Thermocalc® calculations, a liquid phase rich in Si may form during SPS at 1050 °C and silicon contribute to the formation of $Ti_xSi_y$, an HCP phase at the interface.

## 4.3 Laser melting

During the Spark Plasma Sintering runs, some melting of the lunar regolith simulant powders happened when higher temperatures were tried. The EAC-1A powder melted during the one-step SPS run for the FGM samples with stainless steel at 1100 °C and a trial at 1200 °C was also made to see the effect of pressure on the DLP powder. Melting of the powder at temperature around 1100 °C was a starting point for the trial of laser additive manufacturing technique. The lunar regolith could be used as a cladding for metallic parts to protect them against environment issues. A laser based additive manufacturing technique could eventually be used to manufacture whole FGM.

Three different spot size have been chosen for the laser lines trials that give three different energy densities. The first observation is that higher spot size (i.e. smaller energy density) results in a more continuous line. Indeed, when using higher energy density, only a portion of the powder melts and sticks to the ceramic plate, as seen in Figure 92. However, even the smaller energy density gives an incomplete laser line: smaller energy might be required, or the inhomogeneous surface of the used plate could also be a reason for incomplete melted lines.

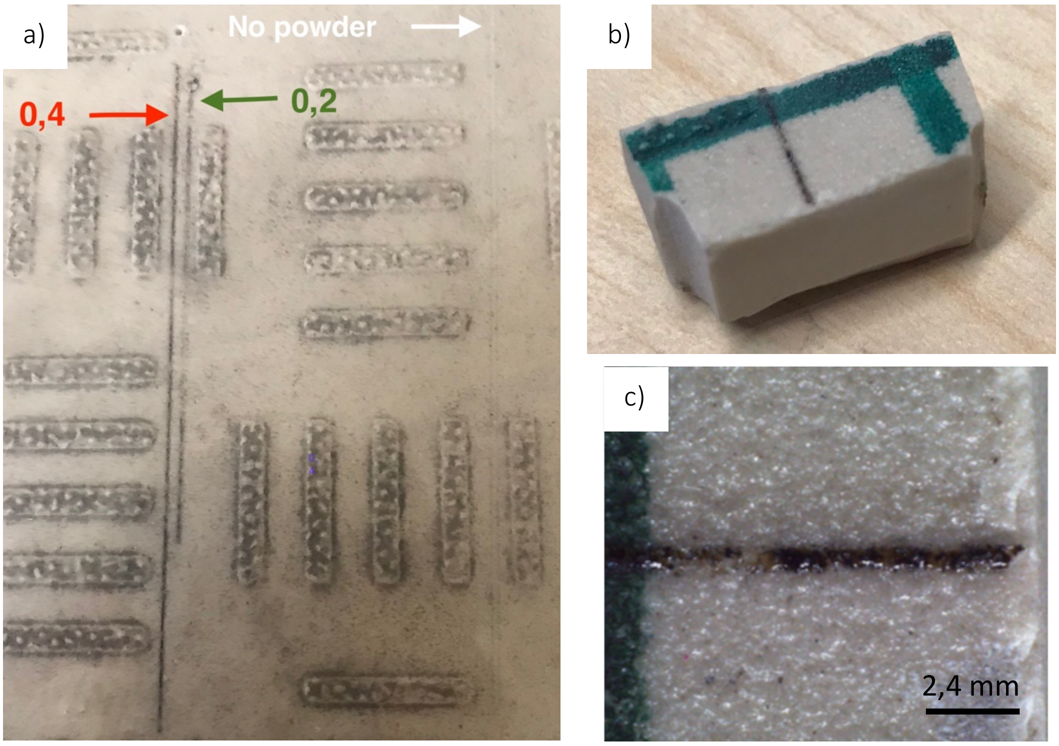

*Figure 92. Laser scanned lines: a) 2 laser scanned lines with different laser spot size and 1 line without powder, b & c) laser scanned lines with laser spot size of 0,6 mm*

The morphologies of the laser lines are relatively similar. The tracks exhibit the microstructure of solidified layer after being molten. The surface is smooth and exhibits patterns of a wavy melt pool.

Besides, they all exhibit cracks perpendicular to the scanning direction of the laser. These cracks could result from thermal stresses arisen during the cooling of the liquid powder or due to thermal stresses between the plate and the solidified regolith powder.

Only a small portion of particles are seen on the SEM images indicating that the powder almost completely melted during the laser melting experiments: the energy density is then enough to melt the powder. However, the particles of the lunar regolith have different composition and the softening/melting point differs between minerals. The parameters for a technique like selective laser melting should then be optimized to melt all different minerals without causing too much defects.

The big holes on the SEM image on Figure 93 might be related to a default in the powder bed: a lack of powder could explain this. Moreover, on SEM images, some small holes are present. The lunar regolith simulants have particles with irregular shapes and they cannot be smoothly spread on the substrate as spherical particles can be. These irregularities create inconsistent voids in the powder packing, which leads to inhomogeneous mass distribution and inhomogeneous energy intensity. The melt pool is thus inconsistent, and voids can be created due to irregularities in the powder shape.

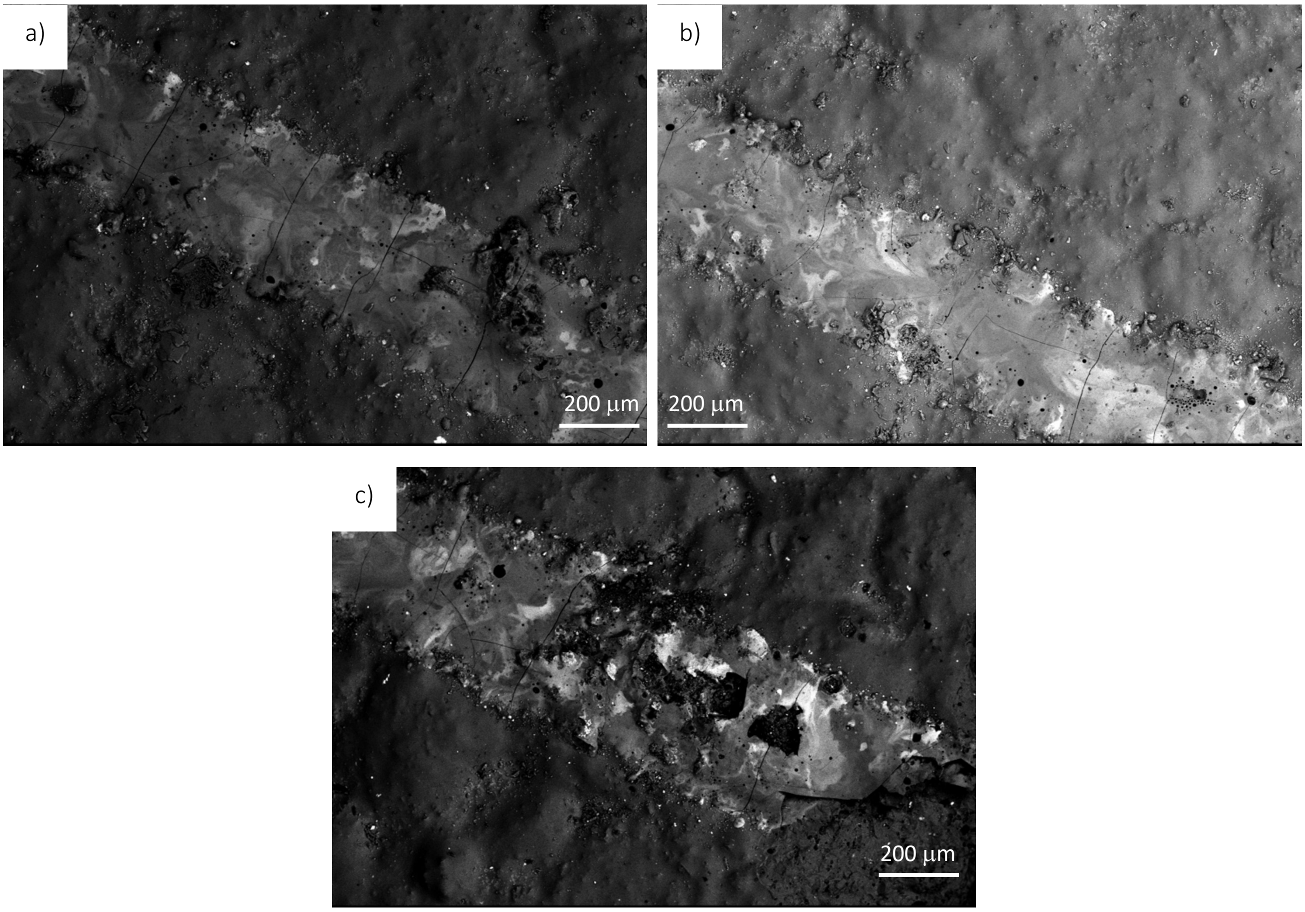

*Figure 93. SEM images of laser melted lunar regolith simulant LMS-1 with different spot size: a) 0,2 mm, b) 0,4 mm and c) 0,6 mm*

Some trials were also made on a steel substrate. The powder was successfully melted and stuck partially to the substrate. On Figure 94, some laser lines appear incomplete for 2 reasons: either because the melted powder did not stick during laser melting or because the laser-melted powder came off while removing the extra powder after the laser melting experiments. The sticking of the melted powder proved to be poor. Moreover, some lines were made with an overlap of 50 % to obtain a wider area. During the second run, the laser-melted lines came off the substrate.

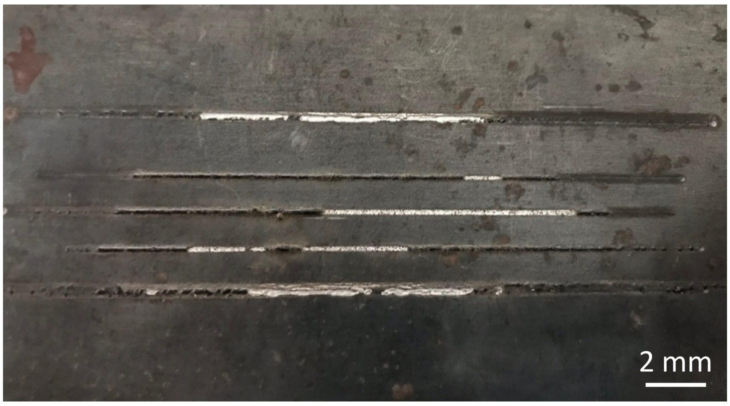

*Figure 94. Laser lines on steel plate*

The XRD analysis of the scanned lines did not show many peaks indicating crystalline phases as on the XRD pattern of the as-received powder (figure 95-b). The material turned amorphous during laser melting. The peaks seen on XRD pattern (Figure 95-a) corresponds to main phase of the powder: sodian anorthite.

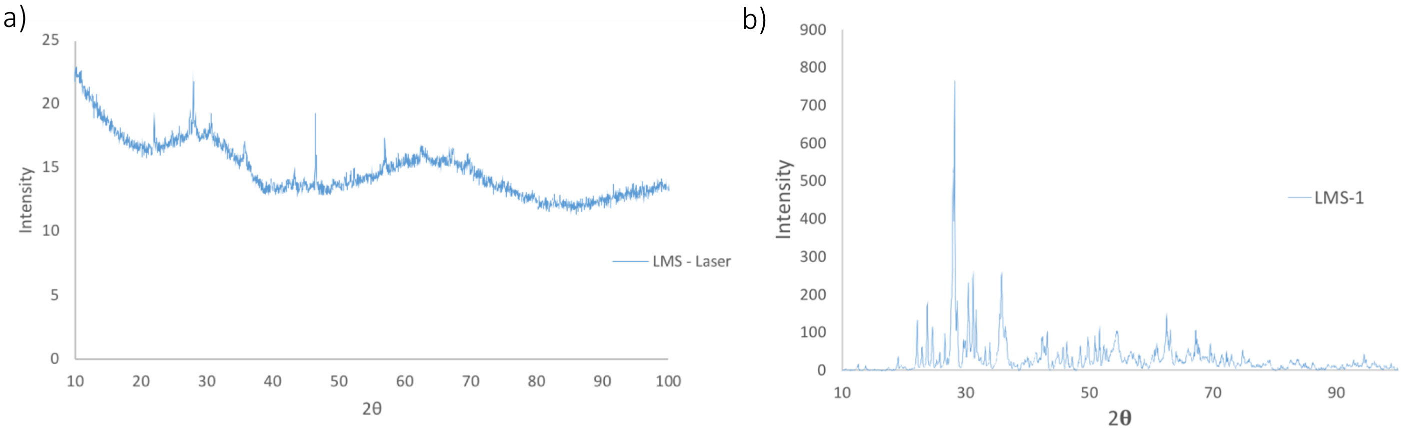

*Figure 95. XRD of a) the laser sintered lines and b) the as-received LMS-1 powder*

The laser trials can be related to the SPS experiments. Indeed, the poor sticking of the powder to the steel plate is in accordance with the trials of FGM with stainless steel and lunar regolith simulant.

## 4.4 Modelling of DLP sintering

The simulation has been developed to study the sintering of the powder when applying only temperature, as in the case of the sintering stage in Digital Light Processing process. The thermal and viscous properties of the slurry used in DLP required for the model are unknown, so properties from literature have been used. The simulation can thus be improved with proper (experimentally validated) properties. However, this simplified model could be used to evaluate the stresses within the samples and the temperature gradient during sintering.
Different tests have been performed to evaluate the effect of heating rate, temperature and average particle size. The results are summed up in the tables below. The temperature gradient corresponds to

the difference of temperature between the surface and the centre at the end of the heating. The porosity gradient is defined as the difference of porosity between the centre and the side of the samples. The samples are discs of a diameter of 20 mm and an initial height of 5 mm.

In the study of the heating rate (Table 22), an initial porosity of 47 %, an average particle size of 1 µm and a sintering temperature of 1150 °C are fixed for all the different simulations. It can be seen that using a high heating rate cause a high gradient of temperature. This high gradient of temperatures can cause stresses within the sample and inhomogeneity in the sintering process. The porosity gradient is not relevant for any heating rate even if the temperatures are not homogeneous. It could be related to the temperature of 1150 °C, which is high enough to provide good sintering.

*Table 22. Influence of the heating rate on sintering*

| Heating rate (°C/min) | Maximum stress (N/m²) | ΔT (°C) | Porosity gradient |
|---|---|---|---|
| 2 | $2,2.10^{-4}$ | 0,5 | - |
| 10 | $2,36.10^{-4}$ | 3 | - |
| 50 | $2.8.10^{-4}$ | 5 | - |
| 100 | $1.10^{-5}$ | 33 | - |

The stresses are higher on the edges and especially on the top and bottom surface (figure 96 and 97). It is related to the higher temperatures and to the gradient of temperature (figure 98). Indeed, a higher temperature enables higher consolidating of the particles and higher deformation.

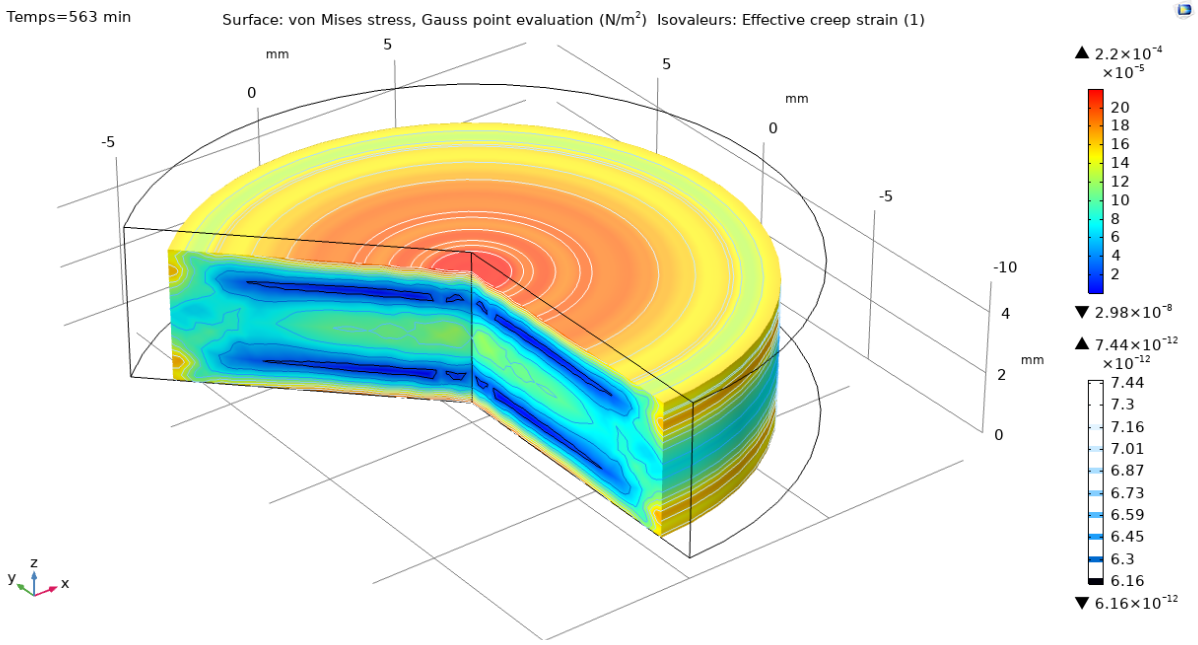

*Figure 96. 3D stresses after sintering at 1150 °C, with an average particle size of 1 µm and a heating rate of 2 °C/min*

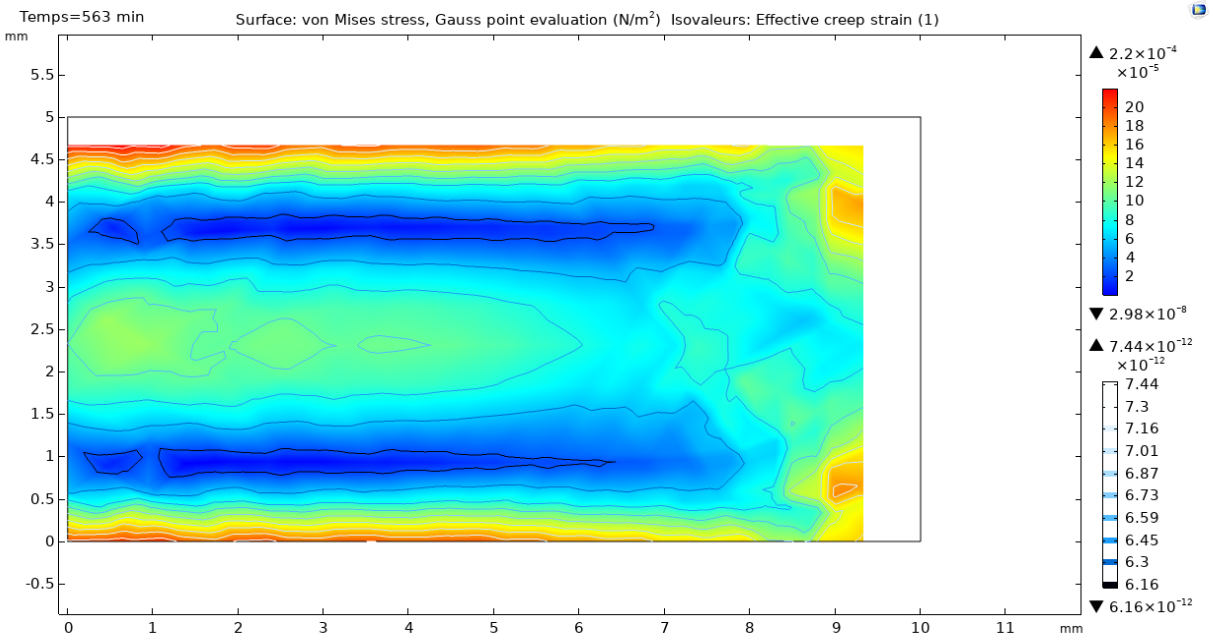

*Figure 97. 2D stresses after sintering at 1150 °C, with an average particle size of 1 μm and a heating rate of 2 °C/min*

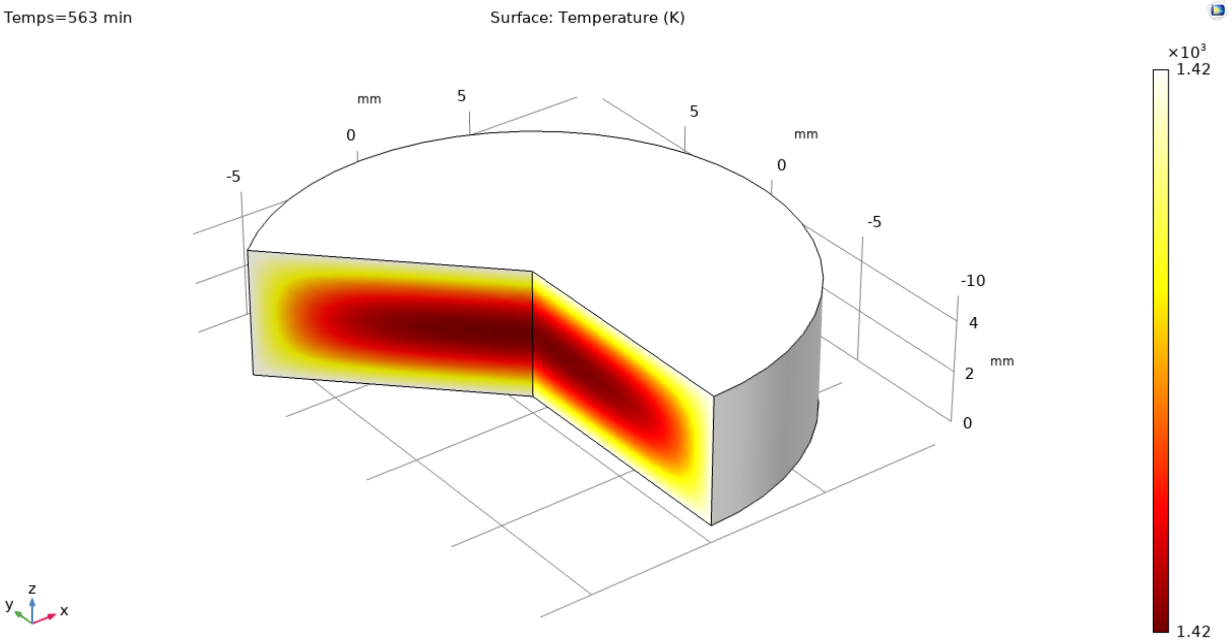

*Figure 98. Temperature profile in sintered sample*

In the table 23 below, the influence of the sintering temperature is shown. The same particle size of 1 μm and a heating of 2 °C/min were fixed. Higher sintering temperature gives higher stresses and so higher deformation. However, temperature higher than 1200 °C causes too high non-linearity of the model, which could be an evidence of potential local melting of the powder. Using a low heating rate for these simulations can explain the very low temperature gradient.

*Table 23. Influence of the sintering temperature on the sintering*

| Sintering temperature (°C) | Maximum stress (N/m²) | ΔT (°C) | Porosity gradient |
|---|---|---|---|
| 1050 | $1{,}25.10^{-4}$ | 1 | - |
| 1100 | $1{,}53.10^{-4}$ | 0,6 | - |
| 1150 | $2{,}2.10^{-4}$ | 0,5 | - |
| 1200 | $3{,}02.10^{-4}$ | 0,5 | - |

The influence of the average particle size is given in the Table 24. A sintering temperature of 1150 °C and a heating rate of 2 °C/min were fixed for these simulations. The coarser the particles, the poorest the sintering is. The stresses and strains decrease significantly when using high average particle size. It relates to the poor sintering obtained during the DLP experiments done with the lunar regolith simulant.

*Table 24. Influence of the average particle size on the sintering*

| Average particle size (μm) | Maximum stress (N/m²) | ΔT (°C) | Porosity gradient |
|---|---|---|---|
| 1 | $2{,}2.10^{-4}$ | 0,5 | - |
| 5 | $4{,}4.10^{-5}$ | 0,5 | - |
| 10 | $2{,}52.10^{-5}$ | 0,5 | - |
| 50 | $6{,}6.10^{-6}$ | 0,6 | - |

# 5 Conclusions

In situ resource utilization is crucial for future space habitation on the Moon. In this study, additive manufacturing consolidation techniques of lunar regolith simulants have been examined and optimized in order to study the functional grading feasibility with metallic substrates. For this purpose, first lunar regolith simulants were printed and debound using direct light processing and then spark plasma sintering using different conditions (temperature, particle size and composition) was applied and optimised. The similar approach was applied towards metallic powder. Finally, the best processing window for consolidation of functionally graded regolith was developed with respect to its densification, microstructural, compositional and microhardness characteristics. The following conclusions are drawn based on defined research objectives:

1. *Determine how process parameters affect the developed microstructural and densification properties.*

   The characterisation of the powder proved that all three simulants have composition and particle size distribution close to the ones of the lunar regolith. They are composed of plagioclase, pyroxene and iron titanium oxide. They proved to be suitable for studies of feasibility of consolidation of lunar regolith.

   Lunar regolith simulants can be successfully additively manufactured with direct light processing and spark plasma sintering at 1050 °C under 80 MPa. However, for the best densification it is required to sieve or mill the powders to 20 – 50 µm range. The density increased to $3.040 \pm 0.046$ g/cm$^3$ with the use of milled powder, compared to $2.831 \pm 0.077$ g/cm$^3$ with the 50 µm-sieved powder. A higher pressure could be used to avoid the milling step.

   Increasing the temperature and reducing the particle size were found to increase the densification and the Vickers micro-hardness. An optimal temperature of 1050 °C was found to avoid unstable SPS processes.

   The compositions of the sintered samples are similar to the powder composition: mainly augite, sodian anorthite and iron titanium oxide. Spark Plasma Sintering has no influence on the composition of the materials.

   Metallic powders can be fully densified with SPS at relatively low temperature and a pressure of 50 MPa. Both stainless steel and $Ti_6Al_4V$ showed homogeneous structure without precipitates or carbides. The optimal sintering parameters for stainless steel were found to be a sintering temperature of 1100 °C, a pressure of 50 MPa and a holding time of 20 min. The optimal sintering parameters for $Ti_6Al_4V$ were found to be a sintering temperature of 1050 °C, a pressure of 50 MPa and a holding time of 10 min.

   The lunar regolith simulants was found to melt at 1075 °C under 80 MPa. A proof of concept of laser melting was successfully performed and the lunar regolith simulants can be melted at low energy (less than 8 J/mm$^2$) to allow for future application in laser-based manufacturing.

2. *Investigate feasibility and type of FGM manufacturing and its properties.*

   FGM were made using the optimal SPS parameters. The combination of lunar regolith and $Ti_6Al_4V$ was the most promising. The hardness profile showed a gradual transition between the two layers and the interface was found strong enough to avoid cracking. Moreover the bonding of the lunar regolith to a steel plate is poor whereas the bonding to a ceramic substrate is very strong.

3. *Simulate selected manufacturing process to analyse the thermal properties of the materials in order to understand the relations between processing parameters and the material characteristics.*

   A model was developed to study the influence of sintering parameters on the densification of the lunar regolith simulants. It was found that the densification is higher when increasing the sintering temperature or decreasing the heating rate or decreasing the particle size. These results are in accordance to the experimental results. However further studies on the thermal properties of the lunar regolith simulants would be required to increase the accuracy of the model.

4. *Provide a link to actual lunar applications based on material constraints.*

   This study showed the feasibility of producing dense specimens via Spark Plasma Sintering. The specimens showed high hardness useful to protect space habitats against impacts. Moreover FGM were successfully sintered and the combination of mechanical properties of both materials would be useful to mitigate the different constraints of the lunar environment.

   Laser melting proved to be feasible with lunar regolith simulants. Using a low energy density, the lunar regolith simulant can be melted and used as a coating on metallic surfaces to protect them against potential hazards.

The main objective of “Investigate what is the most suitable consolidation techniques for both lunar dust and functionally graded materials (FGMs)” can then be concluded as follows:

- Digital Light Processing is a promising consolidation technique even though the sintering stage must be optimized or coupled with a hot isostatic pressing step.

- Spark Plasma Sintering can be used to sinter both lunar regolith simulants and metals. Moreover it was found to be a promising technique to sinter Functionally Graded Materials. This technique offers high densification with a fast process.

## Recommendations for future work

This master thesis presents a research about the feasibility of consolidating techniques of in-space resources. It presents the preliminary results and offers good opportunities for further research. The following recommendations and follow-ups for this study are proposed:

- SPS results gave good results with high densified samples of lunar regolith samples. The process parameters were studied but optimization would be required to obtain higher densification and complete densification of the samples. Higher pressure of 100 MPa could be a good option to decrease the porosity and to get more homogeneous structure. Moreover, the use of higher pressure could suppress the milling stage required when using lower pressure.
- This study focuses on small samples manufactured via SPS. The sintering of bigger samples should be carried out because inhomogeneous distribution of pores was noticed in the samples and it may cause problems for sintering of thicker samples.
- DLP would need optimization of the sintering process. The use of milled powder (powder size of less than 5 $\mu$m) could help and should be investigated to determine the optimal conditions.
- The laser lines scans proved to be promising. The powder can be easily melted with a laser and Selective Laser Melting is a technique that should be studied further. This technique is indeed interesting because it allows to make complex shape. Furthermore, this technique could be investigated as a potential coating technique. The lunar regolith could be used as a coating on top of metallic component to increase the resistance to meteoroids impacts or the resistance to radiation. However, optimization would be required to allow the lunar regolith powder to stick on the metallic substrate.
- FGM have been manufactured during this thesis and titanium alloy proved to be a promising metal whereas the stainless steel showed poor sintering properties. Many opportunities and follow-ups for FGM can be envisioned:
  - the sintering process should be optimized with potential studies implementing gradients of materials to avoid high thermal stresses.
  - aluminium could be considered as a potential metal for FGM according to its availability on the Moon. However, its sintering temperature would be lower than 500 °C and a multistep sintering process would be required. Moreover, thermal stresses should be well considered due to mismatch in thermal coefficients.
  - the use of buffer layers between the metal layer and the lunar regolith layer should be studied: the composition and the thickness of these buffer layers need to be determined.
- This study focuses on the optimization of the process parameters based on the microstructural results. Further studies on the mechanical properties of the sintered samples are required. Mechanical properties such as strength, fracture toughness would be interesting to determine the ability of these specimens to withstand the lunar conditions.
- The model should be improved with adequate properties of the sintered specimens. A study on the thermal properties of the sintered specimens should be carried out and the properties found could then be implemented to the model. The model could then be used to determine the properties of the FGM.

# 6 Bibliography

[1] M. Fateri and A. Gebhardt, "Process Parameters Development of Selective Laser Melting of Lunar Regolith for On-Site Manufacturing Applications," *International Journal of Applied Ceramic Technology,* vol. 12, no. 1, 2015.

[2] E. Robens, A. Dąbrowski, E. Mendyk, J. Goworek, K. Skrzypiec, M. Drewniak, M. Dumańska-Słowik, W. Gac, R. Dobrowolski, S. Pasieczna-Patkowska, M. Huber, M. Iwan, K. J. Kurzydłowski, T. Płociński, J. Ryczkowski, Z. Rzączyńska and J. W. Sobczak, "Investigation of surface properties of lunar regolith – Part IV," *Annales Universitatis Mariae Curie-Skłodowska, sectio AA – Chemia,* vol. 63, pp. 144-168, 2008.

[3] Y. Liu and L. A. Taylor, "Characterization of lunar dust and a synopsis of available lunar simulants Yang Liu n, Lawrence A. Taylor," *Planetary and Space Science,* no. 59, pp. 1769-1783, 2011.

[4] A. Bhattacharya, A. Porwal, S. Dhingra, S. De and G. Venkataraman, "Remote estimation of dielectric permittivity of lunar surface regolith using compact polarimetric synthetic aperture radar data," *Advanced in Space Research,* no. 56, pp. 2439-2448, 2015.

[5] D. S. McKay, G. Heiken, A. Basu, G. Blanford, S. Simon, R. Reedy, B. M. French and J. Papike, "The Lunar Regolith," in *Lunar Sourcebook*, Cambridge University Press, 1991, pp. 285-356.

[6] V. S. Engelschiøn, S. R. Eriksson, A. Cowley, M. Fateri, A. Meurisse, U. Kueppers and M. Sperl, "EAC-1A: A novel large-volume lunar regolith simulant".

[7] G. Cesaretti, E. Dini, X. De Kestelier, V. Colla and L. Pambaguian, "Building components for an outpost on the Lunar soil by means of a novel 3D printing technology," *Acta Astronautica,* no. 93, pp. 430-450, 2014.

[8] D. S. McKay, J. L. Carter, W. W. Boles, C. C. Allen and J. H. Allton, "JSC-1: A new lunar soil simulant," *Engineering, Construction, and Operations in Space IV,* pp. 857-866, 1994.

[9] A. Meurisse, A. Makaya, C. Willsch and S. Sperl, "Solar 3D printing of lunar regolith," *Acta Astronautica,* vol. 152, pp. 800-810, 2018.

[10] V. Marzulli and F. Cafaro, "Geotechnical Properties of Uncompacted DNA-1A Lunar Simulant," *Journal of Aerospace Engineering,* vol. 32, 2019.

[11] M. Liu, W. Tang, W. Duan, S. Li, R. Dou, G. Wang, B. Liu and L. Wang, "Digital light processing of lunar regolith structures with high mechanical properties," *Ceramics International,* vol. 45, pp. 5829-5836, 2019.

[12] Z. Yongchun, S. Shijie, O. ZIyuan, Z. Yongliao, L. Jianzhong, L. Chunlai, L. Xiongyao and F. Junming, "CAS-1 lunar soil simulant," *Advances in Space Research,* vol. 43, pp. 448-454, 2009.

[13] X. Zhang, M. Khedmati, Y. Kim, H. Shin, J. Lee, Y. Kim and B. Cui, "Microstructure evolution during spark plasma sintering of FJS-1 lunar soil simulant," *Journal of the American Ceramic Society,* pp. 1-13, 2019.

[14] A. M. Jablonski and K. A. Ogden, "Technical Requirements for Lunar Structures," *Journal of Aerospace Engineering,* vol. 21, no. 2, pp. 72-90, 2008.

[15] H. Benaroya, Building Habitats on the Moon Engineering - Approaches to Lunar Settlements, Springer, 2018.

[16] M. P. Sansoucie, P. V. Hull and M. L. Tinker, "HABITAT DESIGN OPTIMIZATIONAND ANALYSIS," NASA Marshall Space Flight Center.

[17] P. Cavaliere, Spark Plasma Sintering of Materials - Advances in Processing and Applications, Springer, 2019.

[18] X. L. Phuah, H. Wang, B. Zhang, J. Cho, X. Zhang and H. Wang, "Ceramic Material Processing Towards Future Space Habitat: Electric Current-Assisted Sintering of Lunar Regolith Simulant," *Materials,* vol. 4128, no. 13, 2020.

[19] L. Song, J. Xu, S. Fan, H. Tang, X. Li, J. Liu and X. Duan, "Vacuum sintered lunar regolith simulant: Pore-forming and thermal conductivity," *Ceramics International,* vol. 45, pp. 3627-3633, 2019.

[20] M. A. Hobosyan and K. S. Martirosyan, "SINTERING OF REGOLITH BY ACTIVATED THERMITES: A NOVEL APPROACH FOR LUNAR IN SITU RESOURCE UTILIZATION," in *43rd Lunar and Planetary Science Conference*, Texas, 2012.

[21] E. J. Faierson, K. V. Logan, B. K. Stewart and M. P. Hunt, "Demonstration of concept for fabrication of lunar physical assets utilizing lunar regolith simulant and a geothermite reaction," *Acta Astronautica,* vol. 67, pp. 38-45, 2010.

[22] ISO/ASTM59200, "Standard Terminology for Additive Manufacturing – General Principles – Terminology," West Conshohocken, ASTM International, 2015.

[23] M. Molitch-Hou, "Overview of additive manufacturing process," in *Additive Manufacturing - Materials, Processes, Quantifications and Applications*, Elsevier, 2018, pp. 1-38.

[24] Omnexus, "What is additive manufacturing?," [Online]. Available: https://omnexus.specialchem.com/selection-guide/3d-printing-and-additive-manufacturing-polymers-and-processes. [Accessed 21 November 2019].

[25] R. M. Mahamood and E. T. Akinlabi, "Additive Manufacturing of Funtionally Graded Materials," in *Functionally Graded Materials*, Springer, 2017, pp. 47-68.

[26] ASTMF2792-12a, "Standard Terminology for Additive Manufacturing Technologies," ASTM International, West Conshohocken, 2015.

[27] P. J. Bartolo, Stereolithography - Materials, Processes and Applications, Springer, 2011.

[28] C.-J. Bae, A. Ramachandran, K. Chung and S. Park, "Ceramic Stereolithography: Additive Manufacturing for 3D Complex Ceramic Structures," *Journal of the Korean Ceramic Society,* vol. 54, no. 6, pp. 470-477, 2017.

[29] T. Moritz and S. Maleksaeedi, "Additive manufacturing of ceramic component," in *Additive Manufacturing - Materials, Processes, Quantifications and Applications*, Elsevier, 2018, pp. 105-161.

[30] R. He, G. Ding, K. Zhang, Y. Li and D. Fang, "Fabrication of SiC ceramic architectures using stereolithography combinedwith precursor infiltration and pyrolysis," *Ceramics International,* vol. 45, pp. 14006-14014, 2019.

[31] Formlabs, "SLA vs. DLP: Compare Resin 3D Printing Technologies (2020 Guide)," [Online]. Available: https://formlabs.com/blog/3d-printing-technology-comparison-sla-dlp/. [Accessed December 2019].

[32] R. Dou, W. Z. Tang, L. Wang, S. Li, W. Y. Duan, M. Liu, Y. B. Zhang and G. Wang, "Sintering of lunar regolith structures fabricated via digital light processing," *Ceramics International,* 2019.

[33] Q. Chen, G. Guillemot, C.-A. Gandin and M. Bellet, "Three-dimensional finite element thermomechanical modeling of additive manufacturing by selective laser melting for ceramic materials," *Additive Manufacturing,* vol. 16, pp. 124-137, 2017.

[34] A. Goulas, R. A. Harris and R. J. Friel, "Additive manufacturing of physical assets by using ceramic multicomponent extra-terrestrial materials," *Additive Manufacturing,* vol. 10, pp. 36-42, 2016.

[35] R. N. Grugel and H. Toutanji, "Sulfur ‘‘concrete’’ for lunar applications – Sublimation concerns," *Advance in SPace Research,* vol. 41, pp. 103-112, 2008.

[36] H. A. Toutanji, S. Evans and R. N. Grugel, "Performance of lunar sulfur concrete in lunar environments," *Construction and Building Materials,* vol. 29, pp. 444-448, 2012.

[37] M. Fateri, A. Meurisse, M. Sperl, D. Urbina and and al., "Solar Sintering for Lunar Additive Manufacturing," *Journal of Aerospace Engineering,* vol. 32, 2019.

[38] G. Hsiang Loh, E. Pei, D. Harrison and M. D. Monzón, "An Overview of Functionally Graded Additive Manufacturing," *Additive Manufacturing,* vol. 23, pp. 34-44, 2018.

[39] R. Modupe Mahamood and E. Titilayo Akinlabi, Functionally Graded Materials, Cham: Springer Nature, 2017.

[40] I. M. El-Galy, B. I. Saleh and M. H. Ahmed, "Functionally graded materials classi cations and development trends from industrial point of view," Springer Nature, Switzerland, 2019.

[41] V. A. Popovich, E. V. Borisov, A. A. Popovich, V. S. Sufiiarov, D. V. Masaylo and L. Alzina, "Functionally graded Inconel 718 processed by additive manufacturing:Crystallographic texture, anisotropy of microstructure andmechanical properties," *Materials and Design,* vol. 114, pp. 441-449, 2017.

[42] R. M. Mahamood and E. T. Akinlabi, "Types of Functionally Graded Materials and Their Areas ofApplication," in *Functionally Graded Materials*, Switzerland, Springer, 2017, pp. 9-21.

[43] A. Gupta and M. Talha, "Recent development in modeling and analysis of functionally graded materials and structures," *Progress in Aerospace Sciences,* vol. 79, pp. 1-14, 2015.

[44] Y. Hu and W. Cong, "A review on laser deposition-additive manufacturing of ceramics and ceramic reinforced metal matrix composites," *Ceramics International,* vol. 44, pp. 20599-20612, 2018.

[45] I. Cheibas, M. Laot, V. A. Popovich, B. Rich and S. Rodriguez Castillo, "Additive Manufacturing of Functionally Graded Materials with In-Situ Resources," 2020.

[46] L. Sibille, P. Carpenter, R. Schlagheck and R. A. French, "Lunar regolith simulant materials: recommendations for standardization, production, and usage," 2006.

[47] J. Schleppi, J. Gibbons, A. Groetsch, J. Buckman, A. Cowley and N. Bennett, "Manufacture of glass and mirrors from lunar regolith simulant," *Journal of Materials Science,* vol. 54, no. 5, pp. 3726-3747, 2019.

[48] P. S. Greenberg, D. Chen and S. A. Smith, "Aerosol measurements of the fine and ultrafine particle content of lunar regolith," 2007.

[49] L. A. Taylor and Y. Liu, "Important considerations for Lunar Soil Simulants," *Earth and Space 2010.*

[50] X. Chen, Y. Zhang, D. Hui, M. Chen and Z. Wu, "Study of melting properties of basalt based on their mineral components," *Composites Part B: Engineering,* vol. 116, pp. 53-60, 2017.

[51] A. Meurisse, J. C. Beltzung, M. Kolbe and A. Cowley, "Influence of Mineral Composition on Sintering Lunar Regolith," *Journal of Aerospace Engineering,* vol. 30, 2017.

[52] A. Tsuchiyama and E. Takahashi, "Melting kinetics of a plagioclase feldspar," *Contributions to mineralogy and petrology,* vol. 84, pp. 345-354, 1983.

[53] V. Badescu, Moon, Badescu, 2012.

[54] A. B. Kale, A. Bag, J.-H. Hwang, E. G. Castle, M. J. Reece and S.-H. Choi, "The deformation and fracture behaviors of 316L stainless steels fabricatedby spark plasma sintering technique under uniaxial tension," *Materials Science & Engineering A,* vol. 707, pp. 362-372, 2017.

[55] G. Marnier, C. Keller, J. Noudem and E. Hug, "Functional properties of a spark plasma sintered ultrafine-grained 316L steel," *Materials and Design,* vol. 63, pp. 633-640, 2014.

[56] F. M. Kgoete, A. Popoola and O. Fayomi, "Influence of spark plasma sintering on microstructure and corrosion behaviour of Ti-6Al-4V alloy reinforced with micron-sized Si3N4 powder," *Defence Technology,* vol. 14, pp. 403-407, 2018.

[57] O. E. Falodun, B. A. Obadele, S. R. Oke, O. O. Ige, P. A. Olubambi, M. L. Lethabane and S. W. Bhero, "Influence of spark plasma sintering on microstructure and wear behaviour of Ti−6Al−4V reinforced with nanosized TiN," *Transactions of Nonferrous Metals Society of China,* vol. 28, pp. 47-54, 2018.

[58] M. Fateri, R. Sottong, M. Kolbe, J. Gamer, M. Sperl and A. Cowley, "Thermal properties of processed lunar regolith simulant," *Applied Ceramic Technology,* pp. 1-10, 2019.

[59] L. Abbondanti Sitta and M. Lavagna, "3D printing of moon highlands regolith simulant," in *69th INternational Astronautical Congress*, Bremen, 2018.

[60] V. Krishna Balla, L. B. Roberson, G. W. O'Connor, S. Trigwell, S. Bose and A. Bandyopadhyay, "First demonstration on Direct Laser Fabrication of lunar regolith parts," *Rapid Prototyping Journal,* pp. 451-457, 2012.

[61] A. Goulas and R. J. Friel, "3D printing with moondust," *Rapid Prototyping Journal,* pp. 864-870, 2016.

[62] D. Ćorić, M. . M. Renjo and L. Ćurković, "Vickers indentation fracture toughness of Y-TZP dental ceramics," *International Journal of Refractory Metals and Hard Materials,* vol. 64, pp. 14-19, 2017.

[63] B. Sarbandi, "Finite Element Simulation of Ceramic Deformation During Sintering," 2011.

[64] Z. Chen, Z. Li, J. Li, C. Liu, C. Lao, Y. Fu, C. Liu, Y. Li, P. Wang and Y. He, "3D printing of ceramics: A review," *Journal of the European Ceramic Society,* vol. 39, pp. 661-687, 2019.

[65] M. A. Roach, D. Keicher, E. Maines, B. Wall, C. Wall, J. Lavin, S. Whetten and L. Evans, "Mechanical challenges of 3D printing ceramics using digital light processing," Albuquerque.

[66] Y. Cheng, Z. Cui, L. Cheng, D. Gong and W. Wang, "Effect of particle size on densification of pure magnesium during spark plasma sintering," *Advanced Powder Technology,* vol. 28, pp. 1129-1135, 2017.

[67] A. Materials, "Silica - Silicon Dioxide (SiO2)," 13 December 2001. [Online]. Available: https://www.azom.com/properties.aspx?ArticleID=1114. [Accessed 2020].

[68] A. Materials, "Alumina - Aluminium Oxide - Al2O3 - A Refractory Ceramic Oxide," February 2001. [Online]. Available: https://www.azom.com/properties.aspx?ArticleID=52. [Accessed 2020].

[69] C. Keller, K. Tabalaiev, G. Marnier, J. Noudem, X. Sauvage and E. Hug, "Influence of spark plasma sintering conditions on the sintering and functional properties of an ultra-fine grained 316L stainless steel obtained from ball-milled powder," *Materials Science and Engineering A,* vol. 665, pp. 125-134, 2016.

[70] K. Crosby, L. L. Shaw, L. L. Estournes, G. Chevallier, A. W. Fliflet and M. A. Imam, "Enhancement in Ti–6Al–4V sintering via nanostructured powder and spark plasma sintering," *Powder Metallurgy,* vol. 57, no. 2, pp. 147-154, 2014.

[71] Y. Long, H. Zhang, T. Wang, X. Huang, Y. Li, J. Wu and H. Chen, "High-strength Ti–6Al–4V with ultrafine-grained structure fabricated by high energy ball milling and spark plasma sintering," *Materials Science and Engineering,* vol. 585, pp. 408-414, 2013.

[72] N. Poondla, T. S. Srivatsan, A. Patnaik and M. Petraroli, "A study of the microstructure and hardness of two titanium alloys: Commercially pure and Ti–6Al–4V," *Journal of Alloys and Compounds,* vol. 486, pp. 162-167, 2009.

[73] C. S. Ray, S. T. Reis, S. Sen and J. S. O'Dell, "JSC-1A lunar soil simulant: Characterization, glass formation, and selected glass properties," *Journal of Non-Crystalline Solids,* vol. 356, pp. 2369-2374, 2010.

# 7 Appendix 1 – Theoretical density with XRD

The theoretical density could be calculated with XRD analysis. XRD is used to determine the composition of the lunar regolith simulant samples. When the phases are known, the lattice parameters of each phase can be used to determine the theoretical density of the material as follows:

$$d = \sum_{i=0}^{n} \frac{n_i M_i}{N_A {V_i}^3} \tag{22}$$

with $n_i$ the number of atoms per unit cell of the phase i, $M_i$ the molar weight of the phase i, $N_A$ the Avogadro number and $V_i$ the volume of the phase i.

# 8 Appendix 2 – Paper for First Aerospace Europe Conference, Bordeaux, 2020

Available on http://www.esa.int/gsp/ACT/doc/HAB/ACT-RPR-HAB-2020-AEC-Functionally_Graded_Materials.pdf
Attached to this master thesis.

# 9 Appendix 3 – Paper for SPOOL (under review)

Attached to this master thesis.